UC Berkeley
UC Berkeley Electronic Theses and Dissertations

Title
Investigations of Iron Chalcogenides and Pnictides

Permalink
https://escholarship.org/uc/item/09n5q9md

Author
Valdivia, Patrick

Publication Date
2015

Peer reviewed|Thesis/dissertation

Investigations of Iron Chalcogenides and Pnictides

by

Patrick Neil Valdivia

A dissertation submitted in partial satisfaction of the

requirements for the degree of

Doctor of Philosophy

in

Engineering: Materials Science and Engineering

in the

Graduate Division

of the

University of California, Berkeley

Committee in charge:

Professor Robert Birgeneau, Chair
Professor Frances Hellman
Professor Joseph Orenstein
Professor Dunghai Lee

Summer 2015

Investigations of Iron Chalcogenides and Pnictides

Abstract

Investigations of Iron Chalcogenides and Pnictides

by

Patrick Valdivia

Dr. of Philosophy in Materials Science and Engineering

University of California, Berkeley

Professor Robert Birgeneau, Chair

Herein is described several experiments investigating the basic properties of iron pnictide and chalcogenide compounds which are all closely related to superconducting compounds. A brief overview of the field is provided, and experimental techniques are described. Four studies are then listed in full, along with explanations of their relevance to the field.

Contents

Acknowledgments

During my Ph.D. I have been fortunate to have had the opportunity to interact with a lot of talented people. First and foremost, I would like to thank our lab members: Byron Freelon, Stephen Wilson, Costel Rotundu, Tom Forrest, Jun Zhao, Jinsheng Wen, Min Gyu Kim, Zhijun Xu, Meng Wang, Alex Frano, and Ming Yi. I have benefited greatly from the time spent with each of them. I would like to further thank Byron, Tom, and Min Gyu whom acted successively as my postdoctoral advisors during different stages of my thesis. Difficult as it is at Berkeley, they each made a lot of time for me. Byron helped me to get started in our non-intuitive field of studying superconductivity with x-ray and neutron beams. Tom and I worked closely discussing growth, transport measurements, as well as synchrotron experiments. Tom's experimental style is patient and sound, and he remains very collected during synchrotron experiments. In the last few years, Min Gyu has been especially helpful to me in the process of publishing and concluding my work. He brings rigor to every process of his work. I've also been fortunate to be able to collaborate with Zhijun and Meng both in our home laboratories and performing neutron experiments and analysis thereof over the past couple years; and I have learned a lot from working with them.

Among the engineers and scientists in Edith's lab there are many whom have consistently supported for our efforts including especially Gautam Gundiah, Zewu Yan, Chris Ramsey, Stephen Hanrahan, Katie Brennan, Yetta Porter, and Najeb Abdul Jabbar.

I thank the Ramesh and Hellman labs for providing much support with x-ray and SQUID measurements, especially Claudy Serrao, Jiun-Haw Chu, Jian Liu, Di Yi, Julie Karel, and Catherine Bordel. I also thank the James Analytis and Toni Helm for work we've done together on a recent project which we plan to publish soon after this thesis is complete.

Additionally, I thank the members of my qualifying and/or thesis committee: Frances Hellman, Joe Orenstein, Dung Hai Lee, and Yuri Suzuki for helping me to prepare for and participating in my qualifying exam, and for their continued support following the exam. The exam process offered me a more complete perspective of my work, and allowed me to re-evaluate my projects more carefully.

I also thank my home department of Materials Science for providing a positive environment and interesting coursework; in particular I would like to thank Oscar Dubon for offering regular encouragement and interest in my progress. I thank those in the physics department who supported our lab including especially Eleanor Crump and Anthony Vitan. There are many others around campus and LBL whom have been great help. A few whom come to mind are James Wu, Daniel Lee, and Tim Teague.

Outside of UC Berkeley and LBL, Dennis Keane and Qing Ma at DND-CAT Argonne, and Mike Toney, Yezhou Shi, Badri Shyam, Valery Borzenets, Apurva Mehta, Bart Johnson, and J. R. Troxel at SLAC helped me to plan for and carry out many x-ray experiments. Brian Toby at Argonne and Hui Wu at NIST offered help with powder diffraction and refinement.

Finally, I thank Bob and Edith for providing me the opportunity to participate in this research; it has been fascinating to be part of a field which for which our understanding

is developing month to month, and having a research group with as much freedom and aspiration as ours has.

Chapter 1

Introduction

1.1 Iron based superconductors: discovery

Unlike the cuprates in which Bednorz and Muller set out to discover high-T_c superconductivity, the discovery of iron-based superconductors was a product of investigations into the role of two dimensional electronic and optical properties of materials [1, 2]. P-type conduction in transparent oxide semiconductors is difficult to realize, as holes tend to be localized on oxygen sites. However, if a cation in the compound has electronic energy levels which overlap with the 2p oxygen orbitals, the holes may delocalize. Alternatively, if both electron and hole charge carriers can be localized in a metallic plane which is separated from the plane of oxygen sites, light emission might also be enhanced. Hosono's group was interested in investigating a number of layered materials because layers allow modularity in design of the electrical properties. Their group therefore investigated not only optically active materials, but related materials with metallic planes [2]. For both the cuprates and the iron pnictides, the superconductivity occurs close to an antiferromagnetically ordered phase. One of the most stark contrasts to the cuprates is that the parent compounds of the iron pnictide superconductors are metallic, having electron and hole Fermi surfaces deriving from multiple d-orbitals of iron, but primarily of d_{xz} and d_{yz} character [3, 4]. For the cuprates, the parent compounds are Mott insulators whose properties can be described by single hole band [5].

1.2 Motivation

The general motivation for my thesis was to figure out design rules when the rules are founded on principles, or empirical 'control rules' otherwise, to tailor the electronic or magnetic properties in strongly correlated systems. As a materials scientist my primary variables would be chemical composition and processing conditions. As the higher T_c iron-based superconductors were discovered just months before I started graduate school in 2008, it seemed like a good entry point for such topics.

1.3 Are iron-based superconductors unconventional?

Next to the cuprates, iron based superconductors have the second highest T_c among known superconductors, excluding a recent claim of superconductivity in hydride phases at very high pressure [6]. An important question which then arises is: are the iron-based superconductors unconventional, i.e., could they be understood within the context of existing theory? If the superconductors are conventional BCS superconductors, then the properties of these materials should correspond to the predictions of the BCS theory of superconductivity, which we discuss next.

1.4 Isotope effects, superconducting gap size, and gap symmetry: comparisons with BCS theory

Isotope effects: overview

Bardeen Cooper and Schrieffer's theory of superconductivity accounted for the experiments showing that increasing the mass of isotopes in a superconductor will cause the critical temperature to decrease; in particular BCS showed that the critical temperature goes as $M^{-\alpha}$ with $\alpha = 0.5$. Isotope effects are usually taken as a hallmark of phonon-mediated superconductivity. Two recent examples of successful isotope effect studies were done for the superconductivity in MgB_2 [7] and Rb_3C_60 [8]. In MgB_2, isotopes of Mg and B can be shown to produce different superconducting critical temperatures, and the Boron isotope effect is substantial at $\alpha_B = 0.26$ [7]; In Rb_3C_60, substituting carbon isotopes gives $\alpha_C = 0.37$ [8]. Deviation from the BCS value in these cases is suggested to be due to Coulomb interactions.

Isotope effects: cuprates and pnictides

In the case of the cuprates, and the iron based superconductors, studying the isotope effect is more difficult due to the correlation of oxygen vacancies with T_c in the cuprates [9, 10, 11], and presumably, due to the question of substitutional disorder and/or other defects/impurity phases for studies which have been done thus far on the pnictides. There are contradictory reports for the existence or the lack of isotope effects in $YBCO$ [9, 10, 11], which was studied because it has been claimed to have less disorder than the LBCO system due to the absence of random site alloying disorder; however, this point is disputed as the YBCO system exhibits defects which are not present in LBCO. In the iron pnictides, two different groups studied the iron isotope effect in $Ba_{0.6}K_{0.4}Fe_2As_2$ and obtained much different results: one group found a large iron isotope effect with $\alpha = 0.35$ [12], while another group found $\alpha = -0.18$, an inverse isotope effect [13]. In iron selenide, one group found a very large iron isotope effect when taking the average of a number of samples [14], yet still noted a single sample out of fourteen measured samples which deviated from the trends;

furthermore, an inverse isotope effect was observed for the telluride substituted compound [15]. In my opinion the difficulties observed in the chalcogenides may be due to the random occupation of the interstitial iron site [16], and also the magnetic impurity phases [17] which accompanied the main phase in the first study [14] and also possible chalcogen vacancies which may exist in FeSe [18].

Limitations of isotope effect studies and other methods to address the validity of BCS theory

Successful isotope effect experiments are difficult, requiring precise control of the measurement environment and the sample quality, see this reference [19]. In addition, isotope effects can be reduced by the existence of a retarded electron-phonon interaction – some transition metals such as ruthenium and osmium [19] do not exhibit isotope effects [20, 21].

The isotope effect can be considered within the BCS formula for the critical temperature $T_c = (1.13/k)\,\hbar w_D \exp{-1/N_0 V}$ as the Debye frequency w_D is lowered by substituting heavier elements. However, the full equation tells us that there are other ways to check the validity of the theory: experimental measurements of the density of states N_0, Debye Frequency, and experimental estimates of the electron-phonon interaction energy V can be combined to create a strong argument against the BCS coupling mechanism. One application of such studies was in $BaPb_{0.75}Bi_{0.25}O_3$. Band structure calculations of the 'bare' density of states for this material can be compared with the experimentally determined density of states extracted from heat capacity measurements across T_c and susceptibility estimates of the upper critical field to suggest that the electron-phonon coupling is weak. Knowledge of the Debye frequency then shows that the critical temperatures for the bismuth oxides cannot be obtained with the BCS formula. Then, the authors argue that the fact that moderate isotope effects are observed nonetheless, with $\alpha = 0.2$ to 0.25 must be due to coupling of the phonons to charge fluctuations, which drive the superconductivity [22]. Therefore, isotope effects should only be considered in conjunction with other data if their purpose is to support a BCS mechanism.

Another separate claim of BCS theory is that the saturated, low-temperature gap size is proportional to the critical temperature. Therefore, BCS theory does not suffice to explain why T_c changes drastically with only modest changes in the saturated, low-temperature gap size in, $Bi_2Sr_2Ca_{1-x}Dy_xCu_2O_{8+\delta}$ [23]. We are not aware of a similar study in the iron based superconductors; hence we have only mentioned the isotope studies above. However, it was noted by Singh that one does not need to calculate the electron-phonon interaction strength: knowledge of the Debye frequency alone is enough to suggest that BCS theory is not applicable to the iron based superconductors [3].

However, this leaves open the question: if BCS theory doesn't apply to the iron based superconductors, then what should take its place? Similar to the case of explaining conventional superconductors, the explanation of novel superconductivity should rest on successfully explaining experimental data; and a good theory should also give testable predictions, or

at the least be falsifiable/distinguishable from other theories. At present, there is not yet a consensus on the mechanism of superconductivity for the iron-based superconductors.

1.5 Phase diagrams

With regards to the goal of characterizing these systems to understand in detail the superconducting mechanisms, there has been rapid progress since the T_c jump in 2008 [1] which followed their previous discovery of superconductivity at 4K in LaFePO [24]. $BaFe_2As_2$, one of the parent systems of superconductivity, permits substitution by a variety of elements on its crystal sites [25]. In addition, there are a now a large number of structural families of iron-based superconductors.

The disadvantage to there being so many structural and chemical degrees of freedom which can be used to study these superconductors is that there are a large number of experiments which claim many different phases and parameters that may be relevant to the superconductivity. On the other hand, this offers many opportunities for unambiguous testing of theories against simple experiments. We hope that with time, and clever experimentation, a convergence will be achieved on which parameters are essential to stabilizing or destabilizing superconductivity with respect to its neighboring phases. We will now discuss some features of the phase diagrams which are actively studied including the antiferromagnetism, the superconducting dome, and pressure/structural effects and then conclude with a note on the limitations of phase diagrams.

Antiferromagnetism

Considering substitutional phase diagrams of superconductivity, one of the first features one notices is that both the cuprate [26] and the iron pnictide superconductors [27] arise in proximity to an antiferromagnetically ordered state. Detailed neutron scattering studies show that the spin fluctuations associated with the antiferromagnetic order in these materials are gapped when superconductivity develops, and that the susceptibility in the superconducting state exhibits a broad maximum at energies just above the gap energy. A redistribution of magnetic spectral weight occurs which seems to correlate with the onset of superconductivity - the integrated intensity of the spin fluctuations up to some cutoff energy typically increases like an order parameter below T_c; see e.g. [28, 29] and works which cite them. There are several theoretical models which suggest the spin fluctuations play a role in the superconductivity; indeed, one of the first theories of superconductivity in the pnictides is of this type [30].

Superconducting dome

Furthermore, superconductivity appears to have a dome-like feature as a function of substitution in the iron pnictides, which is reminiscent of several phase diagrams in the cuprates

[26, 31, 32]. What determines the shape of the superconducting dome in each of these systems? One persistent idea is that a quantum critical point, occurring at zero temperature, may lie beneath the dome producing fluctuations which give rise to the superconductivity. As a critical point should show divergence in some derivative of the free energy - the parameter which diverges may give insight into the type of fluctuations giving rise to superconductivity, if one exists at all. In the cuprate system YBCO, an increase in the effective mass by a factor of three occurs within a small region of oxygen substitution when superconductivity is suppressed by field; this is claimed to arise from the quantum critical point beneath the dome [32]. A similar 'divergence' of effective mass, or at least an increase by 2 to 3 times, has been observed in the phosphorous substituted barium-iron-arsenide compound [33]. However, recent work on the same phase diagram with a dense set of sample compositions suggests a first-order transition at the onset of superconductivity rather than a quantum critical point [34]. Another claim in the cuprates is that there may be a quantum critical point beneath the superconducting dome which is related to the suppression of the pseudogap phase. This critical point is proposed to occur in the slightly overdoped region, where the critical current density is the highest, even though T_c is not optimal at this concentration [35]; this was confirmed by an NMR study whom claim the pseudogap phase coexists with superconductivity and competes for electrons at the Fermi surface [36]. A pseudogap which may influence the shape of the superconducting dome was also suggested for K-substituted pnictides by ARPES measurements [37].

Pressure studies and structural effects

If a quantum critical point exists, one may be able to locate and study it by determining the shape of higher dimensional phase diagrams which include the pressure and magnetic field dependencies in addition to the charge carrier density. On the other hand, if a quantum critical point does not exist, and if no other interesting effects are uncovered by creating these higher dimensional phase diagrams, the experiments are nonetheless meaningful in determining under what conditions superconductivity appears and disappears - effectively in reducing the number of relevant parameters needed to describe the physics.

One relevant question in studying these types of materials is: does T_c increase further by pressure than is attainable by chemical substitution? This seems to be the case for most cuprates, which is suggestive that the charge density is not the only parameter which determines the maximum T_c. Detailed pressure studies have suggested that T_c might be increased by in-plane compression of the CuO_2 planes [38]. A comparable finding is that in the iron-based superconductors, pressure can drastically enhance T_c of FeSe, from 8K to 37K ; the maximum T_c occurs close to the pressure at which the structure is most highly three-dimensional in terms of a high value of the ratio $(a + b)/2c$ [39].

It has also been reported that the anion height from the iron plane exhibits the value of a perfect tetrahedron at the optimal value of T_c in many iron based superconducting materials [40]. However, the pressure study on FeSe previously mentioned seems to conflict with this finding [39]. As in the cuprates, the structural symmetry is altered close to the

onset of superconductivity in many iron based superconductor families: orthorhombic order coexists with superconductivity in a narrow concentration window in $BaFe_2As_2 : Co$ [41] and in $FeSe_{1-x}Tex$ [42]. Determining the role, if any, of structural degrees of freedom on the superconductivity of iron-based materials is therefore an important task.

Limitations of phase diagrams for theory of superconductivity

Experimental physicists hope that their work is central to understanding the underlying physics, and that their efforts help to guide theory. Determining phase diagrams does give stringent conditions for the superconducting mechanism. However, the shape of the phase diagram alone is not necessarily sufficient to distinguish models of superconductivity. For instance, a spin density wave phase also exists in the parent compounds of the organic superconductors, which is suppressed, giving rise to a dome structure in T_c for organic superconductors. In the case of the organics, the superconductivity might be explained by a bipolaronic mechanism in which electron pairing occurs on short length scales as compared with BCS superconductors [43]; bipolarons appear as solutions to the Hubbard model containing significantly strong attractive interactions [44, 45]. Within this model, a superconducting dome can occur either as a function of electron concentration or electron-phonon coupling strength. Thus many theorists were interested in applying the bipolaronic theory to the cuprates, given the similarity of their phase diagrams as compared with the organic superconductors. Recently, however, some of the key authors who originally proposed the bipolaronic mechanism of superconductivity for the organic superconductors have refuted its application to the cuprates because the effective masses of hypothetical bipolarons, which are determined from the hopping energies which are roughly equal to the energies of local phonon modes, produce very small superconducting critical temperatures [46]. Another way to consider this inconsistency is that an incorrect physical explanation can generate an accurate phase diagram if the parameters are tuned to arbitrary values. Thus, phase diagrams are only part of the experimental toolkit necessary to elucidate mechanisms of superconductivity.

1.6   Summary and Overview of Document

Not knowing the theory which governs superconductivity, there is not a clear way to raise the critical temperature. This, however, is not new - while the equations of BCS theory may ostensibly be seen to give a prescription to find higher temperature superconductors, the major successes of increasing T_c came from experimental work following what I previously called 'control rules', since they are not based firmly on principles, but empirical; such as allowed Matthias and others to discover new higher T_c superconductors 'in spite' of BCS [47]. One hopes that experimental investigations might ultimately elucidate similar control rules for superconductivity which could eventually be consolidated and refined by theorists;

and that perhaps feedback between these two efforts could lead to a satisfactory theory of superconductivity.

An overview of this document is as follows. Chapter 2 will discuss experimental techniques we use and what can be learned using them. Chapter 3 discusses the nature of the structural and magnetic phase transitions in $BaFe_2As_2$ extracted from single crystal x-ray diffraction measurements which were performed with synchrotron light; I participated in these experiments with Tom Forrest. Chapters 4 and 5 include two papers on which I collaborated with Meng Wang in order to determine the basic physical properties and nature of the spin wave excitations of these materials. Finally, I worked on a phase diagram of a non-superconducting compound series iron telluride with copper substitution, which, similar to the superconductors, exhibits intriguing interconnections between the magnetism, structure, and electronic degrees of freedom, which appears in Chapter 6.

Bibliography

[1]   Y. Kamihara *et al.*, J. Am. Chem. Soc. **130**, 020503 (2008).

[2]   H. Hosono, J. Phys. Soc. Jpn. **77**, Suppl C pp 1-8 (2008).

[3]   D.J. Singh, Physica C **469**, 418-424 (2009).

[4]   A. Subedi, L. Zhang, D.J. Singh, M.H. Du, Physical Review B. **78**, 134514 (2008).

[5]   F.C. Zheng, T.M. Rice, Physical Review B. **37**, 3759 (1988).

[6]   A.P. Drozdov, M.I. Eremets, I.A. Troyan, arXiv:1412.0460 (2014).

[7]   S.L. Bud'ko *et al.*, Phys. Rev. Lett., **86**, 1877 (2001)

[8]   A.P. Ramirez *et al.*, Phys. Rev. Lett., **68**, 1058 (1992)

[9]   B. Batlogg *et al.*, Phys. Rev. Lett., **58**, 2333 (1987)

[10]   L.C. Bourne *et al.*, Phys. Rev. Lett., **58**, 2337 (1987)

[11]   K.J. Leary *et al.*, Phys. Rev. Lett., **59**, 1236 (1987)

[12]   R.H. Liu *et al.*, Nature Lett., **459**, 64 (2009)

[13]   P.M. Shirage *et al.*, Phys. Rev. Lett., **103**, 257003 (2009)

[14]   R. Khasanov *et al.*, New J. Phys. **12**, 073024 (2010).

[15]   Y. Tsuge, A. Iyo, Y. Tanaka, H. Eisaki, T. Nishio, Physics Procedia **36**, 731 (2012)

[16]   E. Rodriguez *et al.*, Chem. Sci., **2**, 1782 (2011)

[17]   A. Wittlin *et al.*, Supercond. Sci. Technol. **25**, 065019 (2012)

[18]   E. Pomjakushina *et al.*, Phys. Rev. B , **80**, 024517 (2009)

[19]   T.H. Geballe, B.T. Matthias, IBM Journal **April**, 256 (1962)

[20]   P. Morel, P.W. Anderson, Physical Review **125**, 1263 (1962)

[21]   C.W. Chu *et al.*, arXiv:1504.02488 (2015)

[22]   B. Batlogg *et al.*, Phys. Rev. Lett. **61**, 1670 (1988)

[23]   J.M. Harris *et al.*, Phys. Rev. Lett. , **54**, R15665 (1996)

[24]   Y. Kamihara *et al.*, J. Am. Chem. Soc., **128**, 10012 (2006)

[25]   D. Mandrus *et al.*, Chem. Mater. , **22**, 715 (2010)

[26]   A. Aharony *et al.*, Phys. Rev. Lett., **60**, 1330 (1998)

[27]   C. de la Cruz *et al.*, Nature, **453**, 899 (2008)

[28]   J. Rossat-Mignod *et al.*, Physica C , **86**, 185 (1992)

[29]   S. Chi *et al.*, Phys. Rev. Lett., **102**, 107006 (2009)

[30]   I. I. Mazin *et al.*, Phys. Rev. Lett., **101**, 057003 (2008)

[31]   D.M. Broun, Nature, **4**, 170 (2008)

[32]   S. E. Sebastian *et al.*, Proc. Nat. Acad. Sci., **107**, 6175 (2010)

[33]   P. Walmsley *et al.*, Phys. Rev. Lett., **110**, 257002 (2013)

[34]   D. Hu *et al.*, Phys. Rev. Lett., **114**, 157002 (2015)

[35]   J. L. Tallon *et al.*, Phys. Stat. Sol., **215**, 531 (1999)

[36]   G. Zheng *et al.*, Phys. Rev. Lett., **94**, 047006 (2005)

[37]   Y.-M. Xu *et al.*, Nat. Comm., **2**, 392 (2011)

[38]   J. S. Schilling, Frontiers of High Pressure Research II: Application of High Pressure to Low-Dimensional Novel Electronic Materials, Nato Science Series **48**, 345 (2001)

[39]   S. Margadonna *et al.*, Phys. Rev. B, **80**, 064506 (2009)

[40]   C.-H. Lee *et al.*, J. Phys. Soc. Jpn., **77**, 083704 (2008)

[41]   D. K. Pratt *et al.*, Phys. Rev. Lett., **103**, 087001 (2009)

[42]   A. Martinelli *et al.*, Phys. Rev. B, **81**, 094115 (2010)

[43]   B. K. Chakraverty and J. Ranninger, Philosophical Magazine B, **52**, 669 (1985)

[44]   S. Robaskiewicz *et al.*, Phys. Rev. B, **23**, 1447 (1981)

[45]   M. H. Cohen *et al.*, Phys. Rev. B, **29**, 4496 (1984)

[46] B. K. Chakraverty *et al.*, Phys. Rev. Lett., **81**, 433 (1998)

[47] B. T. Matthias, Physica, **51**, 69 (1971)

Chapter 2

Experimental Techniques

2.1 Crystal growth: routines for new syntheses

Working in Bob's group we have had a constant influx of postdocs, and about a half of them have no growth experience when joining the group: synthesis is a skill many learn as they go. In our efforts to grow materials we have benefited greatly from working in Edith's lab, and particularly from interacting with the scientists and engineers in her group have been essential to our efforts including Gautam Gundiah, Zewu Yan, Chris Ramsey, Steve Hanrahan, Yetta Porter, Ramesh Borade, Katie Brennan, and Najeb Abdul-Jabbar. In the following paragraphs I will summarize some routine procedures for beginning a new growth.

Choice of furnace

Before doing any growth, choice of a furnace is very important. The furnace should allow for modification of the thermal and environmental parameters as needed for any experimental variations one might want to perform in the growth, i.e. raising the temperature, changing the size of the crucible, flowing gas and/or maintaining a leak-free environment so as not to react with a Tantalum crucible, for instance. In designing a Bridgman furnace, we decided to translate the furnace over the alumina tube, rather than translating the sample through a static zone, to minimize vibrations to the sample - see the figure below for a picture. Characterization of the thermal profile of the chosen furnace with a thermocouple is essential: many months in, one of our postdocs was upset to find that his reactions may have failed because the furnace temperature was not reaching its setpoint. When characterizing the thermal profile, one should pay attention to the location of the gradients, if directional solidification is desired. The thermal profile can be modified by changing the insulation. For the 8 inch, horizontal, single zone furnaces in Edith's lab, it was necessary to remove insulation in order to achieve directional solidification. Doing so produced a temperature 60 to 100°C lower than the setpoint of 1100 °C over the rear four inches of the furnace; without removing this insulation, the gradient is about one half to one third this size, where differences may depend on how well sealed the alumina tube is - this condition is preferable

Figure 2.1: A Bridgman furnace I helped to design, in use May 2015

for solid state reactions, or melting reactions in which a uniform temperature profile is desired. The thermal gradient will also be affected by gaseous flow. When we initially set up the vertical Bridgman furnace pictured below, we found that the maximum temperature gradient which could be achieved at 1000 °C was about 50°C per inch - decently high, but not excellent. After adding additional alumina foam, and after Chris Ramsey fabricated new flanges to keep the alumina tube airtight and heat shields, which primarily exist to protect the flanges, we were able to increase the maximum gradient to 70°C per inch in the presence of a small but steady Argon gas flow of several cc/min.

Collection of background information on materials

Searching the ASM phase diagram database is a good way to begin learning about growth of a new compound. First, we collect all information about the targeted phase and nearby impurity phases by searching known binary and ternary phase diagrams. From the phase diagrams we try to deduce a good reaction sequence. Solid-solid transitions of either the main phase or impurity phases can cause a crystal to shatter, so that we try to avoid crossing these transitions when unnecessary. I try to account for possible variation of these transition temperatures with slight solubility of other species in the impurity phases. We may also wish to consider the rate of freezing with temperature – Fisher et. al [1] for instance argue that one should consider that, since the nucleation rate is proportional to the inverse of the slope of the liquidus line, one should expect that crystals which nucleate over a range of temperatures are less strained, as compared with the case of a liquid which freezes uniformly at a single temperature. Another consideration if the compound does not melt congruently at a suitable temperature given the furnace and crucible options is whether flux be used

to either lower the reaction temperature or otherwise alter the phase diagram such that congruent melting becomes possible. Important parameters in the choice of a flux may include the difference between the melting or boiling points of precursors, reactivity of the flux with other precursors and/or the crucible, and details of the flux incorporation and removal [2].

Secondly, we consider which species in the compound may be volatile and/or reactive. One example of a bad reaction is that in synthesizing the pnictides containing alkalai metal, caution has to be used in preparing the stoichiometric 1:1 arsenide binaries of the alkalai metals without producing other phases, which will disrupt the subsequent crystal growth reaction. Another example of reactivity: it seems likely that it is the fluoride precursor BaF_2 in the synthesis of $Ba_2F_2Fe_2OSe_2$ which is responsible for the strong reaction with quartz; we found that simply placing the powder in alumina, removing direct contact of the material with the quartz wall allowed the synthesis to be completed; however, additional devitrification was minimized by sealing the precursors inside an alumina crucible using alumina paint.

An example of volatility is that in growing $FeSe_{0.4}Te_{0.6}$, we also observed that when we melt the Fe-Se-Te mixture together and raise it to around 900 °C, the mixture emits a dark vapor, possibly Te, which coats the walls of the quartz. The as-grown boules sometimes occur with pores, which can be reduced by pre-melting reactions as described in the paper later in this thesis, or by using binary precursors; doing so, we obtain large crystals weighing about 90 percent of the original mass of precursors. However, in my experience, using binary precursors to synthesize $FeSe_{0.4}Te_{0.6}$ resulted in samples with low volume fraction superconductivity. Pores, being three-dimensional, are nonequilibrium defects, which is one reason we can work to minimize them by clever synthesis techniques. While these pores are comprised of local vacancy clusters, and while an equilibrium vacancy concentration will exist in any material, it is not known at present to what extent the possible variations in the chalcogen vacancy concentrations affect the properties of these materials. Some groups have reported that Se vacancies occuring in FeSe at the level of a single percent will determine the occurence of superconductivity [3]. Potentially related to this, annealing in the chalcogen vapors has been shown to change the properties of some iron chalcogenides [4]; however, this effect might also result from a reduction of the interstitial site occupancy. Chalcogen vacancies are known to exist in a variety of other materials [5, 6, 7] so it would not be surprising to find that they also exist in the iron chalcogenides, although it is difficult to establish their existence by refinement, for instance, given that these materials are known to incorporate a nonstoichiometric occupancy of metal in their crystal structures. However, our main point here has been to suggest that the volatility of chalocogen species is one parameter which should be considered during the growth process.

Precursors

Solid state reactions occur at boundaries between phases, so the form of the material, i.e. particle size is important, although reducing particle size may increase the oxidation rate,

which is noticeable for many metals such as Fe, Ba, Sr, Ca, FeAs, etc even when the glovebox is kept under optimal conditions. Se/Te pieces also react with air, and caution should be used to keep them fresh, such as sealing them with parrafin even within the glovebox. Copper also readily absorbs oxygen, and in the synthesis of $Fe_{1+\delta}Te : Cu$, we noticed that the magnetic signal at low fields from what is presumably Fe_3O_4 was reduced upon substituting 8N copper sheet for the very fine 4N powder. Powders can be sieved and pressed if necessary which will increase their contact area and enhance the solid state reaction rate. This was done for each of the three reactions to make $Ba_2F_2Fe_2OSe_2$ as described in the reference [8] - we performed x-ray diffraction incrementally after each reaction and found that the third reaction is indeed necessary to fully form the product.

Crucibles

There are many choices of crucible specific to certain syntheses; but for most of the reactions we have done using pnictides and chalcogenides, the syntheses have been carried out in quartz, alumina, or tantalum. Two families I've synthesized, the '11' type $Fe_{1-x}Cu_xSe1 - yTey$ and $CaFe_2As_2$, each cause the quartz to crack upon cooling, presumably due to strong surface interactions of the melt with the quartz. Particularly for $CaFe_2As_2$, this was very surprising as for $BaFe_2As_2$ and $SrFe_2As_2$, the reactions can be carried out in a single crucible. An inner crucible of either alumina or quartz is therefore necessary to consistently complete these reactions under vacuum. Another trick we used to extend quartz to higher melting temperatures, i.e. above 1180 °C, is to carburize it by evaporating a solvent on the quartz using a hydrogen-oxygen flame. This can be useful if it is possible to carburize only the section of quartz which will be exposed to high temperature, and not the part which will be sealed, as the quartz can become difficult or impossible to seal using the hydrogen/oxygen flame.

The thermal and environmental properties inside of a sealed quartz tube can also be modified by the presence of an exchange gas, such as argon or helium, by the choice of crucible type and dimensions, and by the presence of quartz wool as insulation within the crucible. When available, helium exchange gas may be preferable to argon as it has a higher thermal conductance. Oxygen may be minimized by sealing a getterer such as carbon inside the quartz, as is done in the synthesis of FeSe powders [9]. Tantalum foil can be used to prevent materials from contacting quartz if reactions occur; and doing so does not result in other unwanted reactions of the material with tantalum. Searching the ASM phase diagram database, we find that Tantalum can form a variety of binary compounds with chalcogens and with arsenic. Tom Forrest's samples of $BaFe_2As_2$ which he annealed in Ta foil were visibly duller after annealing, and he noted a corresponding change in the FWHM of the $(0, 0, L)$ reflections. However, WDS did not indicate the presence of tantalum on the crystal surface. Thus, we still do not know whether Tantalum reactions could be partly responsible for these changes in the apparent surface quality.

2.2 Powder diffraction and Rietveld refinement

When doing powder diffraction for Rietveld refinement, as with many other diffraction techniques, one can either aim to collect data with high intensity or with high resolution. The choice will depend on the parameters to be refined.

Typically I use the lab x-ray diffractometers to collect positional data which determines the phases present, as well as their volume ratios and lattice parameters. When taking such measurements, a positional calibrant which can be measured simultaneously to the sample should be mixed in. A good sample mount is critical in reducing the background to observe low-intensity peaks and to obtain better data for refinement, and 3° off-axis quartz is an expensive, but suitable choice as it is fairly transparent to x-rays. Strong c-axis plate type preferred orientation of many iron chalcogenide powder samples makes it difficult to trust refinements of additional structural parameters of the main phase beyond the lattice parameters, especially since in these materials the other free parameters we are interested in are z positions, which cause a similar group of reflections to vary in intensity as does preferred orientation. We observed such strong effects even when using careful sample preparation techniques recommended by scientists at Argonne; after sieving the samples through a 22 micron mesh, the powders were either mixed in acetone, stirred, and dispersed as they dried, or were lightly sprinkled onto a surface. However, these techniques still resulted in samples with large orientation effects with March-Dollase factors. The preferred orientation is much weaker in the large samples volumes used with neutron powder diffraction. Therefore from this standpoint, neutron diffraction is a better tool for refining detailed parameters of the iron based superconductors and related materials. Had I continued trying the x-ray powder diffraction measurements, the next logical step to reduce preferred orientation would have been to disperse the sample in a lacquer which could be sprayed as an aerosol, or cast into an aerogel.

Hui Wu at NIST suggested the following order of refinement variables, which was used in the neutron powder diffraction refinements in the paper on $Fe_{1+\delta}Te : Cu$ which occurs later in this thesis. First refine scale, which we always keep refining; then add in a cosine Fourier series background function (GSAS type 2), increasing the number of parameters progressively from 9 up to at least 14; then refine the lattice parameters in three cycles, then do one cycle of refinement including the lattice parameters and the zero point. Following, refine the site parameters with the strongest scatters first: first refine all positions, then all thermal factors, then all occupancy factors. Sometimes thermal factors, background, and occupancy fractions can correlate, thus a cautious procedure must be employed in order to refine these individually and iteratively. Following, refine the profile coefficients, U, V, and W, one at a time. Then add X and Y while refining U, V, and W. From this point on, we keep the previously mentioned parameters active during further refinements unless otherwise specified. Next, we add anisotropic broadening terms one by one if necessary, which is determined by observing whether in the calculated pattern there are some peaks which overestimated widths and simultaneously others which underestimated the widths. In the final steps of refinement, since we have already obtained nearly stable values of the

parameters thus far listed, we should go back and repeat the above refinements, checking for large correlated parameters at every step. If correlations are observed then we must continue the refinement in a more gradual process, refining the correlating parameters separately and iteratively. Once a convergence is achieved again, we shold also check the stability of the solutions by removing all profile parameters from the refinement and refining the atomic factors all at once, and then the thermal factors all at once, again performing iterative refinements with any correlating parameters until convergence is achieved. In the final step, we add in the preferred orientation, which tends to correlate with atomic factors and thermal factors, and repeat the iterative refinements until convergence is achieved.

This is the process we followed for refinements, using a variety of different structural starting models. For each of our neutron powder diffraction refinements, we obtained convergent solutions as described in our paper on copper substituted iron telluride; solutions which could not be distinguished by the goodness of fit are also described therein.

2.3   SEM and WDS

WDS is superior to SEM in that the energy resolution is higher, thus the accuracy of the measurement is much better; in addition, it can probe light elements such as fluorine. The SEM machine, however, has better availability. The SEM in the geology department at Berkeley, at LEO-430, does not have a 'monitor' to detect the incident electron beam current, and so this introduces additional uncertainty into the measurement. The expensive elemental standards which might be used to determine the oxidation state of an element are kept with the WDS machine, as they are necessary for calibration as only a small window of energies is measured at once. These can be used with SEM to maximize the precision, but we always calibrated the energy to the Kα fluorescence lines of Al and Cu, simultaneously.

To get accurate composition measurements from these techniques, the flatness of the surface is important. If one wishes to improve the precision of the measurements for either technique, one should cast the sample into a resin, and then sand the resin down until the sample surface is exposed.

2.4   Susceptibility

Basic discussion of PPMS and MPMS measurements

The bulk of the susceptibility measurements I've performed during my PhD have used the DC susceptibility option of a Quantum Design PPMS system, although I've occasionally used the AC option for T_c checks when a SQUID was not available. On occasion I have also used a Quantum Design MPMS which employs SQUID technology to obtain high quality susceptibility data; for example, to observe hysteresis in the transition temperature of $Fe_{1+\delta}Te$. Tom Forrest also used a SQUID to investigate the effects of annealing on the phase

transitions of $BaFe_2As_2$ in a paper which appears later in this thesis, and the improved accuracy of the measurement with respect to PPMS measurements helped to reveal the subtle broadening of the transition due to impurities which could be removed by annealing.

Both the PPMS and MPMS measurements employ DC extraction magnetometry, which uses a gradiometer in order to isolate the signal arising at the sample from that of other sources. The gradiometer consists of two sets of counterwound inductors wired in series: as the magnetic field from a dipole falls off as the inverse cube of distance, objects far outside the coilset produce DC fields which are rejected by the inductors if they are balanced. The PPMS uses an additional set of detection coils along with a low-inductance calibration coil to detect the magnetic field gradient as the sample is traveling through the extraction path, while the MPMS uses a SQUID to detect the change in flux; a transformer coupled to the measurement device mirrors the current therein; the signal can then be amplified and filtered to produce the data. SQUIDs may ultimately be sensitive to fields as low as 10^{-17}T, which is five orders of magnitude smaller than non-SQUID sources - more details are available in this reference [10].

We typically measure plate-like antiferromagnetic single crystal samples - for these, the PPMS can be used for samples of size roughly 10mg and above. Given the high sensitivity, SQUID measurements can be used on much smaller samples. SQUID measurements are actually much faster than PPMS measurements as less sampling is required due to the lower measurement noise. The lower noise also leads to cleaner data, so the SQUID is highly preferable for magnetic measurements.

2.5   Resistance

We have used the standard four-point probe method to measure resistance. To maximize the resistance for this measurement, and hence minimize the noise, the sample geometry should have a long length and a small area – a long rectangular shape, with contacts which are thin which along the length, but traversing the width of the sample ensure a homogeneous current and potential profile for a homogeneous sample - this configuration is known as a Hall bar. Sputtered contacts may increase the contact adhesion/stability. Silver paste reacts with chalcogenides, so Ti/Au contacts were sputtered under a high vacuum for our resistance measurements, as described in the paper on iron tellurides in this thesis.

2.6   Elastic x-ray diffraction and neutron diffraction on single crystals: application to phase transitions

Our group specializes in using x-ray and neutron diffraction to study thermodynamics. As there are many excellent references for x-ray and neutron diffraction, I will try to focus on a short overview of the application of elastic scattering techniques to phase transitions, especially concerning the antiferromagnetism and structural orders in systems which have

been studied in this thesis. In this way I hope to consolidate the research we have done, as well as to emphasize experimental limitations, and perhaps reveal remaining problems.

Phase transitions, critical points and coupling of order parameters

An order parameter is an experimentally observed quantity which quantitatively describes the progression of a phase transition. The order parameter is chosen to represent the symmetry broken with respect to the phase transition being studied. Therefore, the order parameter should have zero or at least constant intensity in the high temperature phase, and saturate when the transition is completed; where the case of constant intensity can be subtracted to define an order parameter with value zero in the high symmetry phase. A typical order parameter for the tetragonal to orthorhombic transition observed in many iron based superconducting materials is the lattice parameter splitting, defined as the difference divided by the average of the split lattice parameters, while for the paramagnetic to antiferromagnetic transition, the typical order parameter is the sublattice magnetization.

Now we shall discuss what can be understood physically from the order parameters. Stephen Wilson's original work on the phase transitions in $BaFe_2As_2$ observed that the intensity of the magnetic and structural order parameters in the parent material mimic each other; thus he proposed a model wherein both the magnetism and structure are treated on equal footing, rather than one being the primary order parameter, which would imply a linear-quadratic coupling [11]. A Hamiltonian was thus proposed which contains a biquadratic term in strain and magnetization, which allows for both transitions to be second order, as Stephen Wilson inferred from his experiments, but also implies the existence of a tetracritical point in the phase diagram. Further work has shown that a linear-quadratic strain-magnetization term is necessary to describe the magnetic transitions for the parent compound, which are actually first-order [12], but only have hysteresis in a small temperature window which Stephen did not measure. The interpretation of the new term is that the structural transition arises due to an emergent Ising degree of freedom which couples the interpenetrating antiferromagnetic checkerboard sublattices; this coupling constant can be nonzero in the presence of strong magnetic fluctuations above the phase transition, i.e. where the static ordered moment does not exist. Thus, this model describes the observation that the structural order parameter may begin as a second order phase transition, but is joined by first-order magnetic transition which couples to the structure, as was observed independently from the work at Ames Lab, and first published by our group [13].

Furthermore, Min Gyu Kim's work at Ames Lab and Costel Rotundu's work at Berkeley established the existence of a magnetic tricritical point in the Co-substitution series of $BaFe_2As_2$ [12, 14]. A tricritical point is defined as the point at which three critical lines meet, for example, in the phase diagram of $He_3 - He_4$, and in compounds which exhibit metamagenetic-antiferromagnetic transitions, such as Dy-Al garnets or $FeCl_2$ as a function of applied field, [15]. Alternatively, a tricritical point may be described as a point at which three phases become identical. For the case of the metamagnet-antiferromagnetic transitions, an applied magnetic field can couple to the staggered magnetization of the antiferromagnet,

generating an effective staggered field which couples linearly to the order parameter in the metamagnetic phase. The three phases which become identical are the normal antiferromagnetic phase, and the two metamagnetic phases for which the staggered field couples to the antiferromagnetic order in the positive and negative sense [16]. Thus, the first-order phase boundary represents the distinguishibility of these phases, which requires a latent heat and a coexistence regime. If a first order to second order transition in an antiferromagnet occurs as a function of some tuning parameter such as the defect concentration or dopant density then according to the theoretical models, if one could generate an effective field on the staggered magnetization, three phases would become one at this point which would hence be tricritical.

Tom Forrest's work at Berkeley, which I participated in and which appears in a later chapter of this thesis, has further demonstrated the existence of a tricritical point in the structural phase transition as a function of the defect or dopant concentration, which is observed experimentally as a function of annealing [17]. Specifically, while as-grown samples of $BaFe_2As_2$ exhibit a continuous structural transition which coexists with first-order structural peaks at a magnetic transition at a temperature slightly lower than the onset of the continuous structural transition, after sufficient annealing which is 46 days, the sample exhibits a first-order transition only, i.e. there exists no continuous splitting to within 0.1K of the first-order magnetostructural transition. This suggests that the appearance of a continuous structural transition which is above the Neel transition may only exist due to defects, or rather, that the Neel transition is more strongly suppressed due to defects. It may also suggest that the detailed effects of uniaxial pressure on the magnetic and structural transition temperatures in $BaFe_2As_2$, which will each be discussed in the following paragraph, might be sensitive to the defect concentration.

Uniaxial in-plane pressure experiments introduce a field which couples linearly to the structural order parameter, causing the structural order to occur above the pressure-free transition temperature; interestingly, the magnetic transition temperature also rises slightly [18]. The increase in the magnetic transition temperature under 2MPa in-plane pressure is suggested to be a constant of the system with respect to cobalt concentration; however since the Neel temperature at zero pressure is suppressed with increasing cobalt concentration, the ratio of the pressure increase of the transition temperature to the Neel transition temperature at zero pressure diverges as a function of cobalt concentration [19]. One of the details which might depend on level of annealing is the evolution of the critical exponents, for instance, which are cited in [19].

Random Fields

The random field model is a theoretical model which describes the effects of disorder in the field conjugate to the order parameter on phase transitions. To the usual spin interactions on a lattice is added at each site a small random field, which introduces a local random energy superimposed on top of the underlying spin structure with its exchange interactions. But even if the random field contribution to the energy is much smaller than the exchange terms, the random field terms will induce different behavior locally, such as the formation

of domain boundaries [20]. Neutron scattering can be used to determine the shape of the phase boundary and the line of phase transitions as a function of field, $T_N(H)$, which in the model scales with field depending on the dimensionality of the system; for a 3D Ising system the suppression of the Neel temperature goes as $T_{N,H} - T_{N,0} \propto H^{1.43}$. Furthermore, neutron scattering can be used to determine the domain size if it is not too small. Scaling of the correlation length and structure factor at the transition temperature should also occur as a function of field, again, if these can be observed. The dynamical correlation length may also be obtained by inelastic measurements. Finally, one may study the effect of another thermal treatment: quenching, on the phase transition. All of these are summarized in the review article [21].

Having observed behavior consistent with a random field effect in $Fe_{1+\delta-x}Cu_xTe$ with x=0.06, a composition at which the magnetic transition occurs as second-order, an applied field which couples directly to the staggered magnetization of the antiferromagnetic phase should not produce different phases, as we discussed above in terms of a tricritical point – an applied field can only generate distinguishable phases if the magnetic transition is first-order. Then why do random field effects change the properties of the system? It seems that this is simply because the order parameter cannot fully develop in the presence of random fields - the system is held far away from its equilibrium state; yet this has effects on the quasi-equilibrium collective phenomena [20].

2.7 Inelastic neutron scattering measurements: critical fluctuations, quantum criticality, and spin value extraction

Inelastic neutron scattering has been reviewed by many authors; therefore, similar to the elastic scattering section, I will briefly dicusss the application of inelastic neutron scattering measurements relevant to phase transitions: which is known as the study of critical behavior. Fortunately I had the chance to interact with Stephen Wilson and Min Gyu Kim on triple axis experiments which investigated critical fluctuations.

Additionally, I will discuss time of flight measurements in which I have participated with Meng Wang, from which, knowing the magnetic structure, one can extract the quantum spin value S and the exchange interactions.

Critical fluctuations

Initially, during his work on the phase transitions in $BaFe_2As_2$, Stephen noticed that the critical exponent of the magnetic order parameter corresponded to that of a 2D-Ising model. Then the question arose: why should the system scale as a 2D system when the magnetic order occurs as a 3D peak? This led him to search for and find evidence of 2D

critical fluctuations which build up at T_N [22]. Thus the concept from this paper is that 2D magnetic interactions drive both the 3D structural and magnetic transitions.

At the time of writing this thesis, Min Gyu is studying possible quantum critical fluctuations of Ba122:Cu. One signature of such fluctuations is E/T scaling as observed in the cuprates [23] and in heavy fermion compounds [24]. Another signature is a divergent length scale which should occur at zero Kelvin at a certain composition. However, an experimental demonstration of a divergent length scale as the temperature is lowered, to the knowledge of our group in May 2015, has not been found. At most, the length scale diverges by a factor of three, although the peak amplitude does appear to diverge by two orders of magnitude over an order of magnitude change in the temperature [23]. One may suspect that to observe the length scale divergence, the sample composition would have to be very close to the critical point without crossing it; but obtaining a sample which has such a precise composition, and to have that level remain uniform throughout its volume may be challenging. There may be other crossover behaviors which determine whether one is close to a quantum critical point, which Min Gyu is currently investigating.

Susceptibility, quantum spin value S, and exchange constants J

Integrating the spin excitations over all $\mathbf{q}$ within a Brillouin zone and averaging, one obtains the dynamic susceptibility as a function of energy. In the $Rb_{0.8}Fe_{1.5}S_2$ paper which appears later in this thesis, this integration is taken over three branches of spin excitations, which exist because there are three distinguishable iron atoms within the unit cell. The total fluctuating moment is obtained by a simple integration of the dynamic susceptibility with respect to energy [25]. The static ordered moment is obtained through the weight of the magnetic peak per unit mass of the phase, normalized to vanadium incoherent scattering which gives absolute scattering units. Combining these, the total moment size is obtained as the root of the sum of squares of the static and fluctuating moments, which is proportional to the size of the spin via the moment sum rule [25].

Determining the exchange couplings is a somewhat less trivial task. One begins with the magnetic structure. Comparisons of models to data are made by calculating the dispersions along the high symmetry directions of the magnetic Brillouin zone. The signs of exchange interactions determine the symmetry of the magnetic structure, which is reproduced in the dispersion relations; the relative magnitudes of the exchange interactions determine the spin-wave energies at different positions in the Brillouin zone, and their absolute magnitude is also determined by fitting to the total scattering per unit mass of the phase, normalized to vanadium incoherent scattering to obtain absolute scattering units.

Bibliography

[1]   I. R. Fisher, M. C. Shapiro, and J. G. Analytis, Philosophical Magazine, **92**, 2401 (2012)

[2]   Z. Fisk and J. P. Remeika, Handbook on the Physics and Chemistry of Rare Earths, **12**, 53 (1989); B. M. Wankyln, J. Cryst. Growth, **37**, 334 (1977); M. G. Kanatzidis *et al.*, Angnew. Chem. Int. Ed., **44**, 6996 (2005); P. C. Canfield and Z. Fisk, Phil. Mag. B., **65**, 1117 (1992); D. E. Bugaris and H.-C. zur Loye, Angnew. Chem. Int. Ed., **51**, 3780 (2012)

[3]   E. Pomjakushina *et al.*, Phys. Rev. B , **80**, 024517 (2009)

[4]   W. Lin *et al.*, Phys. Rev. B, **91**, 060513R (2015)

[5]   S. D. Setzler *et al.*, Appl. Phys. Lett., **70**, 2274 (1997)

[6]   G. Salviati and D. Seuret, Thin Solid Films, **104**, L75 (1983)

[7]   Y.S. Hor *et al.*, Phys. Rev. B, **79**, 195208 (2009)

[8]   H. Kabbour *et al.*, J. Am. Chem. Soc., **130**, 8261 (2008)

[9]   A. J. Williams *et al.*, J. Phys.: Condens. Matter, **21**, 305701 (2009)

[10]   R. L. Fagaly, Rev. Sci. Instrum., **77**, 101101 (2006)

[11]   S. D. Wilson *et al.*, Phys. Rev. B, **79**, 184519 (2009)

[12]   M. G. Kim *et al.*, Phys. Rev. B, **83**, 134522 (2011)

[13]   C. R. Rotundu *et al.*, Phys. Rev. B **82**, 144525 (2010)

[14]   C. R. Rotundu and R. J. Birgeneau, Phys. Rev. B, **84**, 092501 (2011)

[15]   R. B. Griffiths, Phys. Rev. Lett., **24**, 715 (1970)

[16]   N. Giordano and W. P. Wolf, Phys. Rev. Lett., **39**, 342 (1977)

[17]   T. R. Forrest *et al.*, submitted (2015)

[18]   C. Dhital *et al.*, Phys. Rev. Lett., **108**, 087001 (2012)

[19]   C. Dhital *et al.*, Phys. Rev. B, **89**, 214404 (2014)

[20]   D. S. Fisher, G. M. Grinstein, and A. Khurana, Physics Today, 56 (December 1988)

[21]   R. J. Birgeneau *et al.*, Physica **137B**, 83 (1986)

[22]   S. D. Wilson *et al.*, Phys. Rev. B **82**, 144502 (2010)

[23]   G. Aeppli *et al.*, Science **278**, 1432 (1997)

[24]   A. Schroeder *et al.*, Phys. Rev. Lett. **80**, 5623 (1998)

[25]   G. Shirane, S. M. Shapiro, and J. M . Tranquada, Neutron Scattering with a Triple-Axis Spectrometer, (Cambridge University Press, 2004)

Chapter 3

The Effects of Post-Growth Annealing on the Structural and Magnetic Properties of $BaFe_2As_2$

3.1   Introduction

Much of the background of this project was discussed in the sections on neutron scattering in the experimental chapter of this thesis. It will suffice here to state here that Tom Forrest participated in the original measurements which uncovered that the structural transition begins as second-order but becomes first-order at a lower temperature. Being aware of Costel's observations of unusual evolution of the heat capacity spectra to annealing, Tom and I undertook to study the effects of annealing on the phase transitions by x-ray diffraction, which has much better resolution than neutron diffraction, and hence is a more sensitive probe for subtle transitions such as the present one. Our work uncovers a tricritical point in the structural transition: specifically, while for as-grown samples the structural transition begins as second order and becomes first-order at the magnetic transition, which occurs at a lower temperature, the separation between these two transitions closes as a function of the annealing time, and for well annealed samples, the transitions merge to within 0.1K. When they do so, the initially-continuous splitting of the structural peak is not observed; the unbroadened tetragonal structural peak simply lowers in intensity and briefly coexists, in a 0.8K range, with the first-order orthorhombic peaks.

At the time of preparing this dissertation, the current draft has been submitted to Phys. Rev. B.

3.2   Paper

The effects of post-growth annealing on the structural and magnetic properties of $BaFe_2As_2$

T. R. Forrest,[1] P. N. Valdivia,[2] C. R. Rotundu,[3] E. Bourret-Courchesne,[4] and R. J. Birgeneau[1, 2, 3]

[1]*Department of Physics, University of California, Berkeley, CA 94720, USA**
[2]*Department of Materials Science and Engineering,*
University of California, Berkeley, CA 94720, USA
[3]*Materials Sciences Division, Lawrence Berkeley National Laboratory, Berkeley, CA 94720, USA*
[4]*Life Sciences Division, Lawrence Berkeley National Laboratory, Berkeley, CA 94720, USA*
(Dated: August 4, 2015)

We investigate the effects of post-growth annealing on the structural and magnetic properties of $BaFe_2As_2$. Magnetic susceptibility measurements, which exhibit a signal corresponding to the magnetic phase transition, and high-resolution X-ray diffraction measurements which directly probe the structural order parameter, show that annealing causes the ordering temperatures of both the phase transitions to increase, sharpen and converge. In the as-grown sample, our measurements show two distinct transitions corresponding to structural and magnetic ordering, which are separated in temperature by approximately 1 K. After 46 days of annealing, the two become concurrent in temperature. The X-ray measurements demonstrate that the structural phase transition is second-order like when the magnetic and structural phase transitions are separated in temperature, and first-order like when the magnetic and structural transition temperature coincides with the structural phase transition. This observation indicates that annealing causes the system to cross a hitherto undiscovered tricritical or multicritical point. In addition, X-ray diffraction measurements show that the c-axis lattice parameter increases with annealing times up to 30 days, and then saturates. Comparisons of the $BaFe_2As_2$ system to $SrFe_2As_2$ are made when possible

I. INTRODUCTION

The discovery of high-temperature superconductivity in the layered iron-pnictide materials[1] has generated great excitement within the strongly correlated electron community. While research into the pnictides is still ongoing, one of the central results has been the intimate connection between superconductivity, magnetism and the lattice structure. Thus to explain how superconductivity emerges in these materials, one must understand the interaction between these three degrees of freedom. To date superconductivity has been identified in several groups of pnictides which have related structures[1–4]. For all the structural classes, the parent compounds exhibit antiferromagnetic order at low temperatures. This magnetic ordering is either preceded or accompanied by a structural phase transition, where the crystal lattice changes from a high temperature tetragonal to a low temperature orthorhombic structure. Upon chemical substitution, the ordering temperatures of both transitions are suppressed and in some cases superconductivity is induced.

The archetypal class of pnictide superconductors are derive from parent compounds of the formula: MFe_2As_2 (M=Ca, Sr, Ba), and are known as the 122 compounds. For this structural class, superconductivity has been induced by substitution on all three atomic sites[2,5–9], or through the application of hydrostatic pressure[10,11]. There has already been a significant amount of research conducted into the nature of the structural and magnetic phase transitions in these compounds. For $CaFe_2As_2$

and $SrFe_2As_2$, the consensus is that the phase transitions are concurrent in temperature and can therefore be thought of as a single first-order magnetostructural transition[12–14]. The case of $BaFe_2As_2$ is more complex however; there have been reports of these phase transitions being both first[15] and second-order or, at least, nearly so[16]. Of particular interest is the research conducted by Rotundu *et al.*[17], where high resolution heat capacity, resistivity and X-ray diffraction measurements were taken on a $BaFe_2As_2$ single crystal that had been annealed in a low pressure Ar atmosphere. Results showed that anomalies observed in the resistivity and heat capacity were raised in temperature from 135.4 K to 140.2 K after 30 days of annealing. Measurements of the sample's residual resistivity ratio showed a consistent improvement with annealing time. This result was confirmed by a later work where $BaFe_2As_2$ single crystals were annealed in a BaAs powder[18]. In the work of Rotundu *et al.*[17], heat capacity measurements showed a peak in C/T consistent with a first-order transition. After 30 days of annealing, the peak raises and sharpens in temperature. To corroborate this finding, high resolution X-ray diffraction measurements of the structural phase transition were carried out for the 30 day annealed sample. The X-ray measurements showed that upon cooling, the orthorhombic distortion initially appeared as a continuous splitting of the tetragonal reflection. At a slightly lower temperature, the continuous splitting was interrupted by the abrupt appearance of a second set of orthorhombic reflections whose positions were nearly constant. As the sample was cooled further

the first set of reflections were rapidly suppressed; their positions continued to move outwards, but never merged with the second set of reflections.

This important result suggests that the structural phase transition in 30-day annealed $BaFe_2As_2$ begins as second-order, but evolves into a first-order transition upon lowering of the temperature. Rotundu *et al.*[17] speculated that the driving force behind this evolution is the formation of the antiferromagnetic order. This unusual structural phase transition was confirmed in an as-grown sample of $BaFe_2As_2$ by Kim *et. al.*[19], whom also conclusively showed that the discontinuous jump in the structural phase transition does indeed correspond to the appearance of antiferromagnetic order. Thus, although there is a subtle difference in the structural and antiferromagnetic ordering temperatures for these samples of $BaFe_2As_2$, the transitions are still strongly coupled to one another.

Even so, the changes in the structural and antiferromagnetic ordering temperatures and/or their separation with annealing, though subtle, might presumably change the coupling of the transitions. Thus annealing might represent a clean method to search for such changes.

Similar X-ray measurements of the structural order parameter in Co- and Rh-doped $BaFe_2As_2$ have been used to accurately track the divergence of the structural and antiferromagnetic ordering temperatures. For the Co-doped compound, a tricritical point wherein the two phase transitions split into separate second-order transitions was identified at a doping level of ≈ 0.22[19,20].

While it has already been shown that annealing has a substantial effect on the properties of $BaFe_2As_2$, there are several unanswered questions regarding how annealing effects this compound. For example, does annealing modify the structure or lattice of these materials? What changes (if any), does annealing have on the nature of the structural and magnetic phase transitions? What is the limiting behavior of extended annealing on the crystals and on their phase transitions?

In order to answer these questions, we have undertaken a number of X-ray diffraction and magnetic susceptibility measurements to study the changes in the structural and magnetic properties of $BaFe_2As_2$, as single crystal samples are annealed for various periods of up to 46 days. In addition, high resolution X-ray diffraction measurements of the structural phase transition in as-grown, 30 and 46 day annealed single crystal samples were also taken. Since neutron diffraction is unable to resolve the jump in the structural phase transition[16], these high resolution X-ray diffraction measurements offer a method to accurately determine the separation in ordering temperatures. A full description of these measurements is given in section II, while the experimental results are shown in section III. Finally this work is discussed and summarized in section IV.

II.   EXPERIMENTAL METHODS

Single crystal samples of $BaFe_2As_2$ were grown using the self-flux method[21]. In order to prevent the absorption of oxygen during the annealing process, crystal samples were wrapped in tantalum foil (a material that readily combines with oxygen) and sealed in a quartz tube with a low pressure Ar atmosphere[22]. After which the samples were annealed at 700°C for cumulative periods of 22, 30 and 46 days. X-ray diffraction measurements of the room temperature lattice parameters and magnetic susceptibility measurements of the phase transition(s) were taken on a single sample as-grown and after each annealing period.

The magnetic susceptibility measurements were taken with a Quantum Design Magnetic Property Measurement System (MPMS), in a magnetic field of $5\mu_0T$ parallel to the sample's a-b crystallographic plane. The susceptibility was recorded upon cooling though the phases transition at intervals of 0.25 K.

Room temperature X-ray diffraction measurements of the (004), (008) & (0012) reflections were taken using a X'Pert pro four-circle diffractometer, with a monochromated Cu-α_1 source.

High resolution X-ray diffraction measurements of the structural phase transition were taken at beamline 7-2, Stanford Synchrotron Radiation Laboratory, on a as-grown sample and after 30 and 46 days of annealing. The diffraction measurements were taken with an X-ray photon energy of 16 keV, in a vertical scattering geometry. Rocking curves of the (008) reflection in as-grown and after 30 days of annealing, gave a full width at half maximum (FWHM) of $\leq 0.1°$, indicating a good surface mosaic. Rocking curves of the same reflection after 46 days of annealing gave a FWHM of $\sim 0.25°$. In order to study the structural phase transition, high resolution reciprocal space scans along the [110] direction were used to measure the splitting of an (HHL) tetragonal reflection into the (H0L) and (0HL) orthorhombic reflections. For as-grown and 30 days annealed, the splitting of the $(3318)_T$ reflection was measured, while the splitting of the $(2216)_T$ reflection was measured in the 46 day annealed . These reciprocal space scans were taken as the temperature was decreased from 160 K to a base temperature of 80 K. Close to the structural phase transition, measurements were taken at temperature steps of 0.1 K. A rest period of at least 4 minutes preceded each scan, this ensured that the measured temperature fluctuations were much less than 0.1 K.

III.   EXPERIMENTAL RESULTS

The process of annealing causes the crystals to dull. To determine if this effect is indicative of a change in chemical composition, wavelength dispersive X-ray spectroscopy measurements were taken after each annealing period. Results showed that annealing produced no

change in the Ba:Fe:As elemental ratio and did not lead to the inclusion of Tantalum.

A. Annealing induced changes in the magnetic susceptibility.

In order to examine the effects of annealing on the magnetic properties of $BaFe_2As_2$, magnetic susceptibility measurements were taken on a single crystal sample as-grown and after each annealing period. Figure 1 (a) shows these measurements across the phase transition(s). The results have been normalized to allow for an easy comparison. The figure shows a step in the magnetic susceptibility that is indicative of a phase transition(s). Annealing raises the temperature of the phase transition(s) from 135.3K in the as-grown sample to 139.8K in the 46 day annealed sample. The transition temperature(s) for the 46 day annealed sample is slightly lower than the value of 140.2 K that was previously reported in a 30 day annealed sample[17]. However, the important point is that post growth annealing raises the temperature of the phase transition(s) in $BaFe_2As_2$.

To further investigate the effects of annealing on the nature of the phase transition(s), we have plotted $\partial(\chi T)/\partial(T)$ in figure 1 (b). $\partial(\chi T)/\partial(T)$ it is known to mimic the heat capacity of both the magnetic and structural phase transitions in the 122 compounds[20,23]. Thus we are able to make an approximate comparison to previous heat capacity measurements[17], however the establishment of a precise quantitative comparison between these two sets of measurements is beyond the purpose of this study. Like the previous heat capacity measurements, figure 1 (b) shows that annealing for long periods (≥ 22 days) causes the peak in $\partial(\chi T)/\partial(T)$ to sharpen.

Similar magnetic susceptibility measurements taken on $Ba(Fe_{1-x}Co_x)_2As_2$, show that the main peak in $\partial(\chi T)/\partial(T)$ arises from the magnetic phase transition, while a shoulder on the high temperature side of the transition represents the structural phase transition.[20,23] Our susceptibility data appear as a single peak at all annealing times, indicating the absence of a distinguishable shoulder feature due to the structural transition. The sharpening of the transition may be due to the increased homogeneity of the sample after annealing. In addition, if the structural transition does contribute to the weight of the susceptibility anomaly as, is the case in lightly cobalt-substituted samples[20,23], then the sharpening of the anomaly is not inconsistent with the results of our X-ray diffraction measurements and the previous heat capacity study[17], namely that the separation between the magnetic and structural transition temperatures decreases with annealing until they converge in the 46-day annealed sample.
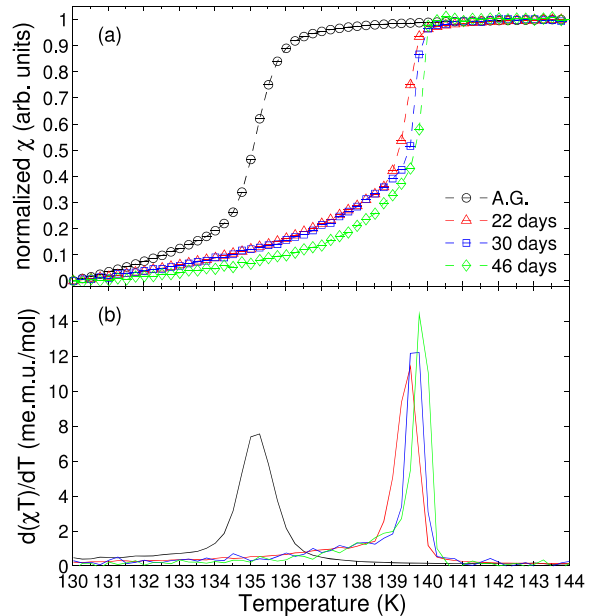
FIG. 1. (a): χ vs T of the phase transitions for a $BaFe_2As_2$ sample, as-grown (A.G.) and after 22, 30 and 46 days of annealing. The data has been normalized to be 0 at 130 K and 1 at 145 K. (b): $\partial(\chi T)/\partial(T)$ vs T.

B. Annealing induced changes in the c-axis lattice parameter.

An investigation into the variations of the lattice parameters might provide useful information into how the process of annealing is modifying the physical properties of this material and serve as a benchmark to compare sample quality across studies. To this end, room temperature X-ray diffraction measurements of the out-of-plane reflections: (004), (008) & (0012), were taken in the same single crystal, as-grown and after each annealing period. Figure 2 shows longitudinal scans across the (008) reflection for the different annealing periods. The reflections have been fitted with a Gaussian curve using a non-linear least squares analysis. The figure shows that annealing has two effects. First, it causes the reflection's intensity to decrease; this may be linked to the crystal becoming duller and/or an increase in crystal's mosaic spread with annealing (see section II). No change was seen in the width (in 2θ) of these reflections with annealing, although these measurements are almost certainly resolution limited by the diffractometer. Second, annealing periods of ≤ 30 days cause the 2θ angle of reflection to increase, revealing that the c-axis lattice parameter contracts. Comparing annealing periods of 30 & 46 days, the reflection's position remains unchanged. These observations also hold true for the (004) & (0012) reflections. This result is summarized in table I, which shows the mean c-axis lattice parameter as determined from the positions of the three out-of-plane reflections.
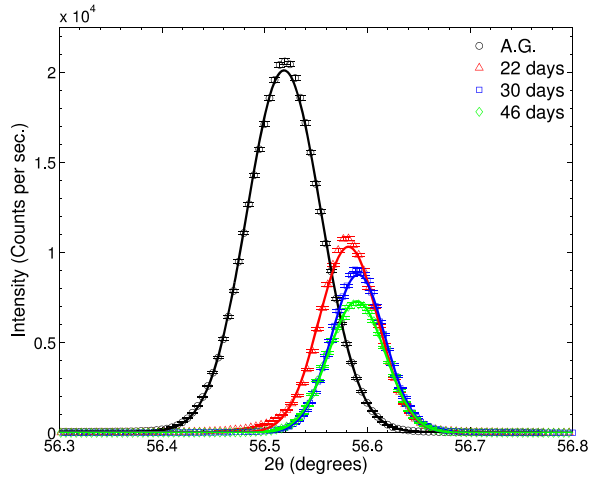
FIG. 2. Longitudinal scans of the BaFe$_2$As$_2$ (008) reflection for as-grown (A.G.) and after 22, 30 and 46 days of annealing. The reflections are fitted with a Gaussian profile.

Annealing time (days)	c-axis lattice parameter (Å)
0	$13.0168\pm9\times10^{-4}$
22	$13.0039\pm1.9\times10^{-3}$
30	$13.0024\pm1.3\times10^{-3}$
46	$13.0025\pm1.9\times10^{-3}$

TABLE I. The mean c-axis lattice parameter and errors for the various annealing periods. These values were determined from fitting the (004), (008) & (0012) reflections with a Gaussian curve using a non-linear least squares analysis, for example see figure 2.

C. Annealing induced changes as seen with X-ray measurements of the structural phase transition.

The final part of this section will focus on any annealing induced changes in the coupling of the structure to the magnetism. In order to study this, we have performed high resolution synchrotron X-ray diffraction measurements of the tetragonal to orthorhombic structural phase transition in as-grown, 30 & 46 day annealed samples. Since the second to first-order jump in the structural phase transition is due to the on-set of antiferromagnetic order[19], these X-ray diffraction measurements should provide information on subtle changes in the nature, temperature and coupling of the structural and magnetic phase transition. Results from these measurements are summarized in table II.

Each of the as-grown and 30 day annealed samples exhibit the now familiar structural phase transition: upon cooling the tetragonal reflection broadens and then splits. At a slightly lower temperature, a second set of (outer) reflections suddenly appears. The positions of these outer reflections are only weakly temperature dependent, although their intensity increases with decreasing temperature. Upon a further decrease in temperature the first

Annealing time (days)	T_S (K)	T_N (K)	T_S-T_N (K)	ΔT_S (K)
0	134.6 (135.2)	133.8	0.8 (1.5)	1.8
30	138.8 (139.5)	138.5	0.3 (1)	1.5
46	138.7	138.7	0	0.8

TABLE II. Characteristic temperatures of the structural phase transition in as-grown, 30 & 46 day annealed BaFe$_2$As$_2$. Here T_S is the temperature where the continuous splitting (broadening) of the tetragonal reflection is first detected. T_N is the temperature where this continuous splitting of tetragonal reflection is interrupted by the appearance of the second set of orthorhombic reflections. Finally, ΔT_S is the difference in temperature between T_N and the disappearance of the inner set peak(s).

set of reflections is rapidly suppressed and their peak positions continue to move outwards, however they never merge with the second set of reflections. An example of this phase transition in the 30 day annealed sample is given in figure 3. The figure shows the $(3318)_T$ tetragonal reflection splitting into the $(6018)_O$ and $(0618)_O$ orthorhombic reflections.

By contrast the structural phase transition in the 46-day annealed sample appears to be purely first-order to at least 0.1 K. This result is given in figure 4, which shows the evolution of the $(2216)_T$ tetragonal reflection into the $(4016)_O$ and $(0416)_O$ orthorhombic reflections upon cooling: for this sample, the continuous splitting of the tetragonal reflection was not observed, instead a set of first-order orthorhombic reflections appear abruptly at 138.7 K (for example see figure 4 (b)). Upon a further decrease in temperature, the intensity of these reflections increase but their position remains approximately constant. Simultaneously, the intensity of the tetragonal reflection decreased, but no significant change in position or width of this reflection was detected.

To emphasize these differences we have plotted the structural order parameter for all sets of measurements, $\delta = (a_O - b_O)/(a_O + b_O)$ close to the phase transition in figure 5(a). The lattice constants a_O and b_O were determined through fitting the reflections with a Lorentzian squared profile using a non-linear least squares analysis. Figure 5(b) shows the FWHM of fits to the tetragonal reflection for temperatures just above structural phase transition in the as-grown and 30 day annealed sample.

For comparison, the structural order parameter of SrFe$_2$As$_2$ is plotted in figure 6. These measurements were taken under the same experimental conditions as for BaFe$_2$As$_2$. The figure shows that the structural phase transition is first-order in SrFe$_2$As$_2$ and similar in nature to the 46 day annealed BaFe$_2$As$_2$.

Since a previous study[19] has shown that the jump in the structural order parameter corresponds to the onset of antiferromagnetic order, the difference between the temperature of the initial splitting (broadening) of the tetragonal reflection and the appearance of the second set of orthorhombic reflections can be readily interpreted as
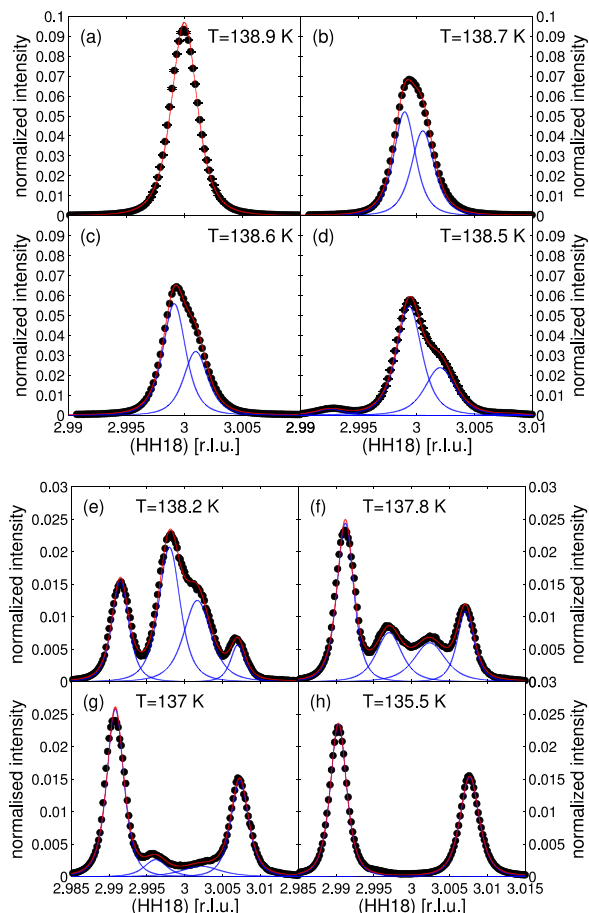
28

FIG. 3. Examples of reciprocal lattice scans across the $(3318)_T$ reflection in 30 day annealed BaFe$_2$As$_2$. All peaks are fitted with a Lorentzian squared profile.

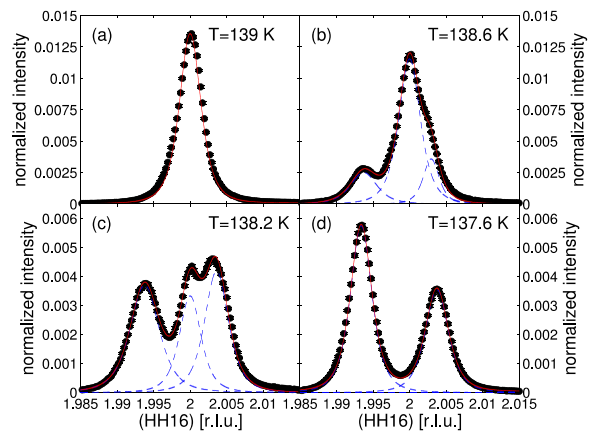

FIG. 4. Examples of reciprocal lattice scans across the $(2216)_T$ reflection in the 46 day annealed BaFe$_2$As$_2$ crystal. All peaks are fitted with a Lorentzian squared profile.

ple. The main point however, is that like the magnetic susceptibility measurements, these X-ray measurements show that annealing increases the ordering temperatures of the phase transitions. Thus the changes in the transition temperatures with annealing observed in our study and the character of the structural order parameter in the as-grown and 30-day annealed samples are consistent with previous studies[17,19]

IV. DISCUSSION AND CONCLUSION

We have shown that annealing of BaFe$_2$As$_2$ causes the structural and magnetic phase transitions to increase and converge in temperature. This culminates in the 46 day annealed sample where the two phase transitions are coincident in temperature to at least 0.1 K.

The present study also confirms that the two phase transitions are separated in temperature in as-grown samples, which did not involve a de-canting step in the growth as did the study of Kim et[19]. Thus this property is likely to be intrinsic to BaFe$_2$As$_2$.

The onset of structural order evidenced by a continuous splitting of the tetragonal reflection has been suggested to correlate with occurrence of a nematically ordered electronic state[24]. Since the continuous splitting is seemingly absent in the 46-day annealed sample, measurements of the electronic anisotropy on samples with this attribute may prove to be a fertile ground in studying the interplay of the structural transition and electron nematic order.

An important question to address is: what is the microscopic effect of annealing which gives rise to the changes in the structural and magnetic phase transitions of BaFe$_2$As$_2$?

In addition, for a first-order phase transformation, the suppression of the phase transition temperature is a hallmark of quenched (non-uniform) disorder: the transition

the difference between the structural and antiferromagnetic phase transition temperatures, this is shown the third column in table II. Initially the difference between ordering temperatures is 0.7 (1.4) K, after 30 days of annealing the difference in ordering temperatures is reduced to 0.3 (1) K. Because the structural phase transition for 46 day annealed BaFe$_2$As$_2$ is completely first-order, we believe that annealing for this length of time cause the antiferromagnetic and structural ordering temperatures to converge to within at least 0.1 K. It is also worth noting that the temperature range of co-existence between the two sets of reflections, shown in the fourth column of table II, decreases with annealing time. While the inner and outer peaks coexist in the as-grown sample over a range of 1.8K, in the 46-day annealed sample the inner peak coexists with the outer peaks over 0.8K.

At this point it should be noted that the ordering temperatures given in table II are slightly lower than the ordering temperatures indicated by the magnetic susceptibility (figure 1). Likely explanations for this inconsistency include slight differences in the calibrations of the respective thermometers and their distance to the sam-
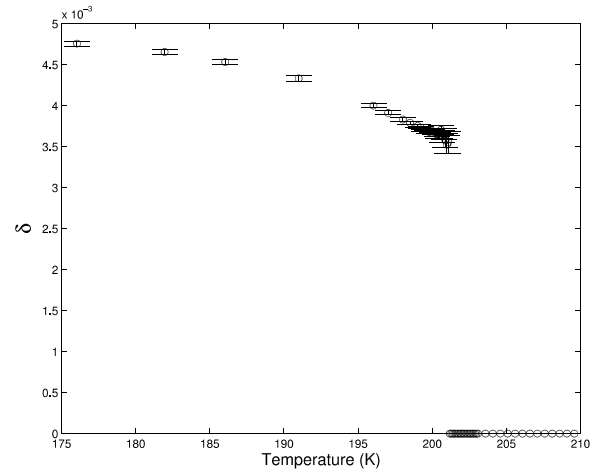
FIG. 6. The structural order parameter of as-grown $SrFe_2As_2$, measured under the same experimental conditions as the order parameters shown in figure 5(a).

FIG. 5. (a) The $BaFe_2As_2$ structural order parameter: $\delta=(a_O - b_O)/(a_O + b_O)$ vs T for as-grown and after 30 & 46 days of annealing. (b) The FWHM of the $(3318)_T$ reflection in the as-grown and 30 day annealed samples. Results show a broadening of this reflection for temperatures just above the structural phase transition.

temperature of a first-order transition is suppressed due to the finite energy of forming domain walls [Imry and Wortis]. Thus the rise of both transition temperatures should be taken as evidence that, at the least, the disorder is homogenized in or annealed samples. Even slight amounts of disorder can cause the phase transition to round, and lower the latent heat of the transition.

The simplest explanation is that annealing modifies the concentration of a certain defect species: such as dislocations, vacancies, or interstitials. In fact the mechanism of how chemical substitution effects the magnetic and structural transitions of $BaFe_2As_2$ is open to debate, i.e. are these changes in these properties due to modifications in the carrier concentration, impurity scattering or a combination of both[25]?

Therefore, the increase in T_S and T_N, as well as the decrease in T_S-T_N with annealing, could be explained by this.

While annealing would likely decrease the concentration of vacancies or dislocations, another possibility is that an interstitial species is introduced to the system

by repeated annealing and exposure to the ambient environment during the course of the X-ray and susceptibility measurements; for instance, exposure of thin-film $SrFe_2As_2$ samples to ambient pressure water vapor is known to effect the c-axis lattice parameter and FWHM in a manner consistent with our observations; however, such vapor was also found to induce superconductivity[26] which is inconsistent with our measurements.

Although we cannot specify the types of defects present in our samples, we suggest that the elimination of defects with annealing may correlate with the trends described in this paper, as well as the increase in the RRR[17].

Another possible mechanism which might presumably give rise to the evolution of T_S and T_N involves reorientation of the excess FeAs flux within the crystal; for $Ca(Fe_{1-x}Co_x)_2As_2$[27,28] it was suggested that nanoscale precipitates with compositions close to that of the flux effectively induce hydrostatic pressure on the quenched crystals. The solubility of the flux, and hence the effective pressure induced by the precipitates are then proportional to the temperature from which the crystals are quenched. The authors of these works suggested a similar process may explain the changes in T_N and T_S with annealing in $Ba(Fe_{1-x}Co_x)_2As_2$[17,29] and speculated equivalent effects for $SrFe_2As_2$[27]. If this model were applicable, we would expect the annealing process to reduce the effective pressure on the crystals, since the annealing temperature ($700°C$) is lower than that of the final reaction temperature of the as-grown crystals ($900°C$). However, opposite to what is expected for a reduction of pressure within the crystal[30], annealing leads to a reduction in the c-axis lattice parameter. And, although the physical properties of $SrFe_2As_2$ are as sensitive to hydrostatic pressure as those of $BaFe_2As_2$[11,31], T_S and T_N are coincident as evidenced by our measurements of its structural phase transition. Thus this mechanism does not suffice to explain our results.

One of the most surprising results of our study is that after a very long annealing time the structural and magnetic transitions converge and the structural transition becomes first order. It has already been demonstrated that the magnetic transition is first order in the parent compound, but crosses over from first to second order at a tricritical point as a function of cobalt substitution[20]. Here we have the unusual result that the structural transition is first order for the long-time annealed sample but is second order in either as-grown samples or with short annealing times. There are at least two scenarios for the resultant phase diagram. One is that the structural phase transition line also has a tricritical point, albeit at extremely low defect/dopant densities. The second is that the phase diagram has a special kind of multicritical point when the structural and magnetic transitions coincide but the structural transition becomes second order as soon as the two transition temperatures differ. Theoretical guidance on this subject would be most helpful. High precision measurements on samples with very low dopant concentrations and long annealing times may also be illuminating.

In conclusion, we have studied the effects of post growth annealing on the structural and magnetic properties of the pnictide $BaFe_2As_2$. We show that annealing causes the ordering temperatures of both the structural and magnetic phase transitions to increase. Our results show that annealing causes the two ordering temperatures to increase and converge, culminating in the 46 day annealed sample where they are coincident to less than 0.1 K. We argue that the hypothesis of annealing-induced changes in the defect/dopant densities, provides the best explanation of the experimental results presented in this paper and elsewhere[17].

Finally, the phase diagram in the immediate vicinity of the pure system's multicritical point requires further investigation, both experimental and theoretical.

* forrest@esrf.fr
[1] Y. Kamihara, T. Watanabe, M. Hirano, and H. Hosono, J. Am. Chem. Soc. **130**, 3296 (2008).
[2] M. Rotter, M. Tegel, and D. Johrendt, Phys. Rev. Lett. **101**, 107006 (2008).
[3] J. Tapp, Z. Tang, B. Lv, K. Sasmal, B. Lorenz, P. Chu, and A. Guloy, Phys. Rev. B **78**, 060505 (2008).
[4] X. Zhu, F. Han, G. Mu, P. Cheng, B. Shen, B. Zeng, and H.-H. Wen, Phys. Rev. B **79**, 220512 (2009).
[5] A. Sefat, R. Jin, M. McGuire, B. Sales, D. Singh, and D. Mandrus, Phys. Rev. Lett. **101**, 117004 (2008).
[6] A. Leithe-Jasper, W. Schnelle, C. Geibel, and H. Rosner, Phys. Rev. Lett. **101**, 207004 (2008).
[7] L. Li, Y. Luo, Q. Wang, H. Chen, Z. Ren, Q. Tao, Y. Li, X. Lin, M. He, Z. Zhu, G. Cao, and Z. Xu, New Journal of Physics **11**, 025008 (2009).
[8] K. Sasmal, B. Lv, B. Lorenz, A. Guloy, F. Chen, Y.-Y. Xue, and C.-W. Chu, Phys. Rev. Lett. **101**, 107007 (2008).
[9] S. Jiang, H. Xing, G. Xuan, C. Wang, Z. Ren, C. Feng, J. Dai, Z. Xu, and G. Cao, J. Phys.: Condens. Matter. **21**, 382203 (2009).
[10] M. Torikachvili, S. Bud'ko, N. Ni, and P. Canfield, Phys. Rev. Lett. **101**, 057006 (2008).
[11] P. Alireza, Y. Ko, J. Gillett, C. Petrone, J. Cole, G. Lonzarich, and S. Sebastian, J. Phys.: Condens. Matter. **21**, 012208 (2009).
[12] N. Ni, S. Nandi, A. Kreyssig, A. I. Goldman, E. D. Mun, S. L. Bud'ko, and P. C. Canfield, Phys. Rev. B **78**, 014523 (2008).
[13] A. I. Goldman, D. N. Argyriou, B. Ouladdiaf, T. Chatterji, A. Kreyssig, S. Nandi, N. Ni, S. L. Bud'ko, P. C. Canfield, and R. J. McQueeney, Phys. Rev. B **78**, 100506 (2008).
[14] H. Li, W. Tian, J. Zarestky, A. Kreyssig, N. Ni, S. Bud'ko, P. Canfield, A. Goldman, R. McQueeney, and D. Vaknin, Phys. Rev. B **80**, 054407 (2009).
[15] M. Kofu, Y. Qiu, W. Bao, S.-H. Lee, S. Chang, T. Wu, G. Wu, and X. Chen, New Journal of Physics **11**, 055001 (2009).
[16] S. D. Wilson, Z. Yamani, C. R. Rotundu, B. Freelon, E. Bourret-Courchesne, and R. J. Birgeneau, Phys. Rev. B **79**, 184519 (2009).
[17] C. R. Rotundu, B. Freelon, T. R. Forrest, S. D. Wilson, P. N. Valdivia, G. Pinuellas, A. Kim, J.-W. Kim, Z. Islam, E. Bourret-Courchesne, N. E. Phillips, and R. J. Birgeneau, Phys. Rev. B **82**, 144525 (2010).
[18] S. Ishida, T. Liang, M. Nakajima, K. Kihou, C. H. Lee, A. Iyo, H. Eisaki, T. Kakeshita, T. Kida, M. Hagiwara, Y. Tomioka, T. Ito, and S. Uchida, Phys. Rev. B **84**, 184514 (2011).
[19] M. G. Kim, R. M. Fernandes, A. Kreyssig, J. W. Kim, A. Thaler, S. L. Bud'ko, P. C. Canfield, R. J. McQueeney, J. Schmalian, and A. I. Goldman, Phys. Rev. B **83**, 134522 (2011).
[20] C. R. Rotundu and R. J. Birgeneau, Phys. Rev. B **84**, 092501 (2011).
[21] X. F. Wang, T. Wu, G. Wu, H. Chen, Y. L. Xie, J. J. Ying, Y. J. Yan, R. H. Liu, and X. H. Chen, Phys. Rev. Lett. **102**, 117005 (2009).
[22] The quartz tubes were filled with Ar gas and pumped out using a combined roughing & torus pump set-up. The pumping was continued until a pressure level of less than 1×10^{-5} was displayed, after which the tube was immediately sealed.
[23] J.-H. Chu, J. G. Analytis, C. Kucharczyk, and I. R. Fisher, Phys. Rev. B **79**, 014506 (2009).
[24] J.-H. Chu, J. G. Analytis, K. De Greve, P. L. McMahon,

Z. Islam, Y. Yamamoto, and I. R. Fisher, Science **329**, 824 (2010).

[25] T. Berlijn, C.-H. Lin, W. Garber, and W. Ku, Phys. Rev. Lett. **108**, 207003 (2012).

[26] H. Hiramatsu, T. Katase, T. Kamiya, M. Hirano, and H. Hosono, Phys. Rev. B **80**, 052501 (2009).

[27] S. Ran, S. L. Bud'ko, D. K. Pratt, A. Kreyssig, M. G. Kim, M. J. Kramer, D. H. Ryan, W. N. Rowan-Weetaluktuk, Y. Furukawa, B. Roy, A. I. Goldman, and P. C. Canfield, Phys. Rev. B **83**, 144517 (2011).

[28] S. Ran, S. L. Bud'ko, W. E. Straszheim, J. Soh, M. G. Kim, A. Kreyssig, A. I. Goldman, and P. C. Canfield, Phys. Rev. B **85**, 224528 (2012).

[29] K. Gofryk, A. B. Vorontsov, I. Vekhter, A. S. Sefat, T. Imai, E. D. Bauer, J. D. Thompson, and F. Ronning, Phys. Rev. B **83**, 064513 (2011).

[30] N. Eguchi, M. Kodama, F. Ishikawa, A. Nakayama, Y. Ohmura, A. andYamada, and S. Nakano, J. Phys.: Conf. Ser. **400**, 022017 (2012).

[31] K. Matsubayashi, N. Katayama, K. Ohgushi, A. Yamada, K. Munakata, T. Matsumoto, and Y. Uwatoko, J. Phys. Soc. Jpn **78**, 073706 (2009).

3.3 Outlook

It is still not entirely clear if the structural tricritical point occurs as a function of the defect density, or of the dopant density, in which case it might possibly also depend on the dopant type. These two scenarios might produce different physical behaviors. It is known that in the electron-substituted arsenide compounds, the structural transition and the magnetic transition split in temperature as a function of substitution, while in the hole-substituted compounds, they remain concomitant. Therefore, if the effect of annealing is to remove slight electron dopants in the as-grown samples, which causes us to cross the tricritical point, then whether the structural tricritical point occurs at all in the hole-doped systems remains an open question. On the other hand, if the structural tricritical point is controlled by the defect density, one may expect a structural tricritical point to occur at a similarly low value of the defect density when substituting hole dopants, which would imply that an initially continuous structural transition could be observed for these substituents as well.

As discussed in the experimental section, at a tricritical point, three distinguishable phases become indistinguishable. Thus, when the structural transition is separated from the magnetic transition and is second-order, fields which couple to the structural order do not produce distinguishable phases, at least not in the structural phase immediately below the transition. When the structural transition is first-order and occurs together with the magnetic transition, fields acting on the structural order will also act on the magnetic order; and thus, if a field acting on the structure could be produced which couples differently to the two antiferromagnetic sublattices, we might expect to observe a first-order phase boundary between distinguishable structural and magnetic states.

Chapter 4

Two Spatially Separated Phases in $Rb_{0.8}Fe_{1.5}S_2$

4.1 Introduction

At the time of writing this dissertation, Dr. Meng Wang is a postdoc in our group. During his postdoc I have been fortunate to be able to collaborate with him in studying the alkalai metal chalcogenides. The following paper helps demonstrate a few of the most important features of these systems which distinguish them from the iron pnictides: namely, large moment magnetism, a magnetic ordering wavevector at a different position in reciprocal space than that of the Fermi surface nesting observed by ARPES measurements, high temperature vacancy orders, and local structural distortions near the vacancies. This work furthers our understanding of these phases and their interaction with one another: diffraction measurements reveal that the two phases which are observed in these samples exchange chemical species. Related to this, the paper also describes the chemical conditions necessary to obtain superconducting samples. Furthermore, the large moment size observed, and the fact that the Neel temperature of the stripe phase is very close to that found for the equivalent phase in the K-Fe-Se system each offer support for a local moment origin of the magnetism.

This paper was accepted for publication as: Phys. Rev. B 90, 125418, 2014.

4.2 Paper

Two spatially separated phases in semiconducting Rb$_{0.8}$Fe$_{1.5}$S$_2$

Meng Wang,[1, *] Wei Tian,[2] P. Valdivia,[1] Songxue Chi,[2] E. Bourret-Courchesne,[3] Pengcheng Dai,[4, 5] and R. J. Birgeneau[1, 3, 6]

[1]*Department of Physics, University of California, Berkeley, California 94720, USA*
[2]*Quantum Condensed Matter Division, Oak Ridge National Laboratory, Oak Ridge, Tennessee 37831-6393, USA*
[3]*Materials Science Division, Lawrence Berkeley National Laboratory, Berkeley, California 94720, USA*
[4]*Department of Physics and Astronomy, Rice University, Houston, Texas 77005, USA*
[5]*Institute of Physics, Chinese Academy of Sciences, P. O. Box 603, Beijing 100190, China*
[6]*Department of Materials Science and Engineering,*
University of California, Berkeley, California 94720, USA

We report neutron scattering and transport measurements on semiconducting Rb$_{0.8}$Fe$_{1.5}$S$_2$, a compound isostructural and isoelectronic to the well-studied $A_{0.8}$Fe$_y$Se$_2$(A = K, Rb, Cs, Tl/K) superconducting systems. Both resistivity and dc susceptibility measurements reveal a magnetic phase transition at $T = 275$ K. Neutron diffraction studies show that the 275 K transition originates from a phase with rhombic iron vacancy order which exhibits an in-plane stripe antiferromagnetic ordering below 275 K. In addition, the stripe antiferromagnetic phase interdigitates mesoscopically with an ubiquitous phase with $\sqrt{5} \times \sqrt{5}$ iron vacancy order. This phase has a magnetic transition at $T_N = 425$ K and an iron vacancy order-disorder transition at $T_S = 600$ K. These two different structural phases are closely similar to those observed in the isomorphous Se materials. Based on the close similarities of the in-plane antiferromagnetic structures, moments sizes, and ordering temperatures in semiconducting Rb$_{0.8}$Fe$_{1.5}$S$_2$ and K$_{0.81}$Fe$_{1.58}$Se$_2$, we argue that the in-plane antiferromagnetic order arises from strong coupling between local moments. Superconductivity, previously observed in the $A_{0.8}$Fe$_y$Se$_{2-z}$S$_z$ system, is absent in Rb$_{0.8}$Fe$_{1.5}$S$_2$, which has a semiconducting ground state. The implied relationship between stripe and block antiferromagnetism and superconductivity in these materials as well as a strategy for further investigation is discussed in this paper.

PACS numbers: 74.25.Ha, 74.70.-b, 78.70.Nx

I. INTRODUCTION

The $A_{0.8}$Fe$_{1.6 \pm \delta}$Se$_2$ (A =K, Rb, Cs, Tl/K) materials, the so-called '245' systems were discovered at the end of 2010, and have since generated a great deal of interest, in large part because of their unique properties: iron vacancy order, block antiferromagnetism (AF) with large $3.3\mu_B$ moments aligned along the c axis, and the existence of superconductivity for appropriate chemical compositions[1–6]. In the Fe pnictide systems, the parent compounds of the superconductors exhibit a collinear antiferromagnetic structure with small ordered moments, typically less than $1\mu_B$[7–10]. Superconductivity arises upon electron or hole doping of the parent compounds, which concomitantly suppresses the AF order. Spin fluctuations associated with the AF order, which exist throughout the superconducting (SC) dome, are thought to play a crucial role in the mechanism of superconductivity[11–13]. In the standard interpretation, nesting between the hole and electron Fermi surfaces gives rise to spin-density-wave (SDW) order. In addition, the ubiquitous occurrence of a neutron 'spin-resonance' at the SDW wave vector in superconducting iron pnictide compounds has been suggested to correlate with "s±" pairing symmetry[14–16].

A spin resonance mode was also found in the 245 system, but at a wave vector different from those of both the block and stripe AF orders[17,18]. Importantly, unlike the Fe pnictides, a weak electron-like Fermi pocket and hole-like bands below the Fermi surface are found in place of hole Fermi surfaces around the Γ point in the $A_{0.8}$Fe$_{1.6}$Se$_2$ system[19–21]. The occurrence of superconductivity with T_c up to 32 K in the '245' system in the absence of electron-hole nesting presents a significant challenge to current theories of these phenomena[22].

There is extensive empirical evidence that the SC phase occurs mesoscopically separated from the block AF insulator[23–29]. The block AF phase exists throughout the two dimensional phase diagrams of A_xFe$_y$Se$_2$ over wide variations in the alkali metal ($0.77 \leq x \leq 0.98$) and iron contents ($1.48 \leq y \leq 1.65$), with little change of T_N[30]. We emphasize that (x, y) are for the sample as a whole, not the two separate constituent phases in most studies. The reports focused on the composition of the superconducting phase remain conflicting[27,31–33]. Thus, the nature of the real superconducting phase and its parent compound are still under debate[25–27,31–34]. Both theory and photoemission experiment proposed an insulating or semiconducting phase as a candidate for the parent compound of the superconducting phase in (K, Tl)$_x$Fe$_y$Se$_2$[25,35]. Importantly, the same stripe AF structure with in-plane ordered moments that occurs in the parent compounds of pnictide superconductors was observed in semiconducting K$_{0.81}$Fe$_{1.58}$Se$_2$ by neutron diffraction[33]. If the stripe phase with in-plane AF order is, in fact, the parent compound of the superconducting phase in the '245' system, then the SC in this system may have the same underlying mechanism as that in the other iron based superconductors, in spite of the absence

of electron-hole nesting and different neutron spin resonance wave vectors[14–21]. Therefore, determining the origin of the in-plane AF order in the semiconducting phase and its relationship with superconductivity is crucial to understanding the mechanism of superconductivity in the $A_x\text{Fe}_y\text{Se}_2$ system.

The low-temperature electrical resistivity of the '245' system can be changed from insulating to semiconducting or superconducting by controlling the iron content as in $A_{0.8}\text{Fe}_y\text{Se}_2$, generally in concert with the alkali concentration A, or by substitution of sulfur on the selenium sites as in $A_{0.8}\text{Fe}_y\text{Se}_{2-z}\text{S}_z$[33,36–40]. In studies to-date, changing the iron content of the pure Se two-phase material results in the sudden disappearance of the superconductivity, while sulfur substitution for selenium appears to suppress superconductivity gradually, resulting in a semiconducting ground state[39]. Accordingly, semiconducting $A_{0.8}\text{Fe}_y\text{S}_2$ may also be viewed as the parent compound of the $A_{0.8}\text{Fe}_y\text{Se}_{2-z}\text{S}_z$ superconductors, although the magnetic phase diagram has not yet been determined for high sulfur substitution. Both high temperature transport and Raman scattering measurements indicate that the block AF phase also exists in the $A_x\text{Fe}_y\text{S}_2$ system[41,42]. Thus, it is important to investigate whether or not the in-plane AF order occurs in $A_{0.8}\text{Fe}_y\text{S}_2$ and, if so, to determine its relationships with superconductivity in the S-substituted $A_{0.8}\text{Fe}_y\text{Se}_{2-z}\text{S}_z$.

In this paper, we present transport and elastic neutron scattering measurements on single crystals of semiconducting $\text{Rb}_{0.8}\text{Fe}_{1.5}\text{S}_2$. Two magnetic phases are found in this material with the next nearest (NN) Fe neighbor bond distances at 180 K 3.765 Å and 3.889 Å for the two phases respectively. The first phase, the '245' phase, which has the more compact in-plane lattice constants, has the $\sqrt{5}\times\sqrt{5}$ iron vacancy order and block AF order as in the $A_{0.8}\text{Fe}_{1.6\pm\delta}\text{Se}_2$ system[30]. The Néel temperature of the block AF order is 425 K; this is reduced significantly compared with ∼560 K in $A_{0.8}\text{Fe}_y\text{Se}_2$, and is also well separated from the $\sqrt{5}\times\sqrt{5}$ iron-vacancy-ordering temperature of 600 K in $\text{Rb}_{0.8}\text{Fe}_{1.5}\text{S}_2$[5]. Schematics of the three-dimensional structure together with that of the iron plane with ordered moments and iron vacancies are shown in Fig. 1 (a) and 1 (b). The second phase has rhombic iron vacancy order with in-plane stripe AF order below 275 K [Fig. 1 (c) and 1 (d)][43]. We named it the "234" phase (this assumes an ideal stoichiometry $\text{RbFe}_{1.5}\text{S}_2$) in spite of the possible deviation of Rb in the discussion below. The estimated in-plane magnetic moment size of $(2.8\pm0.5)\mu_B$ and the Néel temperature of 275 K for the stripe AF order in semiconducting $\text{Rb}_{0.8}\text{Fe}_{1.5}\text{S}_2$ are surprisingly close to the 2.88 μ_B moments and $T_N = 280$ K of the stripe AF order in semiconducting $\text{K}_{0.81}\text{Fe}_{1.58}\text{Se}_2$[33]. These results suggest that strong coupling of local moments plays the dominant role in the formation of in-plane AF order in semiconducting $A_{0.8}\text{Fe}_y X_2$ ($X =$ Se, S).
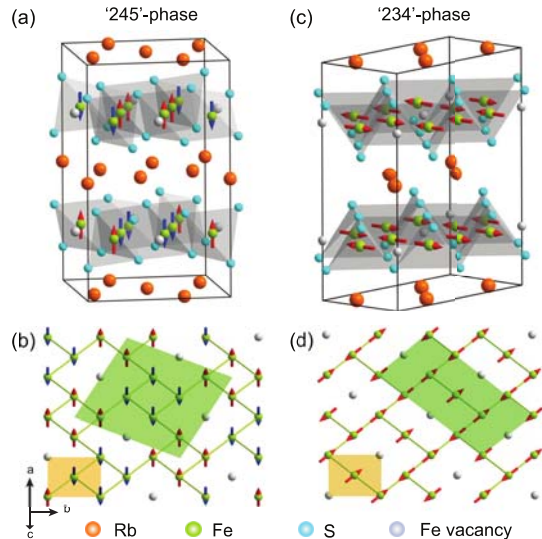
FIG. 1: (Color online). (a) Three-dimensional structure of the block AF phase in $\text{Rb}_{0.8}\text{Fe}_{1.5}\text{S}_2$. (b) The Fe plane of block AF phase with $\sqrt{5}\times\sqrt{5}$ iron order, where a magnetic unit cell with lattice parameter $a_s = \sqrt{5}\times 3.765$ Å has been marked as green. The tetragonal lattice cell used throughout this paper is shaded light orange. The red and blue arrows represent the out-of-plane spin directions up and down. The orange, lime, turquoise and light gray balls are Rb, Fe, and S atoms and Fe vacancies, respectively. (c) A three-dimensional magnetic unit cell of the in-plane AF order and (d) Fe-plane with the rhombic iron vacancy order. A magnetic unit cell is shaded green. The diagonal Fe bonds are 3.889 Å at 180 K.

II. EXPERIMENTAL DETAILS

Our experiments were carried out on the HB-1A triple-axis spectrometer and HB-2C wide-angle neutron diffractometer (WAND) at the High-Flux Isotope Reactor, Oak Ridge National laboratory. The triple-axis experiment employed two pyrolytic graphite (PG) filters before the sample to reduce $\lambda/2$ contamination and horizontal collimation $40'$-$40'$-S-$40'$-$80'$ with a fixed incident beam energy of $E_i = 14.64$ meV. A single piece of crystal weighing 220 mg with a mosaic of 1.5° was loaded into a closed cycle refrigerator (CCR) which covers the temperature range from 30 K to 750 K. The sample was aligned in the $[H, H, L]$ zone and the $[H, 3H, L]$ zone in tetragonal notation with lattice parameters $a = b = 3.889$ Å, $c = 13.889$ Å for the '234' phase and $a = b = 3.765$ Å, $c = 13.889$ Å for the '245' phase optimized at 180 K. The momentum transfer (q_x, q_y, q_z) is defined as $(2\pi H/a, 2\pi K/b, 2\pi L/c)$ in Å^{-1}. (H, K, L) are the Miller indices in reciprocal lattice units (r.l.u). We labeled the wave vectors as $Q = [H, K, L]$ r.l.u throughout this paper. By employing the degrees of freedom of the upper and lower goniometers of HB-1A, we were able to probe wave vectors in the $[H, K]$ plane near $[H, H, L]$. A Ge(115) monochromator was used to produce a neutron beam with $\lambda = 1.482$ Å

in the experiment at WAND. The one-dimensional ^{3}He detectors with 624 anodes can cover a wide range in reciprocal space by rotating the sample. A standard CCR was used to cover the temperature range between 4 K and 300 K.

The $Rb_{0.8}Fe_{1.5}S_2$ single crystals were grown by the Bridgman method with a one-step reacting. Stoichiometric amounts of high purity of a Rb ingot, Fe powder, and pieces of S were loaded in an alumina crucible in an argon gas filled glovebox; then the alumina crucible was sealed in a quartz tube under vacuum. The quartz tube was loaded into a box furnace and kept at 200 °C for 24 hours; then warmed up to 500 °C and held for 20 hours; heated slowly to 1050 °C for melting 5 hours; cooled down to 750 °C at a rate of 4 °C/hour; and finally cooled to room temperature. We obtained single crystals with dimensions up to $5 \times 5 \times 4$ mm^3.

III. RESULTS

We characterized the transport properties of several $Rb_{0.8}Fe_{1.5}S_2$ single crystals with a Quantum Design Physical Property Measurement System (PPMS). The results were very consistent among the different samples measured and indicated consistent phases. The in-plane resistivity shown in Fig. 2 (a) on a logarithm scale represents clear semiconducting behavior. This semiconducting characteristic is quite similar to that of the potassium compound with equivalent composition, $K_{0.8}Fe_{1.5}S_2$[40]. These results reveal, as expected, that $Rb_{0.8}Fe_yS_2$ and $K_{0.8}Fe_yS_2$ have similar transport characteristics. The enlarged resistivity from 240 K to 300 K in the inset of Fig. 2 (a) implies a phase transition at 275 K. This transition temperature corresponds to the onset of the in-plane stripe AF order observed by neutron diffraction, which is discussed in more detail below. The kink at 275 K corresponding to the stripe AF transition can also be seen in the susceptibility measurement. The difference between the zero field cooled (ZFC) and field cooled (FC) susceptibilities in Fig. 2 (b) suggests the possibility of a spin-glass phase coincident with the long range AF order in $Rb_{0.8}Fe_{1.5}S_2$, similar to that which has been proposed for $K_{0.88}Fe_{1.63}S_2$[44].

The lattice constants can be optimized by carrying out θ-2θ scans at nuclear Bragg peaks: scanning the angle of the incident beam and exit beam $S2$ (2θ), and rotating the sample angle (θ) by half of the step. The two well separated peaks in the scan at $Q = (1, 1, 0)$ are strong evidence for two structural phases existing in this sample[Fig. 2 (c)]. As estimated from the integrated peak intensities at 180 K, the '245' phase with $a = b = 3.765$ Å (peak centered at -52.70) has $\sim$65% volume fraction, and the '234' phase with $a = b = 3.889$ Å (peak centered at -50.90) has $\sim$35% volume fraction. We observed that the volume fractions of the two phases varied among our different samples[45]. The transition temperatures of each phase are consistent. The two phases have
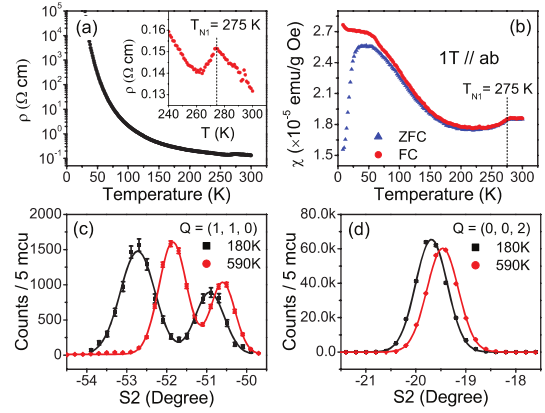
FIG. 2: (color online). (a) In-plane resistivity measurement of semiconducting $Rb_{0.8}Fe_{1.5}S_2$. (b) 1 Tesla Zero field cooled (ZFC) and field cooled (FC) dc magnetic susceptibility measurements with $H \parallel ab$-plane. A spin-glass like behavior appears below 55 K. A kink corresponding to the stripe AF order transition is observed in both resistivity and susceptibility measurements at $T = 275$ K. (c) The well separated peaks in the θ-2θ scans at nuclear reflection wave vector $Q = (1, 1, 0)$ demonstrate two different sets of in-plane lattice constants at 180 K and 590 K. (d) θ-2θ scans at $Q = (0, 0, 2)$ show a single lattice constant c within the instrument resolution. The error bars are one standard deviation and solid lines are fits to Gaussian function throughout this paper.

the same lattice constant $c = 13.889$ Å based on the θ-2θ scans at $Q = (0, 0, 2)$ at 180 K as shown in Fig. 2 (d). The peaks shift slightly due to the change of lattice constants at 590 K, but the peaks at $Q = (1, 1, 0)$ are still clearly distinguishable at 590 K[45]. This is in marked contrast with the behavior in phase-separated superconducting $K_{0.8}Fe_{1.6}Se_2$, where the non-magnetic phase with the more compact in-plane lattice constant merges together with the block AF phase at temperatures above the iron vacancy order-disorder transition at 520 K[23,32].

We first discuss the '245' phase, which has the block AF order and $\sqrt{5} \times \sqrt{5}$ iron vacancy order in Fig. 1 (a, b). The block AF order generates magnetic peaks at the wave vectors shown as the solid circles in the $[H, K]$ scattering planes for $L = odd$ in the inset figure of Fig. 3 (b). The $\sqrt{5} \times \sqrt{5}$ iron vacancy order produces nuclear peaks at the positions of the blank squares in the $[H, K]$ planes for $L = even$. The wave vectors connected by red and blue lines in the inset of Fig. 3 (b) originate from the left and right chiralities, respectively. The details of the diffraction have been described elsewhere[29]. By comparing the peak centers under the two sets of lattice constants, the set with $a = b = 3.765$ Å was determined to correspond to the block AF phase. Fig. 3 (a-c) represent scans at the magnetic wave vectors of $Q = (0.2, 0.4, 1)$, $Q = (0.2, 0.4, 3)$ and $Q = (1.2, 1.4, 1)$ at 212 K. The dramatic decrease of the magnetic peak intensity at $L = 3$ compared with that at $L = 1$ is consistent with c-axis-aligned moments together with the Fe^{2+} magnetic form
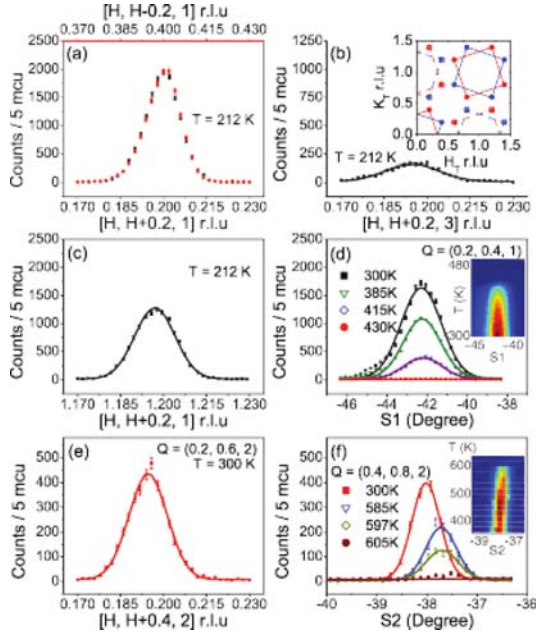
FIG. 3: (color online). Magnetic and nuclear reflection peaks associated with the block AF phase and $\sqrt{5} \times \sqrt{5}$ iron vacancy order. Scans through magnetic peaks at (a) $Q = (0.2, 0.4, 1)$, (b) $Q = (0.2, 0.4, 3)$ and (c) $Q = (1.2, 1.4, 1)$ along $[H, H+0.2]$ direction at $T = 212$ K. The red solid points in (a) through $Q = (0.4, 0.2, 1)$ are from the other chirality. (d) Rocking curve scans through magnetic peak $Q = (0.2, 0.4, 1)$ at selected temperatures of $T = 300, 385, 415$ and 430 K. (e) Scan through the nuclear peak at $Q = (0.2, 0.6, 2)$ along $[H, H + 0.4]$ direction associated with the $\sqrt{5} \times \sqrt{5}$ iron vacancy order at $T = 300$ K. (f) θ-2θ scans through nuclear peak at $Q = (0.4, 0.8, 2)$ at $T = 300, 585, 597$ and 605 K. The inset in (b) is the expected magnetic Bragg peaks (solid circles, $L = $ odd) and nuclear Bragg peaks (empty squares, $L = $ even) in tetragonal reciprocal space. The red and blue lines indicate two different chiralities. The insets in (d) and (f) are color maps of temperature dependence of reflection peaks corresponding to (d) and (f).

FIG. 4: (color online). Diffraction studies on the in-plane AF phase with rhombic iron vacancy order. Scans of magnetic peaks at wave vector of (a) $Q = (0.5, 0.5, 1)$, (b) $Q = (0.5, 0.5, 3)$, (d) $Q = (0.5, 0.5, 5)$ along the $[H, H]$ direction, and (c) $Q = (0.5, 0.5, 1)$ along L direction at selected temperatures. The inset of (a) is a color map of detailed temperature dependence. (e, f) show the nuclear peaks at the wave vectors of $H = 0.25, 0.5, 0.75; L = even$ and magnetic peaks at $H = 0.5, L = odd$ from the in-plane AF phase in the $[H, 3H, L]$ plane at 6 K and 280 K, respectively. The nuclear peaks were not changed, but the magnetic peaks disappeared at 280 K. The peaks at $H = 0.4, L = even$ originate from the $\sqrt{5} \times \sqrt{5}$ iron vacancy order in block AF phase. (g) Scans along $[H, 3H, 0]$ r.l.u at peaks of the rhombic iron vacancy order at $Q = (0.25, 0.75, 0)$ at 180 K, 600 K, 615 K and 630 K. The evolution of 2θ ($S2$) of the peak centers versus temperature indicates an in-plane lattice constant change across the in-plane magnetic structure transition in the inset of (g).

factor. Fig. 3 (a) also shows a scan at the equivalent wave vector $Q = (0.4, 0.2, 1)$ from the other chirality. The temperature dependence of the rocking curve scans demonstrates that the Néel temperature is approximately 425 K, which is significantly lower than that in the $A_{0.8}Fe_ySe_2$ system[5]. The fingerprint reflection peaks of the $\sqrt{5} \times \sqrt{5}$ iron vacancy order at $Q = (0.2, 0.6, 2)$ and $Q = (0.4, 0.8, 2)$ were also investigated and are represented in Fig. 3 (e, f). The order-disorder transition temperature of the iron vacancies occurs at 600 K. Here we have carried out θ-2θ scans in order to track the temperature dependence of the iron vacancy order, while accounting for thermal expansion.

Figure 4 summarizes the Bragg peaks of the '234' phase associated with the in-plane stripe AF order and rhombic iron vacancy order. The magnetic peaks are accurately centered at the wave vectors $Q = (0.5, 0.5, L =$

$1, 3, 5)$ at 180 K with lattice constants $a = b = 3.889$ Å, $c = 13.889$ Å. The magnetic peaks disappear completely by 280 K. The rhombic iron vacancy order together with the stripe AF order will induce magnetic peaks at $Q = (0.25, 0.25, L = odd)$, $Q = (0.75, 0.75, L = odd)$; and nuclear peaks at $Q = (0.25, 0.75, L = even)$, $Q = (0.75, 0.25, L = even)$, $Q = (0.5, 0.5, L = even)$ as demonstrated in the inset of Fig. 4 (d). We show reflection peaks in the $[H, 3H, L]$ plane in Fig. 4 (e) at 6 K and (f) at 280 K. The peaks centered at $Q = (0.25, 0.75, L)$, $Q = (0.5, 0.5, L)$ and $Q = (0.75, 2.25, L), L = 0, -2, -4$ are consistent with the rhombic iron vacancy order. The magnetic peak at $Q = (0.5, 1.5, 3)$ at 6 K in Fig. 4 (e) disappears at a temperature above $T_N = 275$ K. The
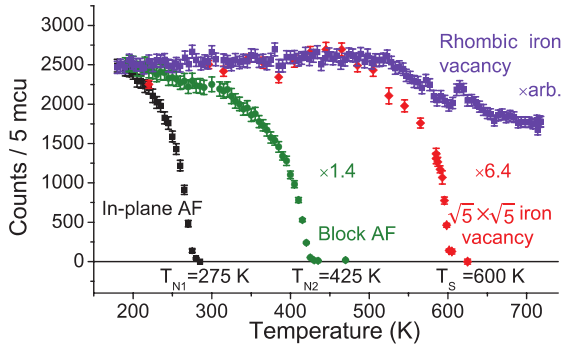
FIG. 5: (color online). Temperature dependence of order parameters for the in-plane stripe AF, the rhombic iron vacancy, the block AF and the $\sqrt{5} \times \sqrt{5}$ iron vacancy orders. The height of peaks at $Q = (0.5, 0.5, 1)$ fitted from $[H, H]$ scans shown as the black squares represent the stripe AF transition at $T_{N1} = 275$ K. The temperature dependence of peak height at $Q = (0.2, 0.4, 1)$ (green circle) fitted from rocking curve scans shows the block AF transition at $T_{N2} = 425$ K. The red diamonds obtained from θ-2θ scans through $Q = (0.4, 0.8, 2)$ indicate a first order-like transition of the $\sqrt{5} \times \sqrt{5}$ iron vacancies at $T_S = 600$ K. The rhombic iron vacancy order parameter integrated from the θ-2θ scans at $Q = (0.25, 0.75, 0)$ was collected from another piece of single crystal with the same composition aligned in the $[H, 3H, L]$ zone.

peaks at $Q = (0.4, 1.2, L = 0, -2, -4)$ originate from the $\sqrt{5} \times \sqrt{5}$ iron vacancy order of the '245' phase. The temperature dependence of the θ-2θ scans in Fig. 4 (g) shows the existence of the rhombic iron vacancy order at temperatures as high as 718 K; this is the reason that the two phases did not merge together at the temperature above the iron vacancy order-disorder transition at $T_S = 600$ K of the '245' phase in $Rb_{0.8}Fe_{1.5}S_2$[23,32]. From the inset, one can see a clear anomaly in the temperature dependence of the in-plane lattice constant at the AF transition indicating strong coupling between the structure and the antiferromagnetism. Residual peaks with temperature-independent intensities were observed at the magnetic peak positions above T_N in semiconducting $K_{0.81}Fe_{1.58}Se_2$[33]. However, we did not observe residual intensity at these positions above T_N in our semiconducting $Rb_{0.8}Fe_{1.5}S_2$ single crystals. This significant difference in these two systems, which otherwise behave quite similarly, remains to be understood.

In order to determine the transition temperatures of the '234' and '245' phases in $Rb_{0.8}Fe_{1.5}S_2$, we carefully measured the intensities of the fingerprint reflection peaks versus temperature; the results are shown in Fig. 5. The Néel temperature of the in-plane stripe AF order of $T_{N1} = 275$ K in the '234' phase of semiconducting $Rb_{0.8}Fe_{1.5}S_2$ is very close to $T_N = 280$ K of the stripe AF order in semiconducting $K_{0.81}Fe_{1.58}Se_2$[33]. The block AF order of the '245' phase has a Néel temperature at $T_{N2} = 425$ K and an iron vacancy ordering temperature of $T_S = 600$ K. These have a much larger separation than

those in the $A_{0.8}Fe_ySe_2$ system[5,6].

IV. DISCUSSIONS AND CONCLUSIONS

The similarity of the Néel temperatures suggests the crucial role of local moment superexchange interactions between the iron spins. Thus, we propose that strong correlation effects are essential to the formation of the stripe AF phase, in contrast with the spin-density-wave mechanism, which has been proposed as the origin of the magnetic order in the parent compounds of the iron pnictide superconductors[14,15]. The strong coupling scenario can also be reconciled with the absence of hole Fermi surfaces in $A_{0.8}Fe_ySe_2$[19–21]. Similar to the iron pnictides, the spin resonance modes associated with superconductivity in iron chalcogenide ($FeTe_{1-x}Se_x$ and $A_{0.8}Fe_ySe_2$) systems are compatible with nesting between the hole-electron or electron-electron Fermi surfaces[18]. In contrast with the pnictides, the in-plane magnetic orders in the iron chalcogenides are not compatible with nesting. The iron chalcogenides also have much larger local moments than the pnictide systems. The moments in the former are strongly suggestive of a localized rather than itinerant model for the magnetism.

The data in Fig. 5 show a surprising feature which indicates that the two different structural phases are in communication with each other. Specifically, there is a small increase ($\sim$10%) with increasing temperature in the intensity of the superlattice reflection associated with the rhombic vacancy order at the temperature at which the vacancies in the $\sqrt{5} \times \sqrt{5}$ phase become disordered. The increase in the integrated intensity is also confirmed by the scans at $Q = (0.25, 0.75, 0)$, $T = 600$ K, 615 K and 630 K in Fig. 4 (g). The intensity change suggests that the iron, partially occupied on the rhombic vacancy sites of the '234' phase below $T_S = 600$ K, moves to the iron vacancy disordered '245' phase. The movement of iron vacancies between the two phases in $Rb_{0.8}Fe_{1.5}S_2$ suggests a possible way to understanding the complex relationship between the AF structures and the superconductivity in the $A_{0.8}Fe_ySe_2$ system. In the compounds with net composition $A_{0.8}Fe_ySe_2$ ($1.5 < y < 1.6$), the material stabilized is a combination of the semiconducting phase $A_xFe_{1.5+\delta}Se_2$ ('234' phase) with in-plane stripe AF order and rhombic iron vacancy order together with the insulating phase, $A_{0.8}Fe_{1.6\pm\delta}Se_2$ ('245' phase) with the block AF order and $\sqrt{5} \times \sqrt{5}$ iron vacancy order. By adding more iron, only the volume fraction of the two phases is changed, that is, one traverses a first order two phase coexistence region between the '234' and '245' phases. This explains naturally why the Néel temperature of the in-plane stripe AF order is so stable. The block AF phase with $\sqrt{5} \times \sqrt{5}$ iron vacancy order, $A_{0.8}Fe_{1.6\pm\delta}Se_2$, ('245' phase) with $\delta = 0$, represents an end point of the two-phase coexistence region. In this picture, by further increasing the iron content beyond $y = 1.6$, the material then separates into a new iron rich superconducting, non-

magnetic phase, and the block AF phase with $\sqrt{5} \times \sqrt{5}$ iron vacancy order. We speculate that the '245' phase is a stable stoichiometric phase and that the $\sqrt{5} \times \sqrt{5}$ ordered iron vacancies cannot be readily occupied. This means that increasing the Fe content above 1.6 causes the formation of a new iron-rich phase which exhibits superconductivity. Concomitantly, the iron-rich SC phase is always accompanied by the '245' phase but the '245' phase is not the parent compound of the superconducting phase.

The results reported in this paper suggest a new strategy for probing the onset of superconductivity in the $A_x Fe_y Se_2$ type systems. In the pnictide systems, important insights have been gained by continuously tuning variables, such as the electron concentration by substitution (e.g., replacing Fe by Co or Ni) and thereby studying the evolution of the magnetism from the AF parent material to the superconducting material[11]. This is especially important at the onset of superconductivity where rich magnetic and superconducting behavior are observed. This approach does not seem to be possible in the $A_x Fe_y Se_2$ systems since the superconductivity seems to appear discontinuously. Yet it is clear from the results reported here that systematic variation of the S content in the $A_{0.8} Fe_y Se_{2-z} S_z$ system should enable one to study the continuous evolution from the 'parent' stripe AF sulphide to the superconducting mixed sulphide-selenide thus emulating studies in pnictide materials like those in $BaFe_2 As_{2-x} P_x$[46]. The $A_{0.8} Fe_y Se_{2-z} S_z$ system may be closely analogous to the $BaFe_2 As_{2-x} P_x$ system.

In summary, we have studied the magnetic and nuclear structures of semiconducting $Rb_{0.8} Fe_{1.5} S_2$ single crystals. Similar to semiconducting $K_{0.81} Fe_{1.58} Se_2$, there is an in-plane stripe AF phase with rhombic iron vacancy order, in addition to the block AF phase with $\sqrt{5} \times \sqrt{5}$ iron vacancy order. The robust $2.8 \pm 0.5 \mu_B$ in-plane ordered moments and $\sim$280 K Néel temperature of the stripe AF phase in semiconducting Fe-Se and Fe-S based systems suggest that strong electronic correlations play a dominant role in determining the nature of the magnetic state. The relationships among the block AF phase, the superconducting phase, and the in-plane stripe AF phase have been discussed in this paper. The $A_{0.8} Fe_y Se_{2-z} S_z$ system opens a new window to study the relationship between the antiferromagnetism and the superconductivity.

[*] Electronic address: `wangm@berkeley.edu`

[1] J. G. Guo, S. F. Jin, G. Wang, S. C. Wang, K. X. Zhu, T. T. Zhou, M. He, and X. L. Chen, Phys. Rev. B **82**, 180520(R) (2010).

[2] A. Krzton-Maziopa, Z. Shermadini, E. Pomjakushina, V. Pomjakushin, M. Bendele, A. Amato, R. Khasanov, H. Luetkens, K. Conder, J. Phys. Condens. Matter **23**, 052203 (2011).

[3] M. H. Fang, H. D. Wang, C. H. Dong, Z. J. Li, C. M. Feng, J. Chen, H. Q. Yuan, Europhys. Lett. **93**, 47004 (2011).

[4] A. F. Wang, J. J. Ying, Y. J. Yan, R. H. Liu, X. G. Luo, Z. Y. Li, X. F. Wang, M. Zhang, G. J. Ye, P. Cheng, Z. J. Xiang, X. H. Chen, Phys. Rev. B **83**, 060512 (2011).

[5] W. Bao, Q. Huang, G. F. Chen, M. A. Green, D. M. Wang, J. B. He, X. Q. Wang, Y. Qiu, Chin. Phys. Lett. **28**, 086104 (2011).

[6] F. Ye, S. Chi, W. Bao, X. F. Wang, J. J. Ying, X. H. Chen, H. D. Wang, C. H. Dong, and M. H. Fang, Phys. Rev. Lett. **107**, 137003 (2011).

[7] C. de la Cruz, Q. Huang, J. W. Lynn, J. Li, W. Ratcliff II, J. L. Zarestky, H. A. Mook, G. F. Chen, J. L. Luo, N. L. Wang, P. C. Dai, Nature (London) **453**, 899 (2008).

[8] Q. Huang, Y. Qiu, W. Bao, M. A. Green, J. W. Lynn, Y. C. Gasparovic, T. Wu, G. Wu, and X. H. Chen, Phys. Rev. Lett. **101**, 257003 (2008).

[9] S. L. Li, C. de la Cruz, Q. Huang, G. F. Chen, T. L. Xia, J. L. Luo, N. L. Wang, and P. C. Dai, Phys. Rev. B **80**, 020504(R) (2009).

[10] J. W. Lynn and Pengcheng Dai, Physica C **469**, 469-476 (2009).

[11] D. C. Johnston, Adv. in Phys. **59**, 803 (2010).

[12] P. C. Dai, J. P. Hu, and E. Dagotto, Nat. Phys. **8**, 709-718 (2012).

[13] M. Wang et al., Nat. Commun. **4**, 2874 (2013).

[14] J. Dong et al., Europhys. Lett. **83**, 27006 (2008).

[15] I. I. Mazin, D. J. Singh, M. D. Johannes, and M. H. Du, Phys. Rev. Lett. **101**, 057003 (2008).

[16] T. A. Maier and D. J. Scalapino, Phys. Rev. B **78**, 020514 (2008).

[17] J. T. Park, G. Friemel, Yuan Li, J.-H. Kim, V. Tsurkan, J. Deisenhofer, H.-A. Krug von Nidda, A. Loidl, A. Ivanov, B. Keimer, and D. S. Inosov, Phys. Rev. Lett. **107**, 177005 (2011).

[18] G. Friemel, J. T. Park, T. A. Maier, V. Tsurkan, Yuan Li, J. Deisenhofer, H. A. Krug von Nidda, A. Loidl, A. Ivanov, B. Keimer, and D. S. Inosov, Phys. Rev. B **85**, 140511(R) (2012).

[19] Y. Zhang, L. X. Yang, M. Xu, Z. R. Ye, F. Chen, C. He, J. Jiang, B. P. Xie, J. J. Ying, X. F. Wang, X. H. Chen, J. P. Hu, D. L. Feng, Nat. Mater. **10**, 273 (2011).

[20] T. Qian, X.-P. Wang, W.-C. Jin, P. Zhang, P. Richard, G. Xu, X. Dai, Z. Fang, J.-G. Guo, X.-L. Chen, and H. Ding,

Phys. Rev. Lett. **106**, 187001 (2011).

[21] D. X. Mou *et al.*, Phys. Rev. Lett. **106**, 107001 (2011).

[22] E. Dagotto, Rev. Mod. Phys. **85**, 849 (2013).

[23] A. Ricci, N. Poccia, B. Joseph, G. Arrighetti, L. Barba, J. Plaisier, G. Campi, Y. Mizuguchi, H. Takeya, Y. Takano, N. L. Saini, A. Bianconi, Supercond. Sci. and Technol. **24**, 082002 (2011).

[24] A. Ricci *et al.*, Phys. Rev. B **84**, 060511(R) (2011).

[25] F. Chen *et al.*, Phys. Rev. X **1**, 021020 (2011).

[26] W. Li, H. Ding, Z. Li, P. Deng, K. Chang, K. He, S. Ji, L. Wang, X. Ma, J. P. Hu, X. Chen, and Q. K. Xue, Phys. Rev. Lett. **109**, 057003 (2012).

[27] W. Li, H. Ding, P. Deng, K. Chang, C Song, K. He, L. Wang, X. M, J. Hu, X. Chen, and Q. Xue, Nat. Phys. **8**, 126-130 (2012).

[28] Z. Wang, Y. J. Song, H. L. Shi, Z.W. Wang, Z.Chen, H. F. Tian, G. F. Chen, J. G. Guo, H. X. Yang, J. Q. Li, Phys. Rev. B **83**, 140505(R) (2011).

[29] M. Wang *et al.*, Phys. Rev. B **84**, 094504(R) (2011).

[30] W. Bao, G. N. Li, Q. Huang, G. F. Chen, J. B. He, D. M. Wang, M. A. Green, Y. M. Qiu, J. L. Luo, M. M. Wu, Chin. Phys. Lett. **30**, 027402 (2013).

[31] N. Lazarević, M. Abeykoon, P. W. Stephens, H. Lei, E. S. Bozin, C. Petrovic, and Z. V. Popović, Phys. Rev. B **86**, 054503 (2012).

[32] S. V. Carr, D. Louca, J. Siewenie, Q. Huang, A. F. Wang, X. H. Chen, and P. C. Dai, Phys. Rev. B **89**, 134509 (2014).

[33] J. Zhao, H. Cao, E. Bourret-Courchesne, D. H. Lee, and R. J. Birgeneau, Phys. Rev. Lett. **109**, 267003 (2012).

[34] X. X. Ding, D. L. Fang, Z. Y. Wang, H. Yang, J. Z. Liu, Q. Deng, G. B. Ma, C. Meng, Y. H. Hu, and Hai-Hu Wen, Nat. Commun. **4**, 1897 (2013).

[35] R. Yu, J. X. Zhu, and Q. Si, Phys. Rev. Lett. **106**, 186401 (2011).

[36] D. M. Wang, J. B. He, T. L. Xia, and G. F. Chen, Phys. Rev. B. **83**, 132502 (2011).

[37] J. G. Guo, X. L. Chen, G. Wang, S. F. Jin, T. T. Zhou, and X. F. Lai, Phys. Rev. B **85**, 054507 (2012).

[38] K. F. Wang, H. C. Lei, and C. Petrovic, Phys. Rev. B. **84**, 054526 (2011).

[39] H. C. Lei, M. Abeykoon, E. S. Bozin, K. F. Wang, J. B. Warren, and C. Petrovic, Phys. Rev. Lett. **107**, 137002 (2011).

[40] Y. Cai, Z. Wang, Z. W. Wang, Z. A. Sun, H. X. Yang, H. F. Tian, C. Ma, B. Zhang, and J. Q. Li, Europhys. Lett. **103**, 37010 (2013).

[41] J. J. Ying, Z. J. Xiang, Z. Y. Li, Y. J. Yan, M. Zhang, A. F. Wang, X. G. Luo, and X. H. Chen, Phys. Rev. B **85**, 054506 (2012).

[42] N. Lazarević, H. Lei, C. Petrovic, and Z. V. Popović, Phys. Rev. B **84**, 214305 (2011).

[43] H. Sabrowsky, M. Rosenberg, D. Welz, P. Deppe, Schäfer, J. Magn. Magn. Mater. 54-57, 1497 (1986).

[44] H. C. Lei, M. Abeykoon, E. S. Bozin, and C. Petrovic, Phys. Rev. B **83**, 180503(R) (2011).

[45] The θ-2θ scan at $Q = (1,1,0)$ on another piece of single crystal indicated $45 \pm 5\%$ '245' phase and $55 \pm 5\%$ '234' phase. The $(1,1,0)$ peaks from the two phases are separated as high as 718 K. Our neutron powder diffraction refinement on 2 grams sample ground by single crystals revealed that only 2% '245' phase and 98% '234' phase in the sample at 500 K.

[46] S. Kasahara, T. Shibauchi, K. Hashimoto *et al.*, Phys. Rev. B **81**, 184519 (2010).

4.3   Outlook

Understanding this family of compounds is a very active and important area of research in the iron based superconductors. Our study not only offers needed information on these materials, but also suggests that studying mixed anion substitutions may be a more suitable method to explore the superconductivity in these materials.

Chapter 5

Spin Waves and Spatially Anisotropic Exchange Interactions in the S=2 Stripe Antiferromagnet $Rb_{0.8}Fe_{1.5}S_2$

5.1   Introduction

Having collaborated with Meng on the transport and basic properties measurements for the earlier paper, I learned about the complexity of the structure and magnetism through that research. Thus, I was quite excited for the opportunity to collaborate again with Meng in a time of flight neutron experiment to study the spin excitations of this material. During the preparation for this experiment, we were very selective in choosing crystals which did not have misoriented grains, as needed to obtain clean data. When we were selecting samples using the ALF neutron laue machine at ISIS, it turned out that a significant portion of the sample mass that we had shipped to ISIS contained multiple grain orientations. Ultimately, we used about a third of the sample mass which we shipped! Such careful selection of crystals was crucial to obtaining the results of the following paper.

This paper was accepted for publication as: Phys. Rev. B 92, 041109R, 2015.

5.2   Paper

Spin Waves and Spatially Anisotropic Exchange Interactions in the $S = 2$ Stripe Antiferromagnet $Rb_{0.8}Fe_{1.5}S_2$

Meng Wang,[1, *] P. Valdivia,[1] Ming Yi,[1] J. X. Chen,[2] W. L. Zhang,[3] R. A. Ewings,[4] T. G. Perring,[4] Yang Zhao,[5, 6] L. W. Harriger,[5] J. W. Lynn,[5] E. Bourret-Courchesne,[7] Pengcheng Dai,[8] D. H. Lee,[1, 7] D. X. Yao,[2] and R. J. Birgeneau[1, 7, 9]

[1]*Department of Physics, University of California, Berkeley, California 94720, USA*
[2]*School of Physics and Engineering, Sun Yat-Sen University, Guangzhou 510275, China*
[3]*Institute of Physics, Chinese Academy of Sciences, P. O. Box 603, Beijing, 100190, China*
[4]*ISIS Pulsed Muon and Neutron Source, STFC Rutherford Appleton Laboratory, Harwell Oxford, Didcot, OX11 0QX, United Kingdom*
[5]*NIST Center for Neutron Research, National Institute of Standards and Technology, Gaithersburg, Maryland 20899, USA*
[6]*Department of Materials Science and Engineering, University of Maryland, College Park, Maryland 20742, USA*
[7]*Materials Science Division, Lawrence Berkeley National Laboratory, Berkeley, California 94720, USA*
[8]*Department of Physics and Astronomy, Rice University, Houston, Texas 77005, USA*
[9]*Department of Materials Science and Engineering, University of California, Berkeley, California 94720, USA*

An inelastic neutron scattering study of the spin waves corresponding to the stripe antiferromagnetic order in insulating $Rb_{0.8}Fe_{1.5}S_2$ throughout the Brillouin zone is reported. The spin wave spectra are well described by a Heisenberg Hamiltonian with anisotropic in-plane exchange interactions. Integrating the ordered moment and the spin fluctuations results in a total moment squared of $27.6 \pm 4.2\mu_B^2$/Fe, consistent with $S \approx 2$. Unlike XFe$_2$As$_2$ (X = Ca, Sr, and Ba), where the itinerant electrons have a significant contribution, our data suggest that this stripe antiferromagnetically ordered phase in $Rb_{0.8}Fe_{1.5}S_2$ is a Mott-like insulator with fully localized $3d$ electrons and a high-spin ground state configuration. Nevertheless, the anisotropic exchange couplings appear to be universal in the stripe phase of Fe pnictides and chalcogenides.

Superconductivity emerges in the vicinity of antiferromagnetism (AFM) in both copper-based and iron-based high-transition temperature (high-T_c) superconductors[1–4]. However, the AFM in the cuprate high-T_c and iron-based superconductors could have different origins. The parent compound of the copper oxide superconductors is a Mott insulator with $S = 1/2$ local moments[5]. In the iron pnictides, the parent compounds are bad metals with multiple bands crossing the Fermi level. The stripe AF ordering wavevectors coincide with the wave vectors connecting the centers of the electron and hole Fermi surfaces[6]. In fact many view the AF order as due to the Fermi surface nesting.

From a localized point of view, with 6 electrons in the iron $3d$ orbitals of Fe^{2+}, the maximum total spin is $S = 2$. This spin state can be realized when the Hund's rule coupling energy, J_H, dominates over the crystal-field splitting associated with the FeM_4 (M = pnictigens or chalcogens) structural unit. On the other hand, a crystal field splitting, Δ_{CF}, comparable to the Hund's coupling J_H can lead to an intermediate-spin $S = 1$ state. In the large crystal field extreme, the $3d^6$ ions of Fe^{2+} will form a low-spin singlet $S = 0$ state[7–9]. In the presence of itinerant carriers the spin must be less than $S = 2$ due to charge fluctuations. Thus, the observation of $S = 2$ for Fe^{2+}would require the system to be predominately localized. Not surprisingly, the various values of ordered moments observed in different iron-based materials have been interpreted in terms of both the local moment picture and the itinerant carrier picture[7–13]. As to the value of the fluctuating local moment, inelastic neutron scattering experiments revealed an increase of S from $S \approx 1$ at 10 K to $S \approx 3/2$ at 300 K for Fe$_{1.1}$Te and a constant $S = 1/2$ for BaFe$_2$As$_2$[14–16]. In addition, an X-ray emission spectroscopy study was interpreted to imply that the iron spin-state varied between $S = 0$ and 2 in the rare-earth doped Ca$_{1-x}$RE$_x$Fe$_2$As$_2$ as a function of temperature[17]. These findings suggest that the magnetism of the iron pnictides and chalcogenides should be understood from a point of view where both itinerant carriers and local moments coexist.

Recently, the discovery of 30 K superconductivity in the $A_{0.8}$Fe$_y$Se$_2$ (A = alkali metal) materials generated a great deal of research activities due to the lack of the Fermi surface nesting conditions necessary for the itinerant understanding of superconducting pairing[18]. Interestingly, a stripe AF order with a rhombic iron vacancy order [Fig. 1 (a,b)] was recently discovered in K$_{0.81}$Fe$_{1.58}$Se$_2$ and Rb$_{0.8}$Fe$_{1.5}$S$_2$, which are insulating compounds in proximity to the superconducting phase in this iron chalcogenide family. The stripe AF orders in these materials have strikingly similar Néel temperatures of $T_N = 280$ K and 275 K, respectively, and moment size of $M = 2.8 \pm 0.5\mu_B$[19, 20]. More importantly, this stripe
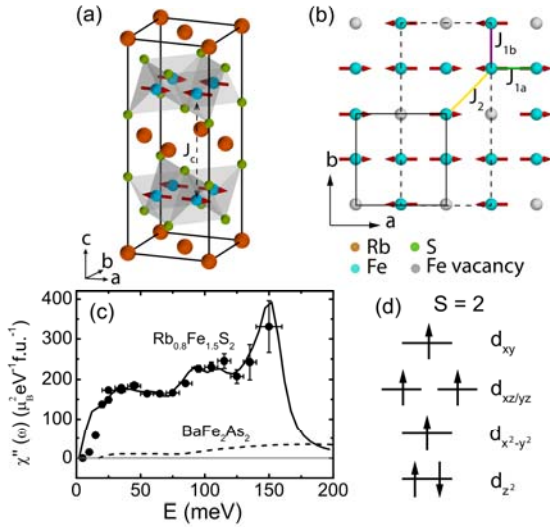
FIG. 1: (color online). Three- (a) and Two- (b) dimensional structures of the stripe AF order with rhombic iron vacancy order in $Rb_{0.8}Fe_{1.5}S_2$. We use the orthorhombic unit cell as shown by the solid square in (b) with lattice parameters of $a = 5.58$ Å, $b = 5.39$ Å, and $c = 13.889$ Å. The wave vector Q is defined as $Q = [H, K, L] = (2\pi H/a, 2\pi K/b, 2\pi L/c)$ in reciprocal lattice units (r.l.u). The dashed rectangle is the real magnetic unit cell. (c) Dynamic susceptibility $\chi''(\omega)$ as a function of energy with E_i =35 (■), 170 (◇), and 250 (●) meV at 8 K. The solid line is computed by the model discussed in the text. The dashed line is the dynamic susceptibility of $BaFe_2As_2$ from Ref. [15]. (d) A candidate for the high-spin ground state configuration of the stripe AF order[7].

AF order has the same structure as the ubiquitous magnetic order in the parent phases of iron pnictides, and has hence been proposed as a candidate parent compound for the superconducting phase in $A_{0.8}Fe_ySe_2$[19, 21]. However, the previous reports on the stripe AF order always showed a mesoscopic interdigitation of the stripe AF order with a robust block AF phase with a $\sqrt{5} \times \sqrt{5}$ iron vacancy order[19, 20]. Therefore, it is very important to understand the nature of this magnetic order by quantitatively characterizing the spin waves in the pure stripe AF phase.

In this paper, we report inelastic neutron scattering studies of the spin wave excitations of the stripe AF order in insulating $Rb_{0.8}Fe_{1.5}S_2$. Only the spin excitations associated with the stripe AF order are observed in our experiment, suggesting a nearly 100% stripe AF order volume fraction. In the presence of iron vacancy order, there are six iron atoms per magnetic unit cell. Hence, one expects three doubly-degenerate spin wave branches. The first acoustic and the second optical branches are observed clearly in both momentum and energy scans in our experiment. The third branch is flat in momentum space and can only be observed by scans in energy. By fitting the spin excitation spectrum

to a Heisenberg Hamiltonian with spatially anisotropic exchange couplings ($SJ_{1a} = 42 \pm 5$, $SJ_{1b} = -20 \pm 2$, $SJ_2 = 17 \pm 2$, $SJ_c = 0.29 \pm 0.05$ and $SJ_s = 0.09 \pm 0.02$ meV), all of the branches of the spin excitations can be accurately described. Furthermore, the total dynamic spin fluctuation moment spectrum is calculated to be $\langle m \rangle^2 \approx 20\mu_B^2$/Fe, similar to that in the block insulating AF $Rb_{0.89}Fe_{1.58}Se_2$[22], revealing the spin S = 2. Knowing that the stripe AF order is an insulator with a large charge gap (~ 1 eV)[23], the spin S = 2 suggests that all Fe $3d$ electrons are fully localized.

Our experiments were carried out on the MAPS time-of-flight (TOF) chopper spectrometer at the Rutherford-Appleton Laboratory, Didcot, UK, and the BT-7 thermal triple-axis spectrometer at the NIST Center for Neutron Research, Gaithersburg, USA. We coaligned 1.5 grams of single crystals with a mosaic of 1.5° full width at half maximum for the two experiments. For the TOF experiment at MAPS, we aligned the c axis of the sample parallel to the incident beam at energies of $E_i = 35, 80, 170$ and 250 meV at 8 K. The intensities were normalized to absolute units by vanadium incoherent scattering. For the low energy neutron scattering measurements performed at BT-7, we fixed the final energy at 14.7 meV, with horizontal collimations of open-80′-S-80′-120′, where S = sample, and two pyrolytic graphite filters after the sample[24]. Uncertainties where indicated represent one standard deviation.

We show spin excitations in the $[H, K]$ plane at various energies in Fig.2 (a-e). The spin excitations stem from the AF wave vectors, disperse outwards and separate into two arcs at 65 ± 5 (this notation represents the signal averaged over $60 < E < 70$ meV) and 75 ± 5 meV. At the energy of 110 ± 9 meV, the wave vectors rotate 90°.

To describe the spin waves in $Rb_{0.8}Fe_{1.5}S_2$, we employed a Heisenberg model with in-plane nearest-(J_{1a}, J_{1b}), and next-nearest-(J_2) neighbor exchange couplings, together with the coupling between layers, J_c, as shown in Fig. 1 (a) and Fig. 1 (b), and the single ion anisotropy term, J_s. The Hamiltonian can be written as:

$$\hat{H} = \frac{J_{r,r'}}{2}\sum_{r,r'}\mathbf{S_r} \cdot \mathbf{S_{r'}} - J_s \sum_r (\mathbf{S_r^z})^2, \quad (1)$$

where $J_{r,r'}$ are the effective exchange couplings and (r, r') label the iron sites[25]. The spin wave excitation spectrum can be expressed analytically by solving Eq. (1) using the linear spin wave approximation[11, 13, 16, 22]. We performed resolution convoluted fits to the time-of-flight data using the Tobyfit program[26]. From the best fit to the experimental data, the parameters were determined to be $SJ_{1a} = 42 \pm 5$, $SJ_{1b} = -20 \pm 2$, and $SJ_2 = 17 \pm 2$ meV, and for computational convenience an energy independent damping $\Gamma = 7 \pm 2$ meV. The widths of the spin wave peaks in H and K were close to being instrumental resolution limited as expected for an
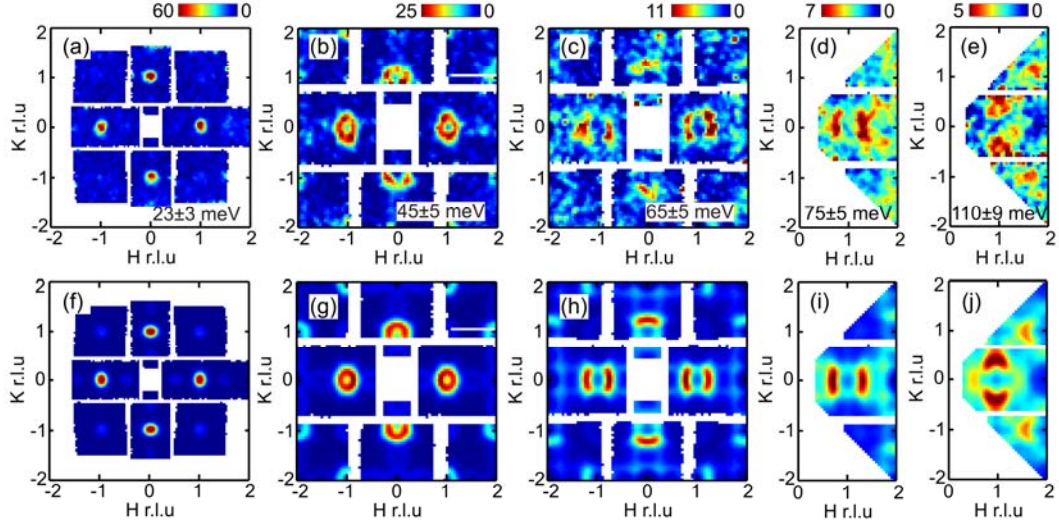
FIG. 2: (color online). Constant energy slices in the $[H, K]$ plane of the spin waves averaged at energies of (a) 23 ± 3 meV with $E_i = 80$ meV, and (b) 45 ± 5, (c) 65 ± 5, (d) 75 ± 5, (e) 110 ± 9 meV with $E_i = 250$ meV, all at 8 K. (f-j) Simulations of spin excitations at the identical energies as in (a-e) using the exchange couplings from the best fits to the experimental data. The simulations were convoluted with the instrumental resolution. The color bar is the same for each energy transfer in units of $mbarnSr^{-1}meV^{-1}f.u.^{-1}$.

insulator; this also holds true for $K_{0.81}Fe_{1.58}Se_2$[27, 28]. The simulations with the fit parameters at the identical energies of Fig. 2 (a-e) are presented in Fig. 2 (f-j).

To compare quantitatively the experimental data with the model, we plot cuts along the $[H, 0]$ and $[1, K]$ directions and compare the cuts with the best fits for a wide range of energies in Fig. 3. The fits are in good agreement with the experimental data at all energies. The small discrepancy near $Q = (2, 0)$ is due to an acoustic phonon. The weaker and flatter cut along the $[1, K]$ direction at 65 ± 5 meV in Fig. 3 (g) and the cut along the $[H, 0]$ direction at 110 ± 9 meV in Fig. 3 (d) are consistent with the splitting of the first branch along the $[H, 0]$ direction and the 90° rotation of the second branch.

Fig. 4 (a) and Fig. 4 (b) show the dispersion relations along the $[H, 0]$ and $[1, K]$ directions with $E_i = 250$ meV at 8 K, respectively. The spin excitations from the second twin at $Q = (0.5, 0), E = 25$ meV in Fig. 4 (a) and the second branch of spin excitations at energies between 90 and 120 meV in Fig. 4 (b) can be observed. The dispersion of the spin excitations extracted from ex-

tensive constant energy cuts and Q cuts, together with the results of simulations with the best fit parameters are plotted in Fig. 4 (c) and Fig. 4 (d). Three branches of spin excitations can be seen. We tried to fit the dispersions in $Rb_{0.8}Fe_{1.5}S_2$ with the parameters obtained for $K_{0.81}Fe_{1.58}Se_2$[27]. The dispersions of the first branch along the $[H, 0]$ and $[1, K]$ directions were matched very well, but the second branch along the $[1, K]$ direction deviated from the experimental data[see supplementary information].

In order to determine the exchange coupling between layers, J_c, and the single-ion anisotropy term, J_s, we measured the L-modulation of the low energy spin excitations at 2 K. The measurements show that a gap in the spin excitations opens up below $\Delta = 6$ meV and that J_c only affects the spin excitation spectrum below 15 meV [Fig. 4 (e)]. By fitting the L-modulated spin excitation spectrum, we determined $SJ_c = 0.29 \pm 0.05$ and $SJ_s = 0.09 \pm 0.02$ meV. The temperature dependence of the spin gap was also studied and is presented in Fig. 4 (f). The spin gap remained sharp right up to
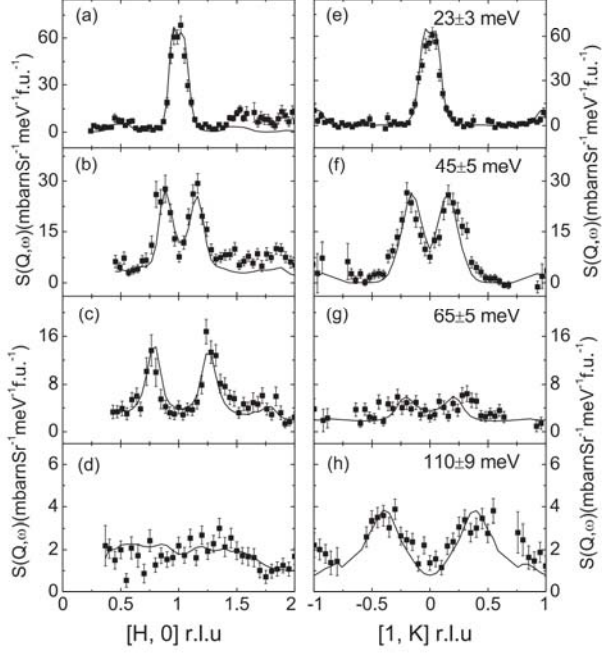
FIG. 3: Constant energy cuts through $Q = (1,0)$ along the $[H, 0]$ (a-d) and $[1, K]$ (e-h) directions averaged at energies of 23 ± 3 meV with $E_i = 80$ meV, and $45 \pm 5, 65 \pm 5$, and 110 ± 9 meV with $E_i = 250$ meV, at 8 K. The solid lines are the best fits obtained from the Tobyfit program.
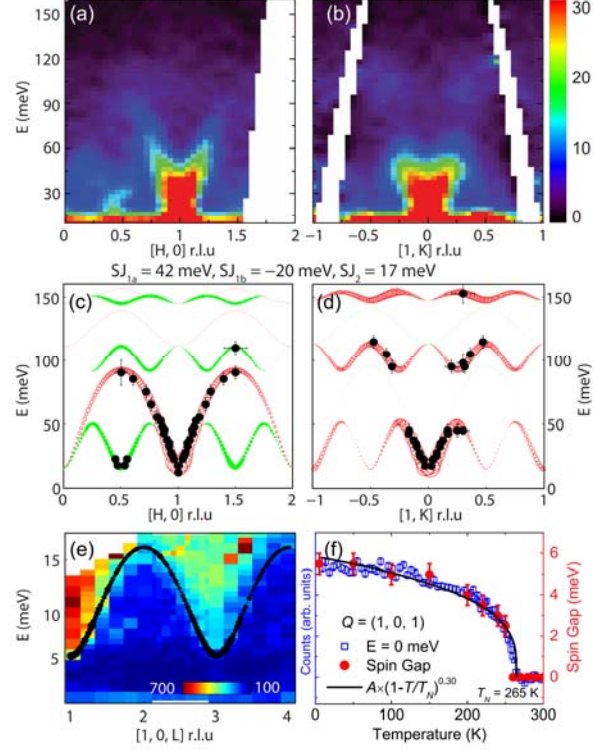

FIG. 4: (color online). (a) Spin excitations along the $[H, 0]$ direction, averaging over $K = \pm 0.2$ r.l.u and (b) along the $[1, K]$ direction, averaging over $H = 1 \pm 0.2$ r.l.u with $E_i = 250$ meV at 8 K. (c, d) The dispersion extracted from experimental data and simulations with the best fit parameters. The red circles are from the first twin, and the green circles are from the second twin[see supplementary information]. The intensity of the simulations is proportional to $\chi''(\mathbf{q}, \omega) \times \sqrt{E}$. (e) The L-modulation of the low energy spin excitations at 2 K and simulations with $SJ_c = 0.29, SJ_s = 0.09$ meV. The intensity is proportional to $\chi''(\mathbf{q}, \omega)$. (f) The temperature evolution of the spin gap measured at $Q = (1, 0, 1)$. The solid line is the result of a fit to the magnetic order parameter (the blue squares) with $A(1 - T/T_N)^\beta$, where A is a scaler, $T_N = 265$ K, and $\beta = 0.30$.

the phase transition. The scaled magnetic order parameter is plotted along with the temperature dependent spin gap. The evolution of the spin gap with temperature follows the trend of the AF order, in agreement with the behavior observed in K_2NiF_4, a quasi-two-dimensional (2D) Heisenberg AF insulator[28].

To unveil the spin state in the stripe AF order of $Rb_{0.8}Fe_{1.5}S_2$, we examined the sum rule of the magnetic neutron scattering. One can calculate the total fluctuating moment squared $\langle \mathbf{m}^2 \rangle$ by integrating the susceptibility $\chi''(\mathbf{q}, \omega)$ over the band width of the spin excitations via

$$\langle \mathbf{m}^2 \rangle = \frac{3\hbar}{\pi} \int_{-\infty}^{+\infty} \frac{\int \chi''(\mathbf{q}, \omega) d\mathbf{q} / \int d\mathbf{q}}{1 - \exp(-\hbar\omega/k_B T)} d\omega. \quad (2)$$

The total moment sum rule is $M_0^2 = M^2 + \langle \mathbf{m}^2 \rangle = g^2 S(S + 1)$, where g is the Landé g-factor and M is the static moment. Thus the spin S can be extracted[22, 29, 30].

The averaged dynamic susceptibility in a Brillouin zone $\chi''(\omega) = \int \chi''(\mathbf{q}, \omega) d\mathbf{q} / \int d\mathbf{q}$ is plotted in Fig. 1 (c). The spin fluctuations in $Rb_{0.8}Fe_{1.5}S_2$ are obviously stronger than those in $BaFe_2As_2$. Integrating the dynamic susceptibility through all the spin excitation band width results in $29.7 \pm 5.5 \mu_B^2$/formula unit (f.u.), and thus $19.8 \pm 3.7 \mu_B^2$/Fe. Taking the ordered moment $M = 2.8 \pm 0.5 \mu_B$ into account, the total moment squared per Fe is $27.6 \pm 4.2 \mu_B^2$, which, assuming $g = 2.0$, results in a spin $S = 2.2 \pm 0.2$, which is equal to the upper limit of $24 \mu_B^2$ and $S = 2$ as the Hund's rule result for

TABLE I: The magnetic exchange couplings and spin states in the stripe AF order of iron pnictides and chalcogenides[13, 16, 27].

Compounds	SJ_{1a}	SJ_{1b}	SJ_2(meV)	S	$M(\mu_B)$	$T_N(K)$
$CaFe_2As_2$	50(10)	−6(5)	19(4)	1/2	0.80	173
$BaFe_2As_2$	59(2)	−9(2)	14(1)	1/2	0.87	143
$SrFe_2As_2$(L)	31(1)	−5(5)	22(1)	0.30	0.94	220
$SrFe_2As_2$(H)	39(2)	−5(5)	27(1)	0.69	0.94	220
$K_{0.85}Fe_{1.54}Se_2$	38(7)	−11(5)	19(2)	−	2.8	280
$Rb_{0.8}Fe_{1.5}S_2$	42(5)	−20(2)	17(2)	2	2.8(0.5)	265

the $3d$ Fe^{2+} within the error. The results reveal that to within the errors all six $3d$ electrons of Fe^{2+} are associated with the local moment in the high-spin state. A candidate spin configuration is illustrated in Fig. 1 (d). The fact that the carriers are fully localized in $Rb_{0.8}Fe_{1.5}S_2$ is consistent with our photoemission measurements on several pieces of single crystals from the same batch. These measurements also reveal a large charge gap below the Fermi energy, suggesting that the stripe AF phase is a Mott-like insulator with the integer spin S = 2[21, 31], rather than a small gap band insulator[19, 20, 32]. The Mott localization in $Rb_{0.8}Fe_{1.5}S_2$ is realized by the presence of the rhombic iron vacancy order, which has enlarged the in-plane Fe-Fe distance, and thus, enhanced the correlation[21, 31].

Several theoretical methods have been successfully explored to describe the spin waves of the stripe AF order: a combination of density functional theory (DFT) and dynamic mean field theory (DMFT)[33, 34]; a Heisenberg model with the anisotropic in-plane exchange couplings $J_{1a}(> 0)$, $J_{1b}(< 0)$, and J_2[11, 13, 16, 27]; and a Heisenberg model with J_1, J_2 and a large biquadratic coupling K[10, 35, 36]. The spin waves of $Rb_{0.8}Fe_{1.5}S_2$ could be described by either model. In particular the rhombic iron vacancy order which has already broken the C_4 symmetry forms at a temperature higher than 718 K[20]. The anisotropic J_{1a} and J_{1b} in $Rb_{0.8}Fe_{1.5}S_2$ could originate from the structural orthorhombicity and the possible orbital ordering[37]. For the $J_1 - J_2 - K$ model, the exchange couplings are estimated to be $J_1S = (J_{1a} + J_{1b})S/2 = 11 \pm 3$, $J_2S = 17 \pm 2$, and $KS = (J_{1a} - J_{1b})S/4 = 15.5 \pm 1.4$ meV[35]. The biquadratic term could be enhanced by the dynamic fluctuations in the chalcogen height. Distinguishing the two models microscopically is beyond the scope of this work.

We list in Table 1 the fitted magnetic exchange couplings and measured Fe spin values in a number of stripe phase Fe arsenides and chalcogenides. The Fermi surfaces in these materials vary significantly as do, concomitantly, the conductivity, the ordered moments and the effective spin values. In spite of this, the exchange couplings measured in units of SJ are remarkably universal. This result is both striking and mysterious. It remains to be seen how this relates to the superconductivity of the iron chalcogenides.

In summary, we have studied the spin waves of the pure stripe AF order in $Rb_{0.8}Fe_{1.5}S_2$ over a wide range in reciprocal space and energy. Our inelastic neutron scattering data reveal that even though the stripe AF order has strikingly similar SJ with all the other iron pinctides and chalcogenides, it is an ideal S = 2 Heisenberg antiferromagnet with fully localized moments exhibiting Mott insulator behavior. This indicates the importance of strong electron correlations in the iron-based superconductors, which have thus far mostly been understood from an itinerant point of view. Our results hence form a bridge that connects the iron-based superconductors to the cuprates.

* Electronic address: wangm@berkeley.edu
[1] M. A. Kastner, R. J. Birgeneau, G. Shirane, and Y. Endoh, Rev. Mod. Phys. **70**, 897 (1998).
[2] R. J. Birgeneau, C. Stock, J. M. Tranquada, and K. Yamada, J. Phys. Soc. Jpn. 75, 111003 (2006).
[3] D. Johnston, Adv. Phys. **59**, 803 (2010).
[4] P. C. Dai, J. P. Hu, and E. Dagotto, Nat. Phys. **8**, 709 (2012).
[5] S. M. Hayden et al., Phys. Rev. Lett. **76**, 1344 (1996).
[6] J. Dong et al., Europhys. Lett. **83**, 27006 (2008).
[7] Q. Si, and E. Abrahams, Phys. Rev. Lett. **101**, 076401 (2008).
[8] F. Krüger, S. Kumar, J. Zaanen, and J. van den Brink, Phys. Rev. B **79**, 054504 (2009).
[9] K. Haule, and G. Kotliar, New J. Phys. **11**, 025021 (2009).
[10] D. Stanek, O. P. Sushkov, and G. S. Uhrig, Phys. Rev. B **84**, 064505 (2011).
[11] J. Zhao et al., Nat. Phys. **5**, 555 (2009).
[12] S. O. Diallo et al., Phys. Rev. Lett. **102**, 187206 (2009).
[13] R. A. Ewings et al., Phys. Rev. B **78**, 220501(R) (2008); Phys. Rev. B **83**, 214519 (2011).
[14] I. A. Zaliznyak et al., Phys. Rev. Lett. **107**, 216403 (2011).
[15] M. S. Liu et al., Nat. Phys. **8**, 376 (2012).
[16] L. W. Harriger et al., Phys. Rev. B **84**, 054544 (2011); Phys. Rev. B **86**, 140403(R) (2012).
[17] H. Gretarsson et al., Phys. Rev. Lett. **110**, 047003 (2013).
[18] E. Dagotto, Rev. Mod. Phys. **85** 849 (2013).
[19] J. Zhao, H. Cao, E. Bourret-Courchesne, D. H. Lee, and R. J. Birgenau, Phys. Rev. Lett. **109**, 267003 (2012).
[20] M. Wang et al., Phys. Rev. B **90**, 125148 (2014).
[21] R. Yu, J. X. Zhu, and Q. Si, Phys. Rev. Lett. **106**,

186401 (2011); R. Yu, Q. Si, Phys. Rev. Lett. **110**, 146402 (2013).

[22] M. Y. Wang *et al.*, Nat. Commun. **2**, 580 (2011).

[23] F. Chen *et al.*, Phys. Rev. X **1**, 021020 (2011).

[24] J. W. Lynn *et al.*, J. Research NIST **117**, 61 (2012).

[25] D. X. Yao, and E. W. Carlson, Front. Phys. China **5**, 166 (2010).

[26] T. G. Perring, *et al.*, http://tobyfit.isis.rl.ac.uk.

[27] J. Zhao *et al.*, Phys. Rev. Lett. **112**, 177002 (2014).

[28] R. J. Birgeneau, J. Skalyo, and G. Shirane, Phys. Rev. B **3**, 1736 (1971).

[29] C. Lester *et al.*, Phys. Rev. B **81**, 064505 (2010).

[30] J. Lorenzana, G. Seibold, and R. Coldea, Phys. Rev. B **72**, 224511 (2005).

[31] C. Cao, and J. H. Dai, Phys. Rev. B **83**, 193104 (2011).

[32] X. W. Yan, M. Gao, Z. Y. Lu, and T. Xiang, Phys. Rev. Lett. **106**, 087005 (2011).

[33] Z. P. Yin, K. Haule, and G. Kotliar, Nat. Phys. **10**, 845 (2014).

[34] C. Zhang *et al.*, Phys. Rev. Lett. **112**, 217202 (2014).

[35] A. L. Wysocki, L. D. Belashchenko, and V. P. Antropov, Nat. Phys. **7**, 485 (2011).

[36] R. Yu, Z. Wang, P. Goswami, A. H. Nevidomskyy, Q. Si, and E. Abrahams, Phys. Rev. B **86**, 085148 (2012).

[37] W. Lv, F. Kruger, and P. Phillips, Phys. Rev. B **82**, 045125 (2010).

49

5.3 Outlook

Our work shows clearly that the magnetic excitations in the $Rb_{0.8}Fe_{1.5}S_2$ system are quite similar to those in the pnictides, despite that the electronic properties in the two systems are quite different. As noted in the paper, this finding may have implications for the superconductivity observed in doped materials for each of these families of compounds.

Chapter 6

Copper Substituted Iron Telluride: A Phase Diagram

6.1   Introduction

There are a multitude of interesting reasons to study this phase diagram; I will list a few here.

First, it is interesting from the standpoint of classifying the effects of impurities and magnetic fields on the double-stripe magnetic order; whereas prior to this work most of the detailed thermodynamic data were available only on magnetically ordered states which occur in zero field, and as a function of the level of interstitial iron substitution. Our paper goes into depth on the effects of copper substitution on the structural and magnetic order in terms of the temperature dependences of their scattering strengths, spatial periods, and the magnetic correlation length in zero field and in an applied field; and demonstrates that the magnetic and structural order at 6 percent copper substitution are each sensitive to the applied field.

Second, before our publication, there was ambiguity in a number of issues such as: the solubility limit of copper in this phase; the existence of high-temperature magnetic orders; and a resistive properties which had been described using a number of different models. We observed solubility of copper to 60 percent substitution; did not observe high temperature magnetic order; and provided detailed information about the fitting, or lack-of-fit of the resistance vs. temperature data to several of these models.

This article was accepted for publication as an editor's suggestion: Phys. Rev. B., 91, 224424, 2015

6.2   Paper

P. N. Valdivia,[1] M. G. Kim,[2] T.R. Forrest,[3] Z. Xu,[3] M. Wang,[3] H. Wu,[4,5] L.W. Harringer,[4] E.D. Bourret-Courchesne,[2] and R.J. Birgeneau[1,2,3]

[1]*University of California, Berkeley, Department of Materials Science, Berkeley CA 94720*
[2]*Lawrence Berkeley Laboratory, Materials Science Divison, Berkeley CA 94720*
[3]*University of California, Berkeley, Department of Physics, Berkeley CA 94720*
[4]*NIST Center for Neutron Research, 100 Bureau Drive, Gaithersburg MD 20899*
[5]*University of Maryland, Department of Materials Science and Engineering, College Park MD 20742*

We have studied the structure, magnetic, and transport properties of copper substituted iron telluride. Our results extend the range of copper substitution to 60% substitution per formula unit, which is far beyond previously stated solubility limits. Substitution of copper into antiferromagnetic iron telluride is found to suppress the signatures of the low-temperature transitions in susceptibility and resistance measurements, giving rise to an insulating, spin glass state. Upon increasing the copper substitution from 4% to 6%, short range antiferromagnetic order appears followed by the combined magnetic and structural transition at a lower temperature, although the magnetic order is ultimately not resolution limited with a correlation length of 250 Å in the 6% Cu-substituted sample, in contrast to the magnetic order of the 4% copper substituted sample, which is resolution limited. Upon warming the 6% Cu-substituted sample in the presence of a 5 T magnetic field oriented along the *b* axis, magnetic and structural phase transitions are observed at a temperature much lower than those of the magnetic and structural transitions which occur in zero field. Furthermore, these transitions are absent upon cooling in this field. We discuss the field results in the most general terms possible, including possible random field effects.

1. INTRODUCTION

The nonstoichiometric $Fe_{1+\delta}Te^{1-9}$ and the transition metal substituted $Fe_{1+\delta-x}TM_xTe$ (TM = Ni[10], Cu[11–19], Pd[20]) compounds exhibit intriguing interconnections between structure, magnetism, and electronic properties. The various forms of magnetism in $Fe_{1+\delta-x}TM_xTe$ appear at the antiferromagnetic wave vector $\boldsymbol{Q}_{AFM} = (0.5-\varepsilon, 0, L)$, which is different from the nesting vector[2], although the electron and hole pockets in the Fermi surface can be connected by a nesting vector[1]. Therefore it has been argued that the antiferromagnetic (AFM) order in the family of $Fe_{1+\delta}Te$ compounds arises from localized electrons[21,22]. In $Fe_{1+\delta}Te$ with $\delta \leq 0.09$, the low-temperature antiferromagnetic order is commensurate and forms a double stripe (also referred to as bicollinear) AFM structure with moments pointing along the longer *b* direction; perpendicular to the propagation vector $\boldsymbol{Q}_{AFM} = (0.5-\varepsilon, 0, 0.5)^2$. This bicollinear order is accompanied by a tetragonal-to-monoclinic structural transition[2]. With more excess Fe ($0.09 < \delta < 0.14$), the low-temperature AFM ordering becomes incommensurate (the SDW phase in Rodriguez et. al[2]). This SDW phase can be either long-ranged as in $Fe_{1.09}Te$ or short-ranged as in $Fe_{1.12}Te$ where it coexists with long-range helical order[2]. Finally, for $\delta \geq 0.14$ the magnetism develops a *c*-axis component of the moment, referred to as a helical order, and the magnetic transition is accompanied by an orthorhombic

structural transition[2]. All of these structural and magnetic transitions occur below T = 70 K, and decrease in temperature with increasing δ, down to $T \approx 45$ K in $Fe_{1.14}Te^3$. Both the structural and AFM transitions are first order at $\delta \approx 0.11$ and second order transitions at higher δ, implying a multicritical point[4,5]. A phase transition occurs initially from paramagnetic and tetragonal to incommensurate AFM in either the orthorhombic[5] or monoclinic[6] structure at compositions just above the critical point, then gives way to a transition towards nearly-commensurate order of the bicollinear structure[2,4–6]. It is not clear whether these transitions occur in a single phase[4] or in separate phases that interact[2,5].

In $Fe_{1+\delta-x}TM_xTe$ (TM = Ni[10], Cu[11,12], and Pd[20]) compounds, as transition metal elements are introduced into the system, the structural and AFM transitions are also suppressed as in the $Fe_{1+\delta}Te$ compounds and it was found that a subtle difference in the substitution level produces various interesting structural and magnetic properties. In particular, for $Fe_{1.10}Cu_{0.04}Te$, a first-order magnetic transition occurs at T = 37 K and the AFM ordering is bicollinear at a nearly-commensurate wavevector $\boldsymbol{Q}_{AFM} = (0.494, 0, 0.5)^{12}$. In a compound with slightly more Cu content ($Fe_{1.04}Cu_{0.1}Te$), a short-range AFM ordering was observed at $\boldsymbol{Q}_{AFM} = (0.48, 0, 0.5)$ up to T = 80 K, and a spin-glass-like behavior was also observed in susceptibility at T = 22 K[12]. The

incommensurability ε [defined by (0.5−ε, 0, 0.5)] observed for these copper substituted compounds is much smaller than that of the Q_{AFM} = (0.38, 0, 0.5) in $Fe_{1.12}Te$ and $Fe_{1.14}Te$ compounds[2,7] or Q_{AFM} = (0.34, 0, 0.5) in $Fe_{1.17}Te$[7]. From these results, it seems that Cu substitution may drive the magnetic order from incommensurate SDW or helical towards the commensurate bicollinear AFM order. However, according to one model, the "semiconducting-like" transition in the low temperature resistance data[11] implies the helical magnetic structure in which the spin-gap is closed[5,23] as in $Fe_{1+\delta}Te$ with $\delta \geq 0.14$. Therefore, it is not yet clear how Cu substitution affects the magnetic properties in this family.

Another puzzle in $Fe_{1+\delta-x}Cu_xTe$ is contrasting properties in similar compounds, especially at higher copper compositions. For example, nonstoichiometric $Fe_{0.66}Cu_{0.61}Te$[15] and stoichiometric $Fe_{0.5}Cu_{0.5}Te$[14] compounds exhibit spin density wave transitions (not necessarily of the same type as in Rodriguez et. al[2]) at T = 256 K and 308 K, respectively, although the crystal structures were not reported[14,15]. Another group showed that in $Fe_{0.61}Cu_{0.565}Te$ a tetragonal structure (isostructural to $Fe_{1+\delta}Te$) exists down to T = 4 K while a spin glass transition occurs between T = 70 and 90 K[13] whereas a third group also produced $Fe_{0.61}Cu_{0.565}Te$ and reported that their sample is paramagnetic at all temperatures above T = 10 K[16]. Despite these works at high copper substitution, it has also been reported that copper is not miscible in the $Fe_{1+\delta-x}Cu_xTe$ structure with $x \geq 0.2$ or 0.3[12].

The transport properties of $Fe_{1+\delta-x}Cu_xTe$ compounds are also intriguing. For instance, the resistance exhibits a change in behavior (a "metal-to-semiconductor" transition[5]) in $Fe_{1+\delta-x}Cu_xTe$[11]. The metallic behavior was previously observed in $Fe_{1+\delta}Te$ with $\delta \approx 0.06$[5] and associated with the existence of a spin gap[5,23]. The spin gap is closed when the magnetic structure develops c-axis component of the moment and forms a helical order in $\delta \approx 0.14$[5,23]. Alternatively, a DFT calculation suggests Anderson localization for the origin of the "metal-to-semiconductor" transition which occurs in $Fe_{1-x}Cu_xSe$ due to local electronic disorder introduced by filled d^{10} shells of copper[24]. The variable range hopping model, which can signify Anderson localization[25] is successfully applied in $Fe_{1-x}Cu_xSe$[26], $Fe_{0.5}Cu_{0.5}Te$[17] and $Fe_{0.98-z}Cu_zSe_{0.5}Te_{0.5}$[27], z = 0.02 and 0.1. However, other studies have suggested that $Fe_{0.5}Cu_{0.5}Te$ is a zero bandgap semiconductor, wherein the resistance scales as a power law in temperature[16,18] reflecting intrinsic power law behaviors in the carrier concentration, and that the exponent's value indicates diffusive transport due to formation of spin polarons[16,28,29].

To shed light on the complex physical properties in $Fe_{1+\delta-x}Cu_xTe$, we present synthesis of a series of single crystals of $Fe_{1+\delta-x}Cu_xTe$ compounds and their resistance and
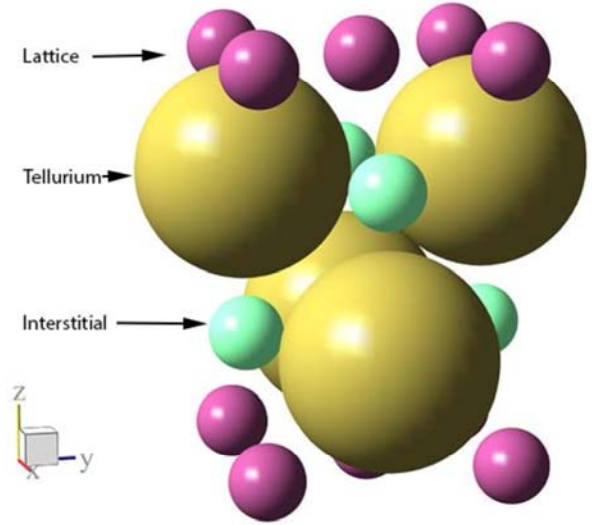
FIG. 1 The crystal structure (visualized in origin choice 1) of $Fe_{1+\delta-x}Cu_xTe$ compounds. The interstitial sites are only slightly occupied by the amount δ as described in the text. The interstitial metal and tellurium atoms are both situated on (2c) sites, which have a free parameter as the height from the metallic lattice plane.

susceptibility. We also report the structural and antiferromagnetic properties in several compounds studied by x-ray powder diffraction, neutron powder diffraction and neutron single crystal diffraction measurements. We find that copper can replace iron up to 60% per formula unit, which is far beyond previously assumed solubility limits[12] in the structure (Fig. 1). We show that the resistance data cannot be fit to the variable range hopping model at any composition while the zero bandgap model can fit our data for 52% and 57% Cu substitutions. Our neutron measurements show a single first order magneto-structural transition in 4% Cu substitution, and two separated structural and/or magnetic transitions in 6% Cu substitution. We demonstrate that the AFM ordering is long-ranged and commensurate in 4% Cu substitution and short-ranged incommensurate with a spin correlation length of 250 Å in 6% Cu substitution. We also find that upon applying an external magnetic field, additional structural and magnetic transitions appear at lower temperature. We discuss the nature of the transitions in field, which might result from random field effects.

2. EXPERIMENTAL METHODS

We synthesized $Fe_{1+\delta-x}Cu_xTe$ (FCT) single crystals using a modified Bridgman growth technique that utilizes the natural temperature gradients in a horizontal furnace. Pieces of elemental iron (4N), tellurium shot (4N), and pieces cut

from copper sheet (8N), were combined in an Argon filled glovebox, and reacted in doubly-sealed quartz ampoules using a two-step procedure. The first step was a pre-melting reaction intended to homogenize the reactants following that previously used to synthesize other iron-chalcogenides[30]. The reacted material was then brought back into the glovebox, where the quartz was broken and the material was ground into a fine powder and loaded into clean quartz ampoules. The second step used a higher melting temperature than that used in the previous studies[12,30] in order to ensure homogeneity of the melt[31]. After heating to 625 °C at a rate of 0.5 °C/min and holding for 12 hours, then heating to 975 °C at 0.5 °C/min and holding for 30 hours, the tubes were heated to 1075 °C at a rate of 0.5 °C/min and held for 30 hours. Then the tubes were cooled first to 650 °C (3 °C/hr) followed by 415 °C (0.5 °C/min), held for 24 hours, and finally cooled to room temperature at a rate of 0.5 °C/min.

The synthesis resulted in large single crystalline boules at all compositions studied, except in the sample of nominal copper free composition $Fe_{1.08}Te$, which appears noncrystalline and produced a multiphase product as observed by x-ray powder diffraction. Crystals extracted from the boules had a reflective silver luster, in contrast with the gold color reported at $x \approx 0.5$ in some previous studies[18,19]. All crystals became less lustrous if left in air at room temperature over the time scale of several weeks; however, the samples were always stored in a glovebox until it became necessary to remove them for measurements.

For elemental analysis, Energy Dispersive X-ray Spectroscopy (EDX) was performed on the **ab**-plane of single crystal samples using a Leo 430 Scanning Electron Microscope. Measurements were performed with over 50,000 points collected over an area of at least 0.1 mm^2. The compositions were extracted by integrating the Cu-Kα, Cu-Kβ, Fe-Kα, Fe-Kβ, Te-Lα, Te-Lβ, and Te-Lγ peak profiles across the entire scanned area. From these ratios we obtained $x_{EDX} = Cu/Te$ and $\delta_{EDX} = (Cu+Fe)/Te - 1$. Three samples were measured from each growth batch, and when the nominal concentration of copper $x_{nom} \geq 0.3$, six samples were measured, as further explained in the results section. The errors in the values x_{EDX} and δ_{EDX}, estimated by the counting statistics of each measurement, were less than 1% for all compounds.

Powder diffraction data were collected at room temperature with a PANalytical X'Pert Pro diffractometer using Co-Kα_1 radiation. The lattice parameters were obtained by refinement using LaB$_6$ (NIST SRM 660b) as a positional calibrant.

For structural refinement beyond the lattice parameters, and for an additional check of the phase purity, neutron powder diffraction (NPD) measurements were performed on two samples with the BT-1 diffractometer at the NIST Center for Neutron Research. The refinements of the crystal structures were performed with GSAS+EXPGUI[32].

Susceptibility measurements were primarily performed using a Quantum Design Physical Properties Measurement System (PPMS), while a Magnetic Properties Measurement System (MPMS) was used to check cooling/warming hysteresis of the AFM transitions of the samples with $x_{EDX} \leq 0.06$. Both zero-field-cooled and field-cooled measurements were performed between 2 K and 350 K. Low field measurements were obtained in a field of $\mu_0 H = 0.1$ T and high field measurements were obtained at 5 T. In each case the field was aligned parallel to the **ab**-plane. For the PPMS measurements, cooling from high temperature was performed in a two-step process involving 2 hours dwell time upon cooling to 50 K and to 2 K, in order to ensure a uniform temperature environment for the measurement.

In order to determine the low-temperature magnetic and structural properties of $x_{EDX} = 0.04$ and $x_{EDX} = 0.06$ compounds, elastic neutron diffraction was performed on single crystals of these compositions at the NG-5 triple axis beamline (SPINS) at the NIST Center for Neutron Research, using $\lambda = 4.09$ Å neutrons. A cooled beryllium filter was used to remove the $\lambda/2$ harmonic. The masses of these samples were 0.498 g for $x_{EDX} = 0.04$ and 0.488 g for $x_{EDX} = 0.06$. Measurements for the $x_{EDX} = 0.04$ sample were performed in a sample can which was loaded into a closed cycle refrigerator, and measurements were taken between 6.5 and 70 K. For the $x_{EDX} = 0.06$ sample, the sample was loaded into a displex/cryostat and all of the measurements, including those in zero field, were performed with a 7 T vertical field magnet installed, which reduced the incident neutron intensity by a factor of roughly ten; measurements in this environment were taken between 2 K and 80 K.

Resistance measurements were also performed with a Quantum Design PPMS. As silver paint contacts often fail for the iron-chalcogenides[33], low-resistance contacts were fabricated by sputtering 500 Å Ti/8000 Å Au pads on the sample and gold wires were bonded to the contacts using silver paint. The measurements were performed between 2 and 300 K.

3. RESULTS AND DISCUSSION

A. Stoichiometry

Figure 2a shows the relation between the actual Cu concentration (x_{EDX}) and the starting (nominal) concentration (x_{nom}) for each growth batch of $Fe_{1+\delta-x}Cu_xTe$, with separate labels for growth batches which were initially distinguished by different nominal iron content: $\delta_{nom} = 0.08$ and 0.18. When $x_{nom} \leq 0.2$, the actual concentration tracks the nominal concentration for individual pieces and for the average, while for concentrations of $x_{nom} \geq 0.3$, a range of
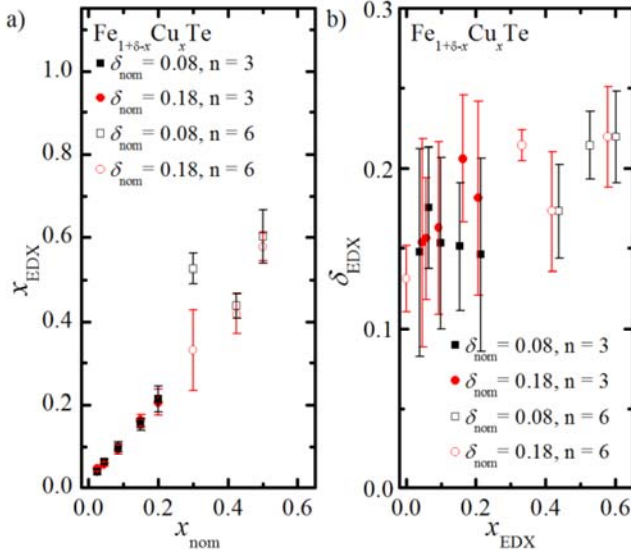
FIG. 2 EDX-mapping data measured for the different growth batches. Average concentrations are determined with three randomly selected pieces of crystal ($n = 3$) for nominal concentration $x_{nom} \leq 0.2$, and six pieces of crystal ($n = 6$) for $x_{nom} \geq 0.3$. a) Average EDX copper concentration x_{EDX} = Cu/Te as a function of x_{nom}. b) Average excess metal ratio δ_{EDX} = [(Cu+Fe)/Te]−1 versus average copper concentrations x_{EDX}. Error bars indicate the standard deviation of the two sets of growth batches at low x_{nom} and single growth batches at high x_{nom}, so that the number of samples in each set is 6.

concentrations was produced with a standard deviation of $\sigma(x_{EDX}) \approx 0.1$ for each growth batch; furthermore x_{EDX} is much greater than x_{nom} in the three growth batches which ended up having the highest actual compositions. Thus we measured an additional three samples for each growth batch with $x_{nom} \geq 0.3$ to investigate the homogeneity of the boules along their length, but did not observe any consistent segregation characteristic. We also measured six samples for $\delta = 0.18$, $x_{EDX} = 0$ as the $\delta = 0.08$ product was multiphase. Within the samples with $x_{nom} \geq 0.3$, the EDX-measured compositions were consistent across the samples which were ~10 millimeters wide, and when comparing the front and back surfaces of samples 2 to 3 millimeters thick. However, since a spread of compositions exists within the boules for $x_{nom} \geq 0.3$, the actual compositions (x_{EDX}) were measured on the same crystals for which we measured powder diffraction, susceptibility, and resistance for these samples (when $x_{nom} \geq 0.3$). Therefore, we will use the variable x_{EDX} throughout the paper to denote the average of all EDX measurements when $x_{nom} \leq 0.2$ and for the concentration of the piece of crystal measured in the physical property measurement specified when $x_{nom} \geq 0.3$, except in this section (correspondingly, Fig. 2) and in the section on neutron powder diffraction

measurements (Fig. 3) where it represents the average of all samples measured.

Figure 2b shows a plot of the averaged δ_{EDX} vs. x_{EDX} for each growth batch. A positive correlation between δ_{EDX} and x_{EDX} is evident. This can be interpreted in at least three ways: (i) the total amount of metal in the phase increases with copper substitution (ii) the occupancy of the tellurium site decreases with copper substitution or (iii) additional impurity phases with a higher (Fe+Cu)/Te ratio are formed at high copper substitution; any combination of the above cases may also occur. We shall show evidence in the neutron powder diffraction section that the first mechanism (i) likely does not contribute to this trend. Comparing the low-temperature resistive properties observed in our copper-free samples of $Fe_{1+\delta}Te$ with previous reports[5] it is highly likely that $\delta \leq 0.11$; using reference data obtained for magnetic susceptibility of crystals with various composition in $Fe_{1+\delta}Te$, we believe that we have obtained $Fe_{1.07}Te$[3], whereas our EDX results give $\delta_{EDX} = 0.13$. We shall discuss evidences of slight amounts of impurity phases in the results of susceptibility measurements and in the section on neutron powder diffraction. For the EDX measurements, we note that the scatter in measured values of δ_{EDX} between growth batches and for different samples within a growth batch is too high to characterize precisely the effect of changing the starting composition δ_{nom}. We attempted to look for correlations of δ_{EDX} with other measured physical properties: lattice parameters, magnetic properties, and resistance; however we could not distinguish any correlations in the data.

B. Neutron Powder Diffraction

Figure 3 shows the neutron powder diffraction (NPD) data measured on two compositions at room temperature, x_{EDX} = 0.10 and 0.60; x_{EDX} = 0.60 represents the high-substitution limit. For x_{EDX} = 0.60 we measured data with λ = 1.5403 Å, while for x_{EDX} = 0.10 we additionally collected data with λ = 1.1975 Å in order to optimize the data for site occupancy refinement; the data using neutrons with wavelength λ = 1.1975 Å are shown for x_{EDX} = 0.10 in Fig. 3 to highlight the angular range measured, although the fitted parameters were obtained by co-refinement of the datasets from both wavelengths. The scale factor, background function, profile parameters, atomic coordinates, thermal factors, and site occupancies were refined. Exemplary fits to the data are shown with the solid black lines. Anisotropic broadening profile terms were required to fit all the peak widths simultaneously; adding an additional phase of the same structure to the single phase with anisotropic broadening hardly improves the fits, demonstrating a lack of phase separation and solubility of copper in each of these compounds. For the refinement starting models, we
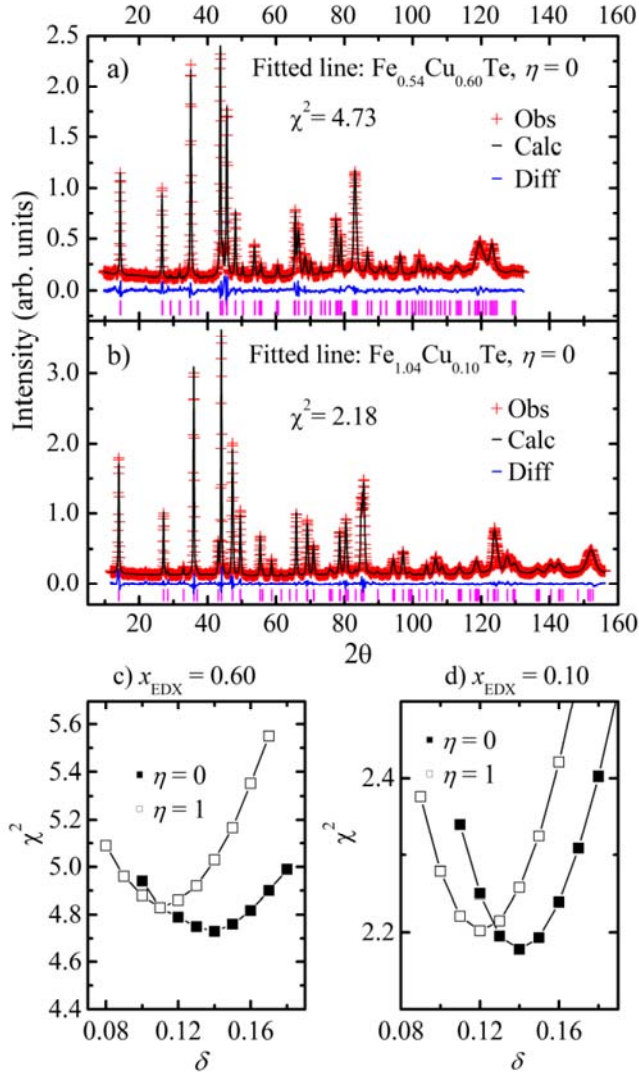
FIG. 3 Neutron powder diffractogram of a) $x_{EDX} = 0.60$ and b) $x_{EDX} = 0.10$ compounds. The goodness-of-fit χ^2 versus δ and η for c) $x_{EDX} = 0.60$ and d) $x_{EDX} = 0.10$ compounds.

constrained the total amounts of metal to the values measured by EDX, while the range of values used for thermal factors and atomic coordinates spanned those in previous NPD and x-ray reports[2,8,13,34,35]. Refining the copper content had little effect on χ^2 and did not correlate with other parameters, thus we kept it fixed to x_{EDX}. Refinements of the (2a) occupancy with various starting models consistently resulted in a fully occupied (2a) site. The two remaining site occupancy parameters may be represented by the variables (δ, η). As in the EDX measurement, δ denotes the excess metal content that is equal to the total occupancy of the (2c) metal site divided by the tellurium occupancy. This gives the (2c) occupancy in these refinements. Given the interdependence of occupancy

parameters in the refinement, it was necessary to fix the tellurium occupancy to 1. The inversion parameter η, describes the distribution of iron and copper over the two sites by the formula:

$$\eta = \begin{cases} 1 - \dfrac{O(Cu, 2c)}{x_{EDX}} & \text{when } x_{EDX} \leq \delta \\[2ex] 1 - \dfrac{O(Cu, 2c)}{\delta} & \text{when } x_{EDX} > \delta \end{cases} \quad (1)$$

with $O(Cu, 2c)$ being the copper occupancy on the (2c) metal site. Thus for $\eta = 0$, iron has maximum preference to be placed into the (2a) site; since our refinements suggest the (2a) site is fully occupied, we simply put as many iron atoms on (2a) as possible. For $\eta = 1$ copper is placed on the (2a) site only, with the remainder of the (2a) site and the (2c) site filled by iron. Increasing η shifts the best fits of δ to lower values and produces only marginal changes in χ^2; thus we cannot determine η but instead examine its effects on the range of best-fit values of δ. We constrained the height variables of interstitial metals: $Z_{Fe,2c} = Z_{Cu,2c} = Z_{int}$, and used one thermal factor for tellurium and another for the metals; using more thermal factors only marginally improved the fits. Since we have fixed the copper and tellurium contents, changing $\delta = (Fe+Cu)/Te$ modifies the total iron content in the refinement model.

Figures 3c and 3d show the results of refinements performed while fixing values of the site occupancy parameters (δ, η), while allowing all other parameters to vary freely. Fixing these parameters during refinement allows us to investigate cleanly the effects of each parameter on the fit. The solutions consistently lie on parabolae in the goodness-of-fit parameter χ^2 vs. δ (Figs. 3c-d); when the site occupancies are refined starting with the values at the minima of the parabolae, the refinements are found to be stable. As shown in Fig. 3c, the optimal occupancy of the (2c) site in the $x_{EDX} = 0.10$ sample is 0.12 Fe ($\eta = 1$), or 0.10 Cu and 0.04 Fe ($\eta = 0$). For the $x_{EDX} = 0.60$ sample, the optimal (2c) occupancies are 0.11 Fe, or 0.14 Cu. Comparison of the range of fitting values for these two samples suggests that the (2c) site occupancy does not change significantly between $0.10 \leq x_{EDX} \leq 0.60$. Since all possible values of η produce solutions between the ranges of δ obtained at the endpoints $\eta = 0$ and $\eta = 1$, these results suggest that the correlation between δ_{EDX} and x_{EDX} described in the previous section does not likely arise from an increase in the total metal content in the phase. The refined parameters for each sample are summarized in Table I, where the errors cover the range of values obtained for the best fit solutions with $\eta = 0$ and 1.

Very weak reflections with intensity at roughly 1% of that of the maximum reflection of the main phase were observed in each diffractogram; at this intensity they are almost indistinguishable from the background. 13 such

features were observed for the $x_{EDX} = 0.60$ sample while only 8 were observed for the $x_{EDX} = 0.10$ data at $|Q| < 5.72$ Å^{-1}, none of which could be conclusively indexed to known phases in the open crystallography database[36]. Therefore, the large values we observe for δ_{EDX} may be partly attributable to the formation of very slight amounts of impurity phases. Due to the limitations of our experiments, we cannot determine whether tellurium vacancies contribute to the large values of δ_{EDX} at high values of x_{EDX} at present.

C. Lattice Parameters

TABLE I. Refined parameters from the neutron powder diffraction data (at room temperature). The atomic positions are provided in origin choice 2. Standard deviations are shown for the lattice parameters, which were consistent between fits, while the average and difference of refined values for the two site occupancy models are shown as the values before and within the parentheses for the other structural parameters.

Sample	$x_{EDX} = 0.10$	$x_{EDX} = 0.60$
c (Å)	6.2825(1)	6.1090(3)
a (Å)	3.8377(1)	3.9683(1)
δ_{NPD}	0.13(1)	0.13(2)
$U_{iso\,(Te)}$ (Å^2)	0.0161(3)	0.0218(1)
$U_{iso\,(Fe/Cu)}$ (Å^2)	0.0146(1)	0.0169(3)
Z_{Te}	0.2808(1)	0.2770(1)
Z_{int}	0.7074(1)	0.6984(6)
χ^2	2.19(1)	4.77(4)
wR_p	0.0579(2)	0.0644(3)
R_p	0.0464(2)	0.0502(3)

Figure 4 shows the room temperature lattice parameters of FCT as a function of copper concentration. We selected small pieces of crystal to grind for XRD, confirming their homogeneity by EDX measurements on both faces of the crystals. After grinding these crystals for the x-ray powder diffraction measurements, a small amount of NIST SRM 660b (LaB$_6$ powder) was mixed with the sample as a positional calibrant. The error in refined lattice parameters for each compound is smaller than 0.01 Å. Hence, the uncertainty in the refined lattice parameter is much smaller than the uncertainty in the concentration in the average copper content of the sample with respect to the EDX measurement, which was performed prior to grinding and therefore might only reflect the surface regions of the samples. We observe close agreement between the lattice parameters obtained by refinement of x-ray powder
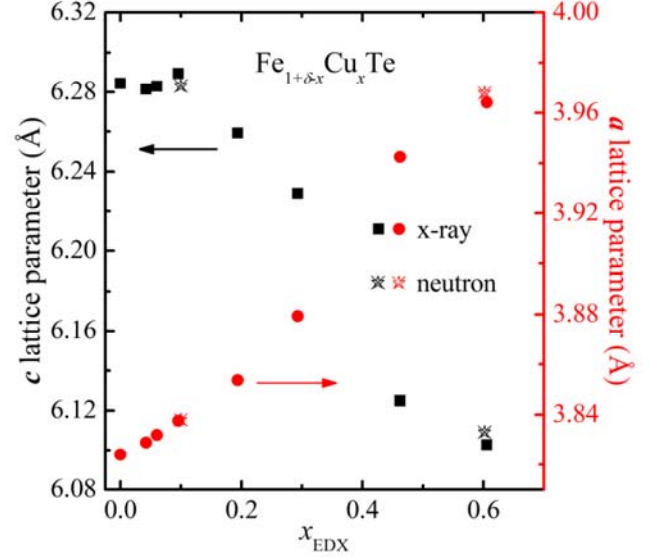

FIG. 4 Lattice parameters a and c as a function of Cu concentration x_{EDX}. See the text for details.

diffraction compared with those for the two samples refined by neutron powder diffraction.

While the c lattice parameter does not vary much for $x_{EDX} \leq 0.1$, the a lattice parameter shows a slight increase. For $x_{EDX} \geq 0.1$, the c lattice parameter contracts, and the a lattice parameter expands gradually with substitution, in agreement with the trends observed previously[11,12]. However, the rate of change of lattice parameters with substitution in the region $x_{EDX} \geq 0.1$ is lower than that in the previous phase diagram[11]. The lattice parameters obtained in the previous phase diagram at $x = 0.3$[11] are nearly equal to those we observe at $x_{EDX} = 0.46$. The lattice parameters we obtain in the region $0.46 \leq x_{EDX} \leq 0.60$ are close to values previously published for compounds with $x = 0.5$, 0.55 and 0.57[13,16,19]. One possibility for the discrepancies between our lattice parameters and those of the previous phase diagram that is easily ruled out is that the values of x_{EDX} in the present study overcount the copper content due to the presence of impurity phases. Impurity phases of Cu, Cu$_2$O, CuO, or Cu$_{1.4}$Te would be expected to produce peaks of nearly-equal intensity (within a factor of 2) in the neutron powder diffractograms as those of the peaks from the main phase, if the mass fraction of each is the same. Therefore, given the lack of high intensity impurity peaks in the NPD measurements, we suggest that any impurity phase containing copper must contain a total mass of less than 1-2% of that of the main phase. Even if copper was distributed among several impurity phases, this could not account for the differences observed between the present phase diagram and the previous one[11]. Therefore, if both measurements are correct, the differences must correspond to details of the main phase
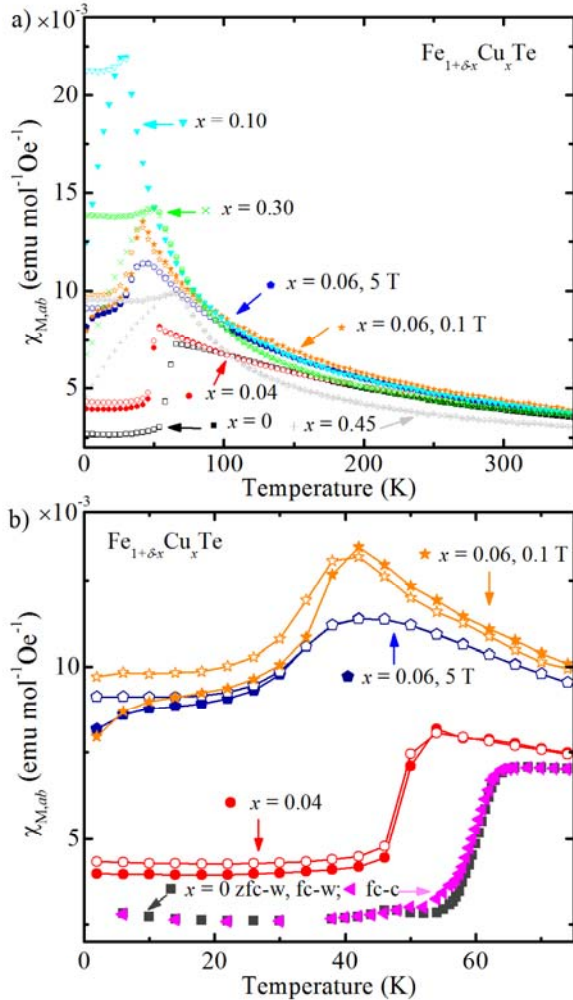
FIG. 5 a) Molar susceptibilities of a series of $Fe_{1+\delta-x}Cu_xTe$ compounds measured in zero-field-cooled (ZFC) and field-cooled (FC) measurements with applied fields of $\mu_0H = 5T$ for $x_{EDX} \leq 0.06$ and 0.1T for $x_{EDX} \geq 0.06$. ZFC and FC are measured on warming. The field was applied in plane ($\mu_0H \parallel ab$). The closed symbols are ZFC while the open symbols are FC. b) The same data, plotted in a limited temperature range $T \leq 75K$ for $0 \leq x_{EDX} \leq 0.06$; and also showing field-cooled cooling (fc-c). Please note 1 emu / (mol Oe) = $4\pi \times 10^{-6}$ m^3/mol.

such as site occupancies: vacancies, excess metal δ, or η, which implies that one or more of these parameters may be sensitive to the growth conditions.

D. Susceptibility

Figure 5a shows the susceptibility of FCT as a function of copper concentration with the magnetic field applied parallel to the *ab*-plane. Sudden changes in the susceptibility χ occur

for all samples at $T \leq 66$ K indicating the occurrence of magnetic transitions. None of our samples exhibit paramagnetism down to 10 K in contrast to the previous study with nominal concentration $x = 0.5$ and $\delta = 0$[16], nor did we observe signatures of a transition at $T = 256\text{-}308$ K which was reported to occur in powderized crystals of nominal concentration $x = 0.5$ and $\delta = 0$ by Mössbauer and susceptibility measurements in well annealed samples[14,15]. Our samples had higher nominal iron compositions and different preparation procedures than these samples; this implies that the details of the sample growth and heat treatment may be important to the properties. For samples with $x_{EDX} \geq 0.10$ the zero field cooled (ZFC) susceptibility decreases with decreasing temperature below the maximum in the susceptibility (which we label as the spin-glass transition temperature, T_G) while in field-cooled (FC) measurements, the susceptibility is constant and approximately equal to the maximum value below T_G. These two characteristics are consistent with behavior expected for a spin-glass transition[37] and also consistent with the previous reports at 10% copper substitution[11]. However, another report claimed that this compound exhibits a transition to a short-range antiferromagnetic state while they observed the same feature in susceptibility measurements[12]. The divergence of dχ/dT at the transition temperature increases with increasing copper substitution up to $x_{EDX} = 0.10$, which might be understood in the antiferromagnetic state as the random field effect of copper[38] which will be discussed in detail later.

The data shown in Fig. 5 were measured at $\mu_0H = 5$T for $x_{EDX} \leq 0.06$ and at $\mu_0H = 0.1$T for $x_{EDX} \geq 0.06$ since the signal from what is presumably slight amounts of a ferrimagnetic Fe_3O_4 impurity phase obscures the signal from the main phase in $\mu_0H = 0.1$T for $x_{EDX} \leq 0.04$; and in addition, no signal from Fe_3O_4 is observed for $x_{EDX} \geq 0.06$, but higher measuring fields can change the shape of the susceptibility transitions in these samples (not shown) which complicates the analysis. In order to compare the susceptibility at low copper substitution to that at high copper substitution, χ was measured for the $x_{EDX} = 0.06$ samples in $\mu_0H = 0.1$T and 5T. Although indicating a slight degree of magnetic saturation, the susceptibility data measured are nearly in agreement for the two different applied fields (Fig. 5b). A significant difference is that a sharp cusp (the temperature at which the maximum in the susceptibility occurs) appears at $T_{cusp} = 42$ K in $\mu_0H = 0.1$ T and it is replaced by a broad maximum in $\mu_0H = 5$ T.

As shown in Fig. 5b, the zero-field-cooled and field cooled susceptibilities measured on warming in field, χ_{ZFC} and χ_{FC}, show a thermal hysteresis in $x_{EDX} = 0$ with respect to the FC cooling curve ($T_N^\chi = 63.1$ K in cooling and 63.5 K in warming determined from the intersection of linear fits to the susceptibility data above and below the maximum value)
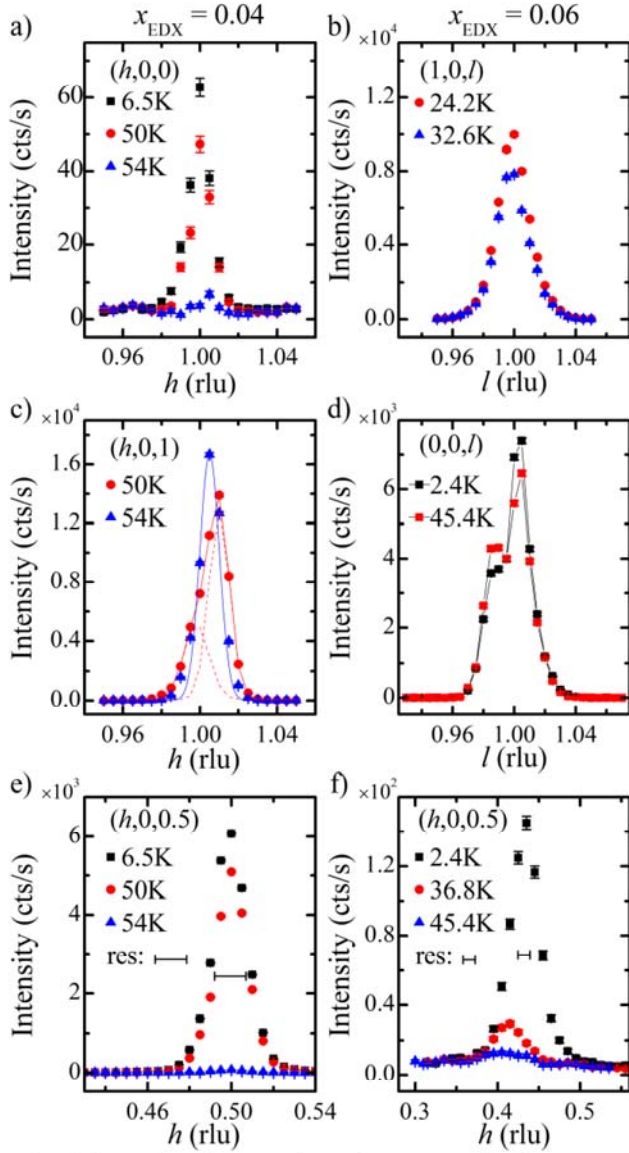
FIG. 6 Overview *Q* scans through structural and magnetic Bragg positions plotted with statistical error. For $x_{EDX} = 0.04$, structural a) (1, 0, 0) and c) (1, 0, 1) and e) magnetic (0.5, 0, 0.5) peaks were measured at several temperatures. For $x_{EDX} = 0.06$, structural b) (1, 0, 1) and d) (0, 0, 1) and f) magnetic (0.5−ε, 0, 0.5) peaks were measured at several temperatures. Scans only at selected temperatures are shown here. The two line shapes drawn with dashed lines in panel c) denote two peak fitting. The instrumental resolution is denoted with bars in e) and f).

which is a signature of a first-order transition. Both ZFC and FC show a single feature with maximum susceptibility at T_N^χ = 54 K for x_{EDX} = 0.04 whereas x_{EDX} = 0.06 shows an additional feature below T_{cusp} which is most easily visible at

temperatures below *T* = 10 K. Below this feature, ZFC and FC curves separate further with cooling. Such a two-featured $\chi(T)$ characteristic was consistently observed in at least four samples measured for each growth batch with x_{EDX} = 0.06. Unlike χ_{FC} in higher copper substituted compounds which remain constant below T_G, χ_{FC} in x_{EDX} = 0.06 is reduced below T_{cusp}, which indicates that this transition may be distinct from the spin-glass transitions. A similar feature was observed in $Fe_{1.13}Te$ which was explained as originating from non-bullk superconductivity[39]. It is possible that our sample also exhibits non-bulk superconductivity although we did not observe any feature in the resistance data at this temperature. The lower temperature transition in x_{EDX} = 0.06 is quite subtle, and its transition temperature is difficult to determine with these data. We will discuss a clear transition observed in neutron scattering measurements in the next section.

Comparing χ_{ZFC} to χ_{FC} data, the susceptibility below and above the magnetic transition are lying on top of each other for both measurements in x_{EDX} = 0 (Fig. 5b). However, such measurements showed that χ_{FC}-χ_{ZFC} > 0 at all temperatures below the maximum in χ for x_{EDX} = 0.04 and 0.06 (Fig. 5b). χ_{FC}-χ_{ZFC} > 0 is reproduced upon a subsequent ZFC procedure. Such behavior might occur if the antiferromagnetic domains form with moments preferably perpendicular to the field when field cooled, resulting in different magnitudes of χ_a and χ_b as expected from the magnetic symmetry of $Fe_{1+\delta}Te^2$ or if the sample moves due to the applied field during measurements. We found it notable that χ_{FC}-χ_{ZFC} is nonzero for $\mu_0 H$ = 0.1T in x_{EDX} = 0.06 while χ_{FC}-χ_{ZFC} = 0 for $\mu_0 H$ = 5T in x_{EDX} = 0. We observed some sample-to-sample variation in the magnitude of χ which was less than 25% from the reported values and this might be due to sample shape effects.

Close inspection shows that the ZFC and FC procedures result in slightly different susceptibilities at temperatures above T_{cusp} in x_{EDX} = 0.06 in a field of 0.1T. However, this difference is temperature-independent to *T* = 350 K (not shown), and is not observed in $\mu_0 H$ = 5 T (Fig. 5b). We believe that it is likely due to the existence of slight amounts of an impurity phase, with a negligible contribution to the susceptibility in the higher field that saturates the impurity susceptibility. We also note the observation of signals at *T* = 340 K in some samples with $x_{EDX} \geq 0.15$ (not shown) which we also believe to be due to slight amounts of an unidentified impurity phase.

E. Single Crystal Neutron Scattering

In order to determine the properties of the low-temperature phases in the x_{EDX} = 0.04 and x_{EDX} = 0.06 samples, we monitored signals at several structural and magnetic Bragg peak positions at different temperatures using the single
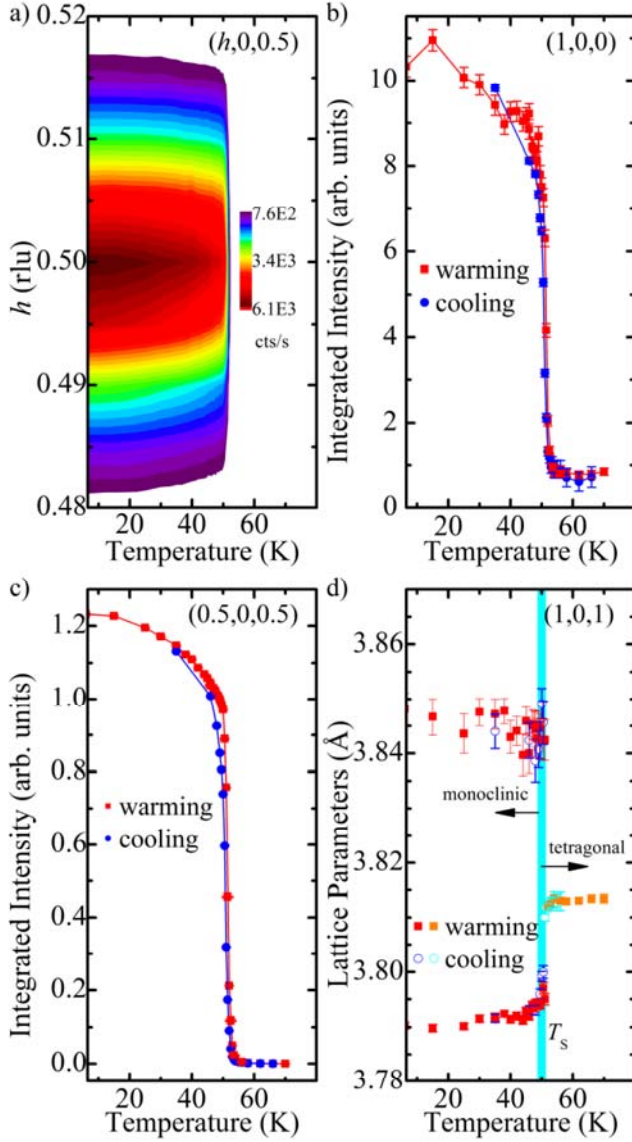
FIG. 7 The AFM and structural order parameters for the x_{EDX} = 0.04 compound plotted with statistical error. a) Contour map of magnetic scattering around (0.5, 0, 0.5) Bragg peak, measured on warming. b) Integrated intensity of (1, 0, 0) Bragg peak as a structural order parameter. Note that a small background which is temperature-independent exists between 54 and 70 K above T_N. c) The AFM order parameter obtained from the integrated intensity at (0.5, 0, 0.5) d) Temperature dependent lattice parameters extracted from fits to [h, 0, 1] scans show the tetragonal-to-monoclinic transition.

crystal neutron diffraction technique and summarize our results in Figs. 6 – 10.

In Figure 6, we show overview scans for structural (h, 0, l) (h = l = integer) peaks and magnetic (h, 0, 0.5) peaks at selected temperatures. For the x_{EDX} = 0.04 sample we monitored structural Bragg peaks at Q = (1, 0, 0) and (1, 0, 1) (Figs. 6a and 6c). The observed signals at the (1, 0, 0) Bragg peak position indicate that the low temperature phase in x_{EDX} = 0.04 is in monoclinic symmetry since the (1, 0, 0) is disallowed within the known tetragonal and orthorhombic symmetries of $Fe_{1+\delta}Te$ but allowed in the monoclinic symmetry previously reported for $Fe_{1+\delta}Te$[6]. For further investigation of the low temperature structure in x_{EDX} = 0.04, we measured the structural (1, 0, 1) peak and observed that at T = 50 K (below the transition) the peak can be fitted with two Gaussian line shapes in the [h, 0, 0] scan (Fig. 6c) indicating two different in-plane lattice parameters.

For the x_{EDX} = 0.06 sample, we did not observe any signal at (1, 0, 0) at the lowest temperature in our measurement (T = 2.5 K) and observed a single peak at the (1, 0, 1) Bragg peak position (Fig. 6b). Neither peak splitting nor broadening of the peak was observed at Q = (1, 0, 1). However, we observed an increase of intensity of (1, 0, 1) Bragg peak as the temperature was lowered. This increase in intensity is likely due to extinction release[40,41] caused by a symmetry lowering structural transition. As any changes in the (0, 0, 1) Bragg peak are negligible in temperature (Fig. 6d) the transition likely involves in-plane structural parameters only. We note that the determination of the exact low temperature structure for x_{EDX} = 0.06 is beyond the scope of our current paper. It should be noted that the (0, 0, 1) scan contains two peaks (Fig. 6d) indicating a possible phase separation with two different c-axis lattice parameters, which was not detected in x-ray powder diffraction measurements.

We also measured signals at Q_{AFM} = (h, 0, 0.5) and show [h, 0, 0] scans of x_{EDX} = 0.04 and 0.06 samples in Figs. 6e and 6f, respectively. We observed a sharp resolution-limited peak at Q_{AFM} = (0.5, 0, 0.5) in x_{EDX} = 0.04, which is commensurate and consistent with the bicollinear AFM structure[2]. In x_{EDX} = 0.06, the magnetic peak is markedly broader than the instrumental resolution, and appears at an incommensurate position (h = 0.433±0.002 at T = 2.5 K); only weak intensity which could not be properly fitted to a peak is observed at T = 45 K as shown in Fig. 6f.

For further investigations on the structural and magnetic phase transitions in these materials, we measured the above-mentioned structural and magnetic Bragg peaks as a function of temperature and show the structural and magnetic order parameters in Fig. 7 for x_{EDX} = 0.04 and Fig. 9 for x_{EDX} = 0.06. Figure 7a shows a temperature dependent contour map of the intensity around the (0.5, 0, 0.5) magnetic peak in x_{EDX} = 0.04. Figure 7c shows a magnetic order parameter obtained by integrating the intensities of the (0.5, 0, 0.5)
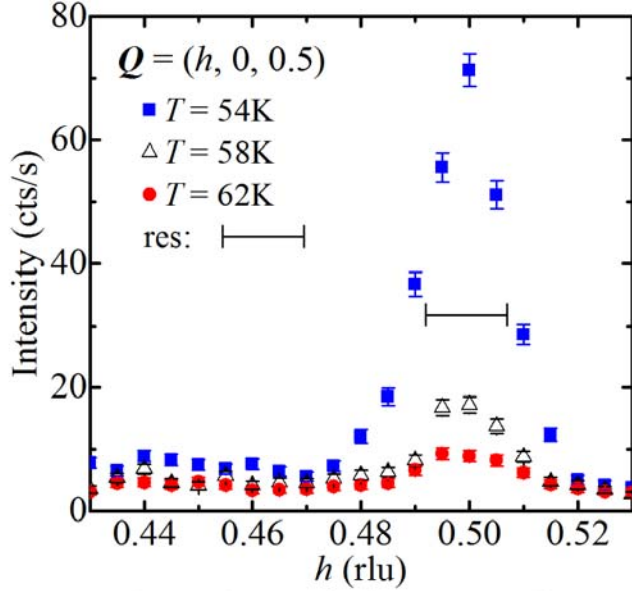
FIG. 8 Weak magnetic scattering in x_{EDX} = 0.04 (above T_N) plotted with statistical error magnetic Bragg peak.

Measurements during cooling and warming exhibit thermal hysteresis; T_N = 50.75 K during cooling and 51.5 K upon warming. The observed transition temperature by neutron measurements is consistent with $T_N\chi$. We conclude from our neutron measurements that the AFM transition is first order in x_{EDX} = 0.04. A close inspection reveals a weak, but resolution limited scattering that remains at the commensurate position above T_N (up to 62 K), with intensity 2-3 orders of magnitude lower than that at temperatures just below T_N (Fig. 8). The existence of weak scattering is in agreement with previous studies of $Fe_{1+\delta}Te$, and lightly copper-substituted $Fe_{1+\delta}Te$, although such scattering has been reported as incommensurate and short-range[2,12], in contrast to the magnetism in the present sample which is commensurate and resolution limited at all temperatures measured (Fig 8).

The structural order parameters at Q = (1, 0, 0) and (1, 0, 1) for x_{EDX} = 0.04 were also investigated. Since the (1, 0, 0) peak is disallowed in the high temperature tetragonal structure, the occurrence of signals at Q = (1, 0, 0) is a good structural order parameter while the lattice parameter splitting obtained from two-peak fit in the (1, 0, 1) peak also well presents a structural order parameter (Figs. 7b and 7d, respectively). We observe that the structural transition occurs at the same temperature as T_N during cooling and warming, which exhibits the same thermal hysteresis (T_S = 50.75 K and 51.5 K). Hence, we conclude that the AFM transition and the structural transition occurs simultaneously and as first order transitions in x_{EDX} = 0.04.
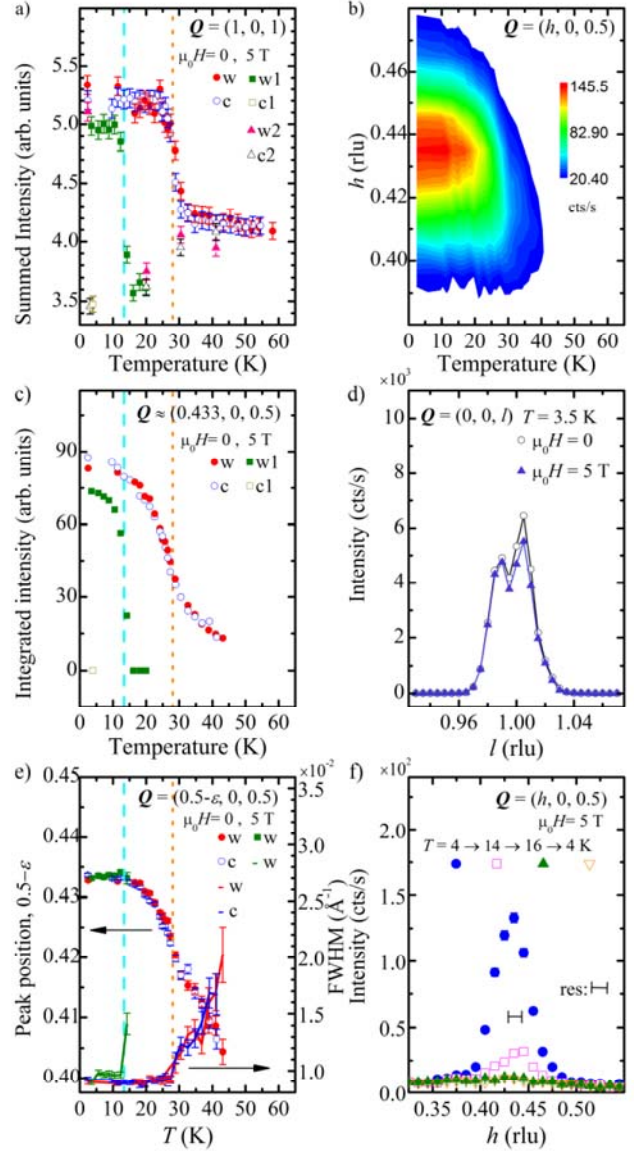
FIG. 9 Order parameters for the x_{EDX} = 0.06 sample, and sample alignment in field plotted with statistical error. The lower and upper dashed lines in panels a) c) and e) denote T_M and T_{SRO2}, respectively a) Structural order parameter (summation) b) Contour map of magnetic scattering measured on warming c) Magnetic order parameter (integration) d) (0, 0, 1) scan before and after applying field e) Incommensurability (symbols) and FWHM (lines) of AFM order; f) Magnetic peak measured in field while warming and cooling across T_M

We now turn to the structural and magnetic transitions in the x_{EDX} = 0.06 compound. We first discuss our observation in an ambient condition, that is μ_0H = 0T. We summed all counts in the Q range measured through the structural (1, 0,

1) peak and found that the intensity increases sharply at $T = 28$ K, which remains constant above this temperature. As discussed earlier, we believe that this temperature is associated with an in-plane structural distortion and we define $T = 28$ K to be the structural transition temperature T_S. As there is no evidence for thermal hysteresis our results are consistent with a second order transition through $T_S = 28$ K.

Figure 9b shows a contour plot of magnetic scattering in $x_{EDX} = 0.06$ measured at $Q_{AFM} = (h, 0, 0.5)$ without an applied field ($\mu_0 H = 0$ T). We fit the $(h, 0, 0.5)$ magnetic peak with the Lorentzian peak shape function and present the integrated intensities (Fig. 9c), the full-width-at-half-maximum (FWHM, Fig. 9e) and the peak position (Fig. 9e) as a function of temperature. We note that the instrumental resolution is convoluted in the analysis of the correlation length which is shown in Fig. 10. Weak signals at Q_{AFM} appear below $T = 43.2$ K and increase gradually until the slope maximizes at $T = 28$ K. The analysis of the FWHM and the correlation length of the magnetic peak demonstrates that the magnetic ordering is short ranged when it appears at the short range magnetic transition temperature $T_{SRO1} = 43.2$ K and the magnetic correlation length is temperature dependent down to $T = 28$ K (Fig. 9e and Fig. 10). With further cooling, the FWHM reaches its minimum value (not resolution-limited) with a correlation length of 250 Å and remains constant below T_S as shown in Fig. 9e and Fig. 10. We define the second short range order transition to be the temperature where the FWHM becomes constant and the magnetic intensity increases most rapidly: $T_{SRO2} = 28$ K. Although a short-range magnetic order was reported to coexist and compete with another long-range magnetic order in $Fe_{1.12}Te$ compound[2], we did not observe additional magnetic peaks in the measured Q range ($0.315 \le h \le 0.54$) but the short-range order alone. The observed short-range order may be caused by short-range bond-length modulations which were claimed in $Fe_{1.09}Te$ compounds[6].

However, details of the nature of the short range order in this compound call for further study.

In addition to the observation of the short-range magnetic order, we also observe that the magnetic peak is incommensurate at all temperatures measured and the peak position changes smoothly from $h \approx 0.40$ toward $h = 0.433$ (the value at $T = 2.4$ K) as shown in Fig. 9e, which corresponds to a real space periodicity of approximately seven magnetic unit cells in every sixteen structural cells along the a axis. The position is constant below $T \approx 13$ K (Fig. 9e). It is interesting to note that $T_{cusp} = 42$ K in the susceptibility measurements coincides with T_{SRO1} but no additional feature was observed in the susceptibility near $T_{SRO2} = T_S$.

Altogether, the short-range magnetic order occurs at $T_{SRO1} = 43.2$ K above the in-plane structural transition at $T_S = 28$ K which coincides with T_{SRO2}. Since we observe continuous
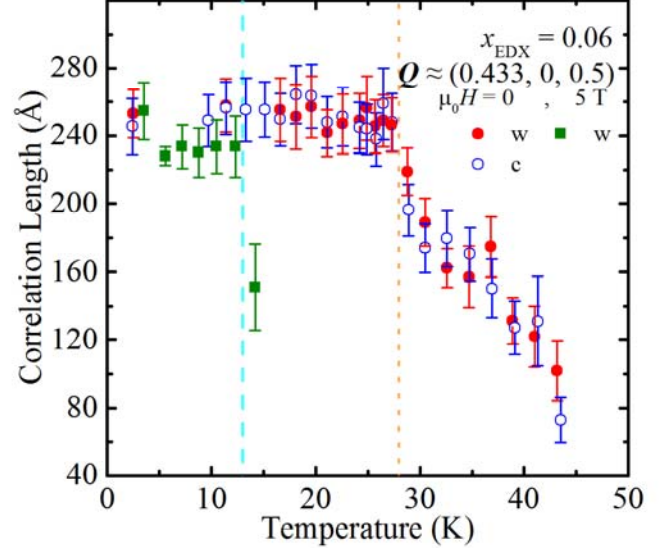
FIG. 10 The spin correlation length along the $[h, 0, 0]$ direction for $x_{EDX}=0.06$ compound, corrected for the instrumental resolution of SPINS with statistical error. The field conditions are indicated in the figure; the lower and upper dashed lines indicate T_M and T_{SRO2}, respectively

evolution of order parameters, continuous changes in FWHM, and no thermal hysteresis, we conclude that each of these transitions is second order in nature. Interestingly, we did not observe a structural transition at T_{SRO1}. However, based on the symmetry requirements for the AFM order at Q_{AFM}, a symmetry lowering transition should accompany T_{SRO1} but it may be too small to be detected with the given instrumental resolution.

Under an applied filed ($\mu_0 H = 5$ T) parallel to the $[0, 1, 0]$ direction in our scattering geometry, we observed surprising results in both the structural and magnetic transitions. In order to ensure the sample alignment under applied magnetic fields, we first measured the structural Bragg peaks without a field ($\mu_0 H = 0$ T) and then again after applying a field ($\mu_0 H = 5$ T). We observed a reduction (~10%) in the intensity of all peaks but the positions did not change which indicates a good sample alignment under an applied field (Fig. 9d). While the cause of the decrease in the peak intensities with $\mu_0 H = 5$ T is unknown it might be due to a subtle rotation of the sample. Knowing that our sample alignment is good under $\mu_0 H = 5$ T, we measured the temperature dependent structural (1, 0, 1) peak under $\mu_0 H = 5$ T. As shown with w1 and c1 in Fig. 9a, the Bragg peak intensity did not change much until it suddenly dropped between 12 and 14 K during warming. The magnetic $(h, 0, 0.5)$ peak was monitored simultaneously and showed the same behavior (disappeared completely at 16 K) as shown with w1 and c1 in Fig. 9 c and 9f. To complete the temperature dependence, we then measured (1, 0, 1) and $(h, 0, 0.5)$ peaks while cooling in the

62

TABLE II. Fitted exponent of log(R) vs. log(T) data in different temperature ranges

Temperature Range (K)	$m(x_{EDX}=0.52)$	$m(x_{EDX}=0.55)$
20-150K	0.825(1)	1.026(1)
150-300K	1.011(1)	1.235(1)

field and found that the signals do not increase across $T \approx 14$ K. We considered that this observation might be due to a misalignment of our sample during a temperature cycle under fields so we warmed the temperature well above T_{SRO2} to check the sample alignment then recovered the intensity at (1, 0, 1) (Fig. 9a). We cooled our sample to $T = 4$ K again without an applied magnetic field and recovered the intensity of (1, 0, 1) again which confirms the alignment during temperature cycles. We also recovered the intensity at $\boldsymbol{Q}_{AFM}$ and the original temperature dependence which confirms the absence of a remanent field. At $T = 4$ K, we applied a magnetic field ($\mu_0 H = 5$T) and measured the temperature dependence of the structural (1, 0, 1) peak at selected temperatures as denoted as w2 and c2 in Fig. 9a. We thus reproduced the results while warming in field, and confirmed that the field-cooled behavior is consistent whether the sample is cooled from $T = 80$ K or $T = 20$ K. Therefore this transition is metastable in field and both the structural and magnetic transitions occur abruptly at $T_M = 13$ K. In the magnetic state below T_M, the incommensurability does not change and the peak appears at a value of $h = 0.433$ which may indicate a first-order lock-in transition.

The absence of the magnetic intensity in the field cooled measurements in this compound may be seen as a strong random field effect of the Cu impurities. In site diluted antiferromagnets, field-cooling through the magnetic transition induces a "domain state" in which magnetic moments around the impurities are, on average, paramagnetic with the applied field; these paramagnetic moments may limit the long range ordering[42–44]. It may be possible for a strong random field effect to completely inhibit the magnetic ordering as observed in our case. The increase in the divergence of dχ/dT at the transition for x_{EDX} ≤ 0.10 is also suggestive of a random field scenario[38].

Furthermore, upon warming in the field between T_M and 30 K as well as in cooling in the field at all temperatures below 30 K, the intensity of the (1, 0, 1) peak is much lower than the field-free values (Fig. 9a). This low intensity implies that another structure type may exist under these conditions, possibly different from the tetragonal structure above the transition and from the structure below the transition in zero field (which we have not identified). The simultaneous first-order magnetic and structural transitions at $T_M = 13$ K indicate a strong coupling between magnetism and structure. Hence if the structure without the AFM at 13 K < T < 30 K remains stable under field cooling below T_M, the AFM
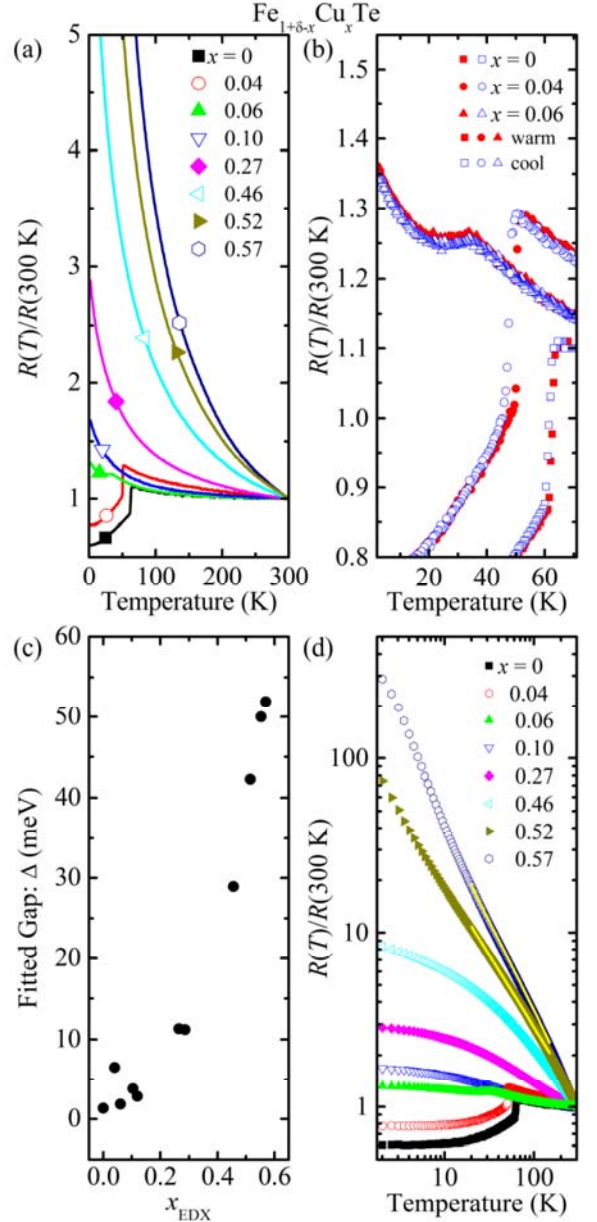
FIG. 11 Normalized resistance of Fe$_{1+\delta-x}$Cu$_x$Te compounds. a) Data with linear axes and plotted in a limited range of normalized resistance, for comparison of samples. b) Measurements upon cooling and subsequent warming for $x_{EDX} \leq 0.06$. c) Fitted energy gap versus x_{EDX} for the data with 200 K ≤ T ≤ 300 K. d) Data with logarithmic axes and plotted in the full range of normalized resistance. Yellow lines are power law fits as described in the text

transition will not occur. Further study is necessary to determine the details of each of these transitions at T_M as well as another possible transition between T_M and 30 K ($\approx T_{SRO2}$).

63

F. Resistance

Figure 11 shows the normalized electrical resistance data $R(T)/R(300\text{ K})$ of $Fe_{1+\delta-x}Cu_xTe$ measured as a function of temperature between $T = 2$ K and 300 K. As the copper concentration increases, the resistance anomaly moves to lower temperatures, and is absent in samples which only exhibit spin-glass transitions at low temperature i.e. $x_{EDX} \geq 0.1$ (Figs. 11a and 11b). The normalized resistance increases with both increasing copper concentration and decreasing temperatures at all compositions and temperatures, aside from the sample with $x_{EDX} = 0.04$ that has higher normalized resistance than the samples with $x_{EDX} = 0.06$ or $x_{EDX} = 0.1$ between $T = 53$ K and 300 K. Such behavior was reproduced for samples from two different growth batches for each composition. The higher normalized resistance in $x_{EDX} = 0.04$ suggests that the samples in the previous study[11] may have different site occupancy parameters (δ, η, and/or vacancies), and/or different nonequilibrium characteristics (phase segregation parameters, or defects) due to the different growth methods used.

Figure 11b shows the anomalies in resistance measured upon cooling and subsequent warming for $x_{EDX} \leq 0.06$. For $x_{EDX} = 0$ and 0.04, we found a thermal hysteresis upon cooling and warming, which indicates first-order transitions. This is consistent with the observation in neutron measurements for $x_{EDX} = 0.04$; therefore, the observed transition in the resistance indicates the Neel transition. We define the transitions $T_N^{resistance}$ at the local maxima in the resistance values, $T_N^{resistance} = 65.5$ K (warming) and 64.5 K (cooling) for $x_{EDX} = 0$, and $T_N^{resistance} = 52$ K (warming) and 50.5 K (cooling) for $x_{EDX} = 0.04$. Unlike the sharp and hysteretic anomalies in $x_{EDX} = 0$ and 0.04, the sample with $x_{EDX} = 0.06$ shows a broad maximum centered at $T_{max}^{resistance} = 34 \sim 36$ K and a broad minimum centered at $T_{min}^{resistance} = 22 \sim 25$ K, where the range of values estimated for the extrema depends on whether a flat or sloping background is taken. Below $T_{min}^{resistance}$ the resistance increases with decreasing temperature which is different to the behavior at lower copper substitution, but similar to the effects of excess iron in $Fe_{1+\delta}Te$[5,45] where it has been attributed to the closing of a spin gap in the helical AFM phase. Because our neutron measurement does not rule out the helical magnetic structure in our sample, the increase of the resistance at $T < T_{min}^{resistance}$ may be due to the closing of the spin gap. $T \approx 28$ K is between the temperatures of the local maximum and minimum in resistance so we associate this transition with $T_S = T_{SRO2} = 28$ K determined in neutron measurements, noting that no resistance anomaly was observed at $T_{SRO1} = 43.2$ K which is far above the maxima and minima in the resistance of $x_{EDX} = 0.06$. Furthermore, we have observed the appearance of transitions at temperatures close to T_M (which are not shown) under the applied field[46].

In order to gain insight into the relevant transport processes of $Fe_{1+\delta-x}Cu_xTe$, we analyze the resistance data using models that have been proposed to govern the transport in $Fe_{1+\delta}Te$[47] or in Cu substituted compounds with $x \approx 0.5$[16–18]. As the samples become less conductive upon copper substitution, we tried fitting to an activated model, commonly used to model an intrinsic semiconductor or insulator[48] and written as

$$R(T) \propto \frac{1}{qn\mu} \propto T^{-m}e^{-\frac{\Delta}{2kT}} + R_0 \quad (2)$$

where the exponent m includes temperature dependences of the carrier concentration n and mobility μ, Δ is the band gap, and R_0 is a constant. We set $m = 0$ and performed fits for Δ by fitting $\ln(R)$ vs $1/T$ to a line between $T = 200$ K and 300 K, and extracted the Δ values shown in Fig 11c. If the model is valid, these fits suggest that Δ increases from 1 to $\sim$50meV in the range $0 \leq x_{EDX} \leq 0.57$, as shown in Fig 11c; the values at high substitution are intermediate to $\Delta = 23$-70meV as reported in previous studies for $x \approx 0.5$[17,18].

We also tried power-law scaling of the resistance that was observed in previous studies in samples with $x \approx 0.5$ with exponents of $m = 1.15$[16] or $m = 1$[18], which the authors[16] attributed to the realization of the condition $\Delta \approx 0$ in Equation (2). The power-law scaling behavior was first observed in semimetals such as α-Sn or HgTe[49,50]. We present R vs. T on a logarithmic scale in Fig. 11d. The resistance in $\log(R)$ vs. $\log(T)$ is nearly linear for samples with $x_{EDX} = 0.52$ and 0.57. The fits of the raw data between 20 K and 150 K for $x_{EDX} = 0.52$ and $x_{EDX} = 0.57$ using Equation (2) with a mesh of $\Delta = 0:1:500$meV and $m = -3:0.01:3$ yield the best fits with $\Delta = 0$ (solid lines in Fig. 11d). In Table II, we present variation of the fitted exponents when different temperature ranges of data were fitted. Similar to a previous study on FCT with $x \approx 0.5$, the deviation from the power law fit was greatest at low temperatures[18]. Although the resistance of the $x_{EDX} = 0.04$ sample can be fitted to a power law above its transition with an exponent close to zero, the $x_{EDX} = 0$ sample does not fit well to a power law. Thus, we believe the power law behavior is less relevant for these low-substituted samples.

Another form which has been suggested to fit the resistance above the Neel transition temperature in iron-telluride is[47]:

$$R \propto \log(1/T) + R_0 \quad (3)$$

where R_0 is constant. This form is suggested to arise from a weak localization effect involving electronic scattering at

interstitial sites. Our fits to the data for the samples with x_{EDX} = 0 and 0.04 above their transition temperatures were good but failed to fit the data far above T_N for x_{EDX} = 0. This form could not fit any significant temperature range of the data for other compositions.

Finally, we attempted to fit the data to variable-range hopping models which describe temperature-activated conduction when electronic states are localized due to Coulomb repulsion or disorder[51]. The variable-range hopping formula is:

$$\ln(R(T)) \propto (1/T)^{1/(d+1)} + R_0 \quad (4)$$

where the exponent d is the dimensionality of the system. While this model with d = 3 has been suggested to provide a good fit to the resistance curves in copper-substituted $FeSe_{0.96}$[26], $FeSe_{1-y}Te_y$[27], and FCT with $x \approx 0.5$[17], we found that it does not provide a good fit to any of our data over any appreciable temperature range and the fit is especially poor at low temperatures where the closest agreement with the model should occur[51]. The fits with varying d in temperature ranges between 2 and 30 K, between 2 and 120 K, and between 70 and 300 K are unstable as indicated by large uncertainty or nonphysical values of d. Another recent work also reported the lack of fit of the variable range hopping model to the resistance of samples with $x \approx 0.5$[18].

Taken together, we find that the variable range hopping model cannot fit any of the data. The data for samples with x_{EDX} = 0 and 0.04 could be fit by the $R \sim -\ln(T)$ model, which is ascribed to localization due to electronic scattering at the interstitial sites[47]. For samples with x_{EDX} = 0.52 and x_{EDX} = 0.57, the resistivity data can be well-fitted by power laws across a large region of temperature with the exponent $m \approx 1$ that may be interpreted as support for a model of localized and diffusive charge transport as claimed in previous reports[16,18]. Whereas the activated model can describe the high temperature data for each sample, fitting the low temperature data can only be done with the weak localization model in the low-substitution limit or with the zero band gap model in the high substitution limit. Although it is difficult to determine conclusively, our observations suggest that local interactions are important factors in the transport mechanisms.

4. SUMMARY AND CONCLUSION

We have studied the stoichiometry, crystal structure, magnetism, and electrical resistance of $Fe_{1+\delta-x}Cu_xTe$ single crystals grown by the modified Bridgman method. Similar to other metal substituted iron-telluride systems, copper substitution causes suppression of the magnetic and
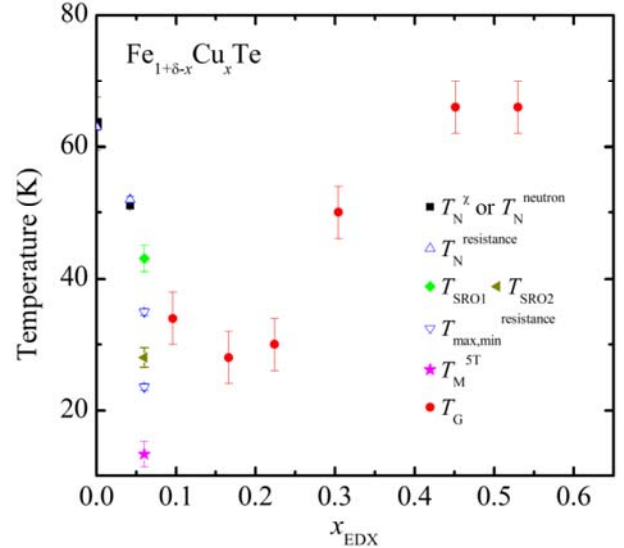
FIG. 12 Magnetic phase diagram of $Fe_{1+\delta-x}Cu_xTe$ compounds. See text for details of the notation

structural transitions. From our studies of susceptibility, resistance, and neutron measurements, we constructed a phase diagram of $Fe_{1+\delta-x}Cu_xTe$ which we show in Fig. 12. The long-range AFM transition is rapidly suppressed with only slight copper substitution. When x_{EDX} = 0.06, the long-range AFM order is replaced by short-range ordering which exhibits two transitions (T_{SRO1} and T_{SRO2}). Under $\mu_0 H$ = 5T, we observed a metastable magnetic transition at T_M. At $x_{EDX} \geq 0.1$, a spin glass phase appears at a minimum of T_G = 28 K at x_{EDX} = 0.16 and T_G increases with further copper substitution.

We find that the structural and antiferromagnetic transitions occur at the same temperature and show first-order nature in x_{EDX} = 0 and 0.04. The AFM ordering is commensurate in these compounds, and gives way to incommensurate short-range order in x_{EDX} = 0.06. The short-range order appears continuously without a detectable structural transition and at lower temperature another short-range ordering transition, defined by the saturation of the correlation length (250 Å), occurs simultaneously with a structural transition. A first-order metastable magnetic transition appears at $T_M \approx 13$ K under an applied magnetic field which indicates strong coupling between structure and magnetism. The behavior of the magnetic component of this transition may indicate random field effects. Furthermore, detailed study of the resistance data indicates the localized nature of the transport at all compositions within the phase diagram. These results suggest that strong in-plane field

effects present challenges to understanding the magnetism in the iron chalcogenides.

ACKNOWLEDGEMENTS

[1] Y. Xia, D. Qian, L. Wray, D. Hsieh, G.F. Chen, J.L. Luo, N.L. Wang, and M.Z. Hasan, Phys. Rev. Lett. **103**, 037002 (2009).

[2] E.E. Rodriguez, C. Stock, P. Zajdel, K.L. Krycka, C.F. Majkrzak, P. Zavalij, and M.A. Green, Phys. Rev. B **84**, 064403 (2011).

[3] Z. Xu, Ph.D. Thesis, City University of New York, 2011.

[4] I.A. Zaliznyak, Z.J. Xu, J.S. Wen, J.M. Tranquada, G.D. Gu, V. Solovyov, V.N. Glazkov, A.I. Zheludev, V.O. Garlea, and M.B. Stone, Phys. Rev. B **85**, 085105 (2012).

[5] E.E. Rodriguez, D.A. Sokolov, C. Stock, M.A. Green, O. Sobolev, J.A. Rodriguez-Rivera, H. Cao, and A. Daoud-Aladine, Phys. Rev. B **88**, 165110 (2013).

[6] D. Fobes, I.A. Zaliznyak, Z. Xu, R. Zhong, G. Gu, J.M. Tranquada, L. Harriger, D. Singh, V.O. Garlea, M. Lumsden, and B. Winn, Phys. Rev. Lett. **112**, 187202 (2014).

[7] W. Bao, Y. Qiu, Q. Huang, M.A. Green, P. Zajdel, M.R. Fitzsimmons, M. Zhernenkov, S. Chang, M. Fang, B. Qian, E.K. Vehstedt, J. Yang, H.M. Pham, L. Spinu, and Z.Q. Mao, Phys. Rev. Lett. **102**, 247001 (2009).

[8] R. Viennois, Acta Phys. Pol. A **121**, 928 (2012).

[9] R. Hu, E.S. Bozin, J.B. Warren, and C. Petrovic, Phys. Rev. B **80**, (2009).

[10] J. Janaki, T. Geetha Kumary, N. Thirumurugan, A. Mani, A. Das, G. V. Narasimha Rao, and A. Bharathi, J. Supercond. Nov. Magn. **25**, 209 (2011).

[11] H. Wang, C. Dong, Z. Li, J. Yang, Q. Mao, and M. Fang, Phys. Lett. A **376**, 3645 (2012).

[12] J. Wen, Z. Xu, G. Xu, M. Lumsden, P.N. Valdivia, E. Bourret-Courchesne, G. Gu, D.-H. Lee, J.M. Tranquada, and R.J. Birgeneau, Phys. Rev. B **86**, 024401 (2012).

[13] A.-M. Lamarche, J.C. Woolley, G. Lamarche, I.P. Swainson, and T.M. Holden, J. Magn. Magn. Mater. **186**, 121 (1998).

[14] A. Rivas, F. Gonzalez-Jimenez, L. D'Onofrio, E. Jaimes, M. Quintero, and J. Gonzalez, Hyperfine Interact. **134**, 115 (2001).

[15] A. Rivas, F. Gonzalez-Jimenez, L. D'Onofrio, E. Jaimes, M. Quintero, and J. Gonzalez, Hyperfine Interact. **113**, 493 (1998).

[16] A.A. Vaipolin, S.A. Kijaev, L.V. Kradinova, A.M. Polubotko, V. V. Popov, V.D. Prochukhan, Y. V. Rud, and V.E. Skoriukin, J. Phys. Condens. Matter **4**, 8035 (1992).

[17] F.N. Abdullaev, T.G. Kerimova, G.D. Sultanov, and N.A. Abdullaev, Phys. Solid State **48**, 1848 (2006).

[18] D.A. Zocco, D.Y. Tutun, J.J. Hamlin, J.R. Jeffries, S.T. Weir, Y.K. Vohra, and M.B. Maple, Supercond. Sci. Technol. **25**, 084018 (2012).

[19] J. Llanos and C. Mujica, J. Alloys Compd. **217**, 250 (1995).

[20] A.B. Karki, V.O. Garlea, R. Custelcean, S. Stadler, E.W. Plummer, and R. Jin, Proc. Natl. Acad. Sci. **110**, 9283 (2013).

[21] C. Fang, B. Andrei Bernevig, and J. Hu, Europhys. Lett. **86**, 67005 (2009).

[22] F. Ma, W. Ji, J. Hu, Z.-Y. Lu, and T. Xiang, Phys. Rev. Lett. **102**, 177003 (2009).

[23] C. Stock, E.E. Rodriguez, M.A. Green, P. Zavalij, and J.A. Rodriguez-rivera, Phys. Rev. B **84**, 045124 (2011).

[24] S. Chadov, D. Schärf, G.H. Fecher, C. Felser, L. Zhang, and D.J. Singh, Phys. Rev. B **81**, 104523 (2010).

[25] D.M. Basko, I.L. Aleiner, and B.L. Altshuler, in *Probl. Condens. Matter Phys.* (Oxford University Press, Oxford ; New York, 2008).

[26] T.-W. Huang, T.-K. Chen, K.-W. Yeh, C.-T. Ke, C.L. Chen, Y.-L. Huang, F.-C. Hsu, M.-K. Wu, P.M. Wu, M. Avdeev, and A.J. Studer, Phys. Rev. B **82**, 104502 (2010).

[27] J. Wen, S. Li, Z. Xu, C. Zhang, M. Matsuda, O. Sobolev, J.T. Park, A.D. Christianson, E. Bourret-Courchesne, Q. Li, G. Gu, D.-H. Lee, J.M. Tranquada, G. Xu, and R.J. Birgeneau, Phys. Rev. B **88**, 144509 (2013).

[28] N. Mott, J. Solid State Chem. **88**, 5 (1990).

[29] T. Kasuya, A. Yanase, and T. Takeda, Solid State Commun. **8**, 1551 (1970).

[30] J. Wen, G. Xu, G. Gu, J.M. Tranquada, and R.J. Birgeneau, Reports Prog. Phys. **74**, 124503 (2011).

[31] B.C. Sales, A.S. Sefat, M.A. McGuire, R.Y. Jin, D. Mandrus, and Y. Mozharivskyj, Phys. Rev. B **79**, 094521 (2009).

[32] B.H. Toby, J. Appl. Crystallogr. **34**, 210 (2001).

[33] J.H. Chu, *(Private Communication)* (2013).

[34] A. Martinelli, A. Palenzona, M. Tropeano, C. Ferdeghini, M. Putti, M.R. Cimberle, T.D. Nguyen, M. Affronte, and C. Ritter, Phys. Rev. B **81**, 094115 (2010).

[35] R.V. Baranova and Z.G. Pinsker, Sov. Phys. Crystallogr. **14**, 214 (1969).

[36] R.T. Downs and M. Hall-Wallace, Am. Mineral. **88**, 247 (2003).

[37] S. Nagata, P.H. Keesom, and H.R. Harrison, Phys. Rev. B **19**, 1633 (1979).

[38] S. Fishman and A. Aharony, J. Phys. C Solid State Phys **12**, L729 (1979).

[39] Y. Mizuguchi, K. Hamada, K. Goto, H. Takatsu, H. Kadowaki, and O. Miura, Solid State Commun. **152**, 1047 (2012).

[40] A. Kreyssig, M.G. Kim, S. Nandi, D.K. Pratt, W. Tian, J.L. Zarestky, N. Ni, A. Thaler, S.L. Bud'ko, P.C. Canfield, R.J. McQueeney, and A.I. Goldman, Phys. Rev. B **81**, 134512 (2010).

[41] X. Lu, J.T. Park, R. Zhang, H. Luo, A.H. Nevidomskyy, Q. Si, and P. Dai, Science (80-.). **345**, 657 (2014).

[42] D.S. Fisher, G.M. Grinstein, and A. Khurana, Phys. Today **41**, 56 (1988).

[43] D.P. Belanger, S.M. Rezende, A.R. King, and V. Jaccarino, J. Appl. Phys. **57**, 3294 (1985).

[44] R.J. Birgeneau, J. Magn. Magn. Mater. **177-181**, 1 (1998).

[45] M.H. Fang, H.M. Pham, B. Qian, T.J. Liu, E.K. Vehstedt, Y. Liu, L. Spinu, and Z.Q. Mao, Phys. Rev. B **78**, 224503 (2008).

[46] T. Helm and P.N. Valdivia, Unpublished (2015).

[47] S. Rößler, D. Cherian, H.S. Nair, H.L. Bhat, S. Elizebeth, and S. Wirth, J. Phys. Conf. Ser. **400**, 022099 (2012).

[48] S.M. Sze and K.K. Ng, *Physics of Semiconductor Devices, 3rd Edition by S . M. Sze and Kwok K. Ng Copyright 0 John Wiley & Sons, Inc.* (John Wiley and Sons, Inc., College Park, MD, 2007).

[49] S. Groves and W. Paul, Phys. Rev. Lett. **11**, 194 (1963).

[50] R. Piotrzkowski, S. Porowski, Z. Dziuba, J. Ginter, W. Giriat, and W. Sosnowski, Phys. Stat. Sol. **8**, K135 (1965).

[51] N.F. Mott, Philos. Mag. **32**, 159 (1975).

6.3   Outlook

Going in to this study, we did not expect to find that the applied magnetic field effects the magnetic order. Further study of the behavior of resistance of several compounds as a function of magnetic field may prove useful to understanding the details of the interactions of magnetic moments with an applied field. Understanding how and when the magnetic order can be tuned by the applied field may be interesting in light of the supposed relations of magnetic order to the superconductivity which occurs in closely related alloys. We are in the midst of analyzing such data at the time of compiling this dissertation.